UNIVERSITY OF OKLAHOMA

GRADUATE COLLEGE

EVALUATION OF SHALE COMPRESSIBILITY FROM NMR AND MICP MEASUREMENTS

A THESIS

SUBMITTED TO THE GRADUATE FACULTY

in partial fulfillment of the requirements for the

Degree of

MASTER OF SCIENCE

By

BACHIR MAHOMAD
Norman, Oklahoma
2014

EVALUATION OF SHALE COMPRESSIBILITY FROM NMR AND MICP MEASUREMENTS

A THESIS APPROVED FOR THE
MEWBOURNE SCHOOL OF PETROLEUM AND GEOLOGICAL ENGINEERING

BY

[redacted]
Dr. Carl H. Sondergeld, Chair

[redacted]
Dr. Chandra S. Rai

[redacted]
Dr. Deepak Devegowda

ACKNOWLEDGEMENT

I would like to dedicate this work to my mother and father who have given every ounce of their beings to the education of their children. Thank you for always being there for me. Only God can repay you for all your good deeds. I would like to express my sincere gratitude to Dr Carl Sondergeld who has been my mentor and advisor during my studies at the OU. I would like to thank him for his commitment and dedication to teaching students both in and outside the classroom. Furthermore I would like to thank Dr Chandra Rai for his feedback and financial support during my graduate school and Dr Deepak Devegowda for continuous support and advice. I would like to thank Gary Stowe, Joe Flenniken and Bruce Spears for their assistance and teaching on how to use the different equipment in the lab.

Special thanks to my cousin Ahmat Mahmat who has always being here for me when I needed him the most. Special thanks to Ali Tinni for the countless discussions and his incredible insight in petrophysics and experimental design. Special thanks to Shalli Young who gladly went out of her way to my life in Norman much easier.

Finally, I would like to thank students, faculties and staffs at Mewbourne School of Petroleum and Geological Engineering for their help and friendship.

TABLE OF CONTENTS

LIST OF FIGURES

LIST OF TABLES

ABSTRACT

Compressibility is a fundamental reservoir parameter that is often overlooked in the assessment of unconventional reservoir performance. Compressibility affects the reserve, recovery, and the mechanical properties of reservoir rock. This study focuses on the evaluation of Mercury Injection Capillary Pressure (MICP) data to compute compressibility. Additionally, the MICP approach is compared to measured pore volume compressibility from Nuclear Magnetic Resonance (NMR) data and pore volume compressibility using helium. Compressing shale forces fluids out of the pore space; thus, aiding the recovery of hydrocarbon. Compressibility was studied over a range of confining pressure from 0-5000 psi with NMR and helium. NMR, MICP, and helium compressibilities were calibrated on sandstone and limestone samples. The error in the estimation of pore compressibility among the three methods was less than 30% at higher pressures. A total of 175 samples from Barnett, Woodford, Haynesville, Eagle Ford and Wolfcamp shales were analyzed. Eleven total samples from Eagle Ford (6), Wolfcamp (4), and Haynesville (1) are selected for NMR pore volume compressibility measurements. The range of NMR measured pore compressibility varies from $2*10^{-6}$ to $1.8*10^{-4}$ psi^{-1}.

This study shows that shale has a significant compressibility, especially at lower confining pressure. Furthermore, the shale compressibility also exhibits a strong pressure dependence which is apparently controlled by microcracks at low pressure. The compressibility measured using NMR agrees with the derived MICP compressibility. No relationship could be established between pore volume compressibility and other measure petrophysical properties.

The experimental results of this study are used to evaluate the effect of compressibility change on production from unconventional resources. Three cases of oil, gas condensate, and gas reservoirs are considered. Results from the simulation indicated that 2 to 25 % underestimation occurs in the prediction of production from oil and gas condensate windows in shale resources when shale compressibility is neglected.

1: INTRODUCTION

"Unconventional resources" is a generic term used to describe a wide range of hydrocarbon bearing formations which cannot produce economically without proper stimulation (Passey et al., 2010). This definition includes reservoirs such as tight gas sand, gas hydrates; oil and gas shale etc.

Shale is the most common sedimentary rock, it accounts for almost 60 % of all sedimentary rocks in the surface of the Earth (Boggs, 2009). Shales were traditionally studied to determine source rock potential (Rieke et al., 1980; Schmoker (1979, 1981); Passey et al., 1990) or the sealing capacity of the cap rock (Berg, 1995; Nelson and Simmons, 1992; Schlomer and Krooss, 1997). Now, they are being reevaluated as reservoirs.

Recent improvements in horizontal drilling and hydraulic fracturing technologies have transformed shale economics, making shale a valuable unconventional resource play. The US has an estimated 665 Tcf of gas recoverable distributed over 20 shale plays throughout the country as shown in Fig 1.1 (EIA, 2013). The gas production from shales enables the US to gain access to a reliable and secure supply of hydrocarbon which can ensure energy independence for decades to come. According to the US Energy Information Administration (EIA) Annual Energy Outlook Report (2012), 95% of gas consumed in the US was produced domestically. Gas shales accounted for up to 40% of the total US natural gas production. The production of gas shale is expected to rise from 23 Tcf in 2011 to 33.1Tcf in 2040 which corresponds to a 44% increase (EIA, 2012).

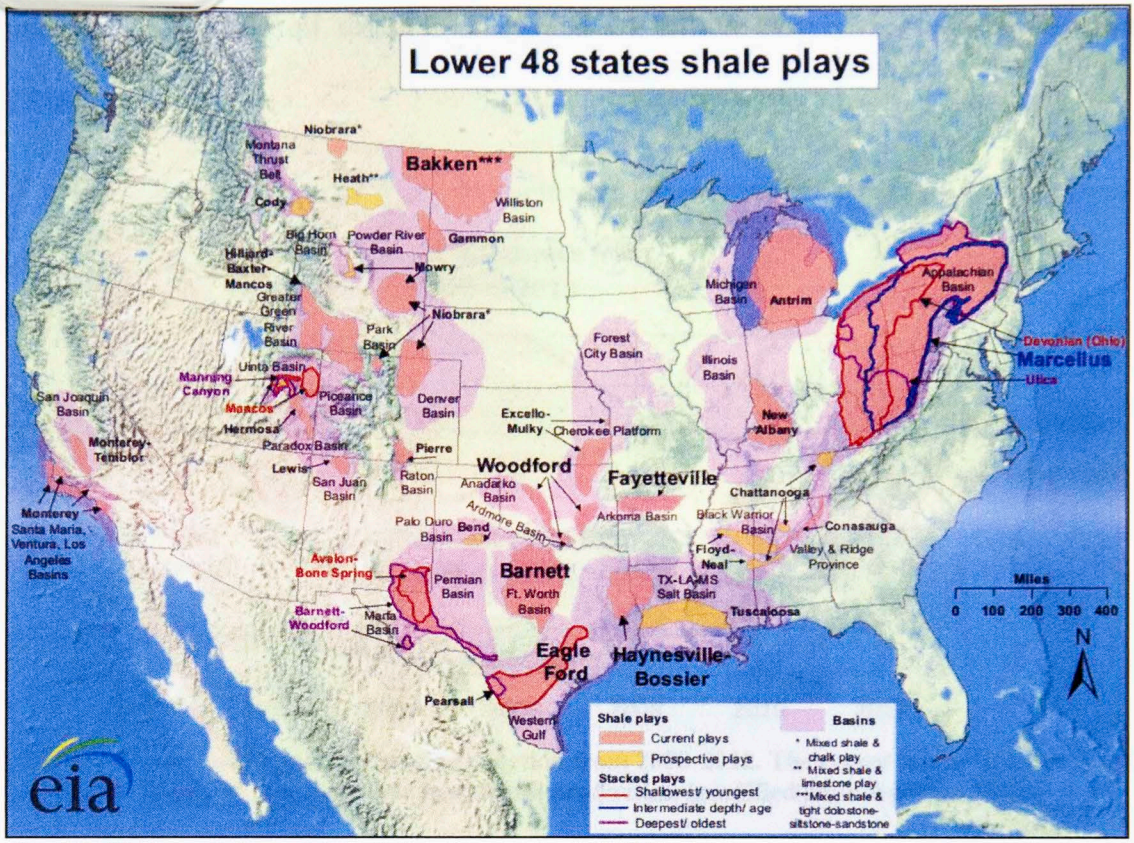

Fig. 1.1: Shale gas plays and their location in the US (EIA, 2011).

The technical advancement made in gas shale production and the high natural gas price from 2005-2010 have led to the production of large volumes of natural gas in the US. However, the rapid growth in natural gas production and the lack of global market integration have caused a saturation of the US market and a drop in natural gas prices in recent years. The disconnected energy value of gas versus oil pushed oil and gas companies to favor liquid hydrocarbon production. This shift made liquid and condensate hydrocarbon producing formations such as the Wolfcamp, Eagle Ford, and Bakken shales more appealing. The US crude production grew exponentially over the past five years (**Fig 1.2**). The US crude oil production increased by almost 847,000 bbl/d from 2011to 2012. This increase was largely driven by liquid production from shale reservoirs which accounts for almost 29% of the total US oil production. The

estimated US shale oil resource is around 24 billion barrels recoverable (Aguilera, 2013).

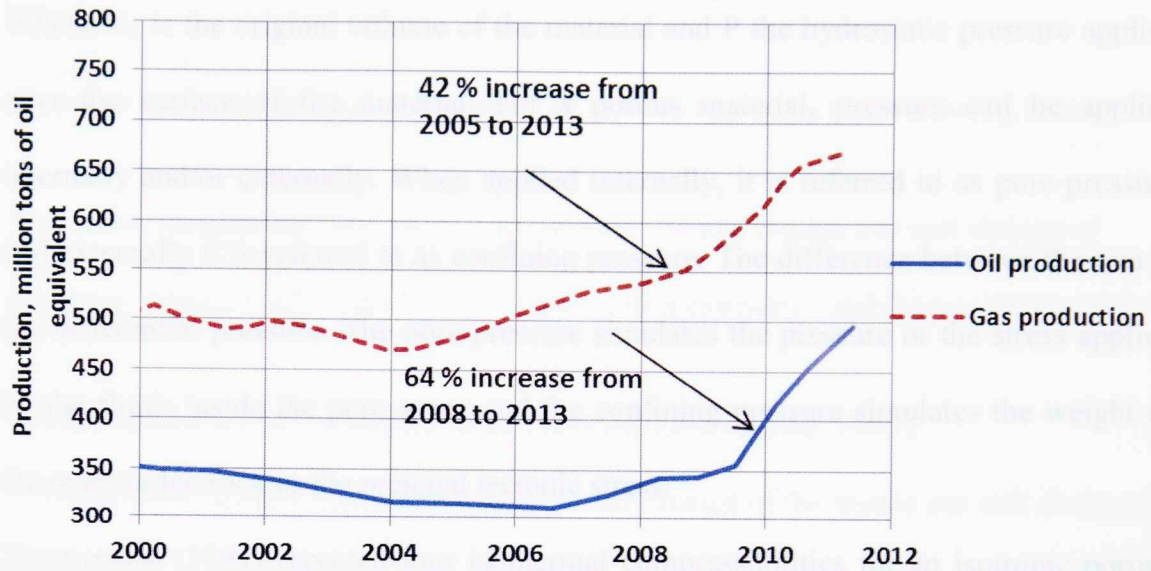

Fig 1.2: US natural gas and crude oil production from 2000-2012. The recent increase in crude oil production is driven by an increase in shale oil production (modified from Aguilar, 2013).

Although significant advances have been made in our understanding of storage capacity, flow capacity, and mechanical properties of shale reservoirs, several challenges still remain. Shale reservoirs are characterized by severe heterogeneity over both small and large scales which reflect the geologic and biotic conditions that prevailed during deposition. These added complexities affect both storage and transport and make shale exploration and development challenging for engineers.

1.1: Compressibility

Compressibility of reservoir rocks is a key drive mechanism and is often ignored in shale reservoirs. Limited data exist that describe the extent of the bulk or pore compressibility in shales. Compressibility, C, is defined as the change in volume as a result of pressure applied on a body (Zimmerman, 1991). It is denoted by the following general formula:

$$C = \frac{-1}{V_i}\left(\frac{dV}{dP}\right) \quad 1.1$$

Where V_i, is the original volume of the material and P the hydrostatic pressure applied over the surface of the material. For a porous material, pressure can be applied internally and/or externally. When applied internally, it is referred to as pore pressure and externally it is referred to as confining pressure. The difference between the two is the differential pressure. The pore pressure simulates the pressure or the stress applied by the fluids inside the pore space and the confining pressure simulates the weight of the overburden rock or the regional tectonic stress.

Zimmerman (1991) reported four isothermal compressibilities for an isotropic porous material. These compressibilities are functions of the applied pressure (pore or confining) and the resultant changes in either bulk or pore volume as illustrated below:

$$C_b^c = \frac{-1}{V_b}\left[\frac{\partial V_b}{\partial P_c}\right]_{P_p} \quad 1.2$$

$$C_b^P = \frac{1}{V_b}\left[\frac{\partial V_b}{\partial P_P}\right]_{P_C} \quad 1.3$$

$$C_p^C = \frac{-1}{V_P}\left[\frac{\partial V_P}{\partial P_C}\right]_{P_P} \quad 1.4$$

$$C_p^P = \frac{1}{V_P}\left[\frac{\partial V_P}{\partial P_P}\right]_{P_C} \quad 1.5$$

Where C_b^c is the "effective bulk" compressibility and represents the bulk volume change per unit change of confining pressure, C_b^P is the "pseudo bulk compressibility" and represents the total bulk volume change per unit change of pore pressure. C_p^C is the "formation compaction" and represents the pore volume change per unit change of confining pressure. C_p^P is the "effective pore compressibility" and represents the pore volume change per unit change of pore pressure (Zimmerman, 1991).

A fifth compressibility, representing the volume change of the matrix per unit change of pressure can be defined. It is referred to as the matrix or the grain bulk compressibility and has the following equation:

$$C_r = \frac{-1}{V_g}\frac{\partial V_g}{\partial P} \qquad 1.6$$

$$C_r = \frac{1}{K_r} \qquad 1.7$$

Where K_r is the bulk modulus of the rock matrix.

The bulk compressibility controls the propagation of seismic waves underground and is useful in modeling subsidence. Pore compressibility is vital for reservoir engineers in estimating storage capacity of rock. The compressibility value is an input into the material balance for estimating OOIP (Original Oil in Place). It affects both the reserve estimate and the mechanical properties of the rock.

1.2: Outline

This study is divided into five chapters. The introduction and the scope of the project is given in chapter one. The second chapter explores the background theory and principles in shales characterization as well as a review of past research on the compressibility of rocks. The third chapter deals with the experimental set up and procedures followed during the compressibility measurements. The fourth chapter provides a detailed discussion of the observation and consequences in reservoir simulation. Chapter five summarizes the main conclusions and recommendations.

2: INTRODUCTION AND THEORETICAL BACKGROUND

2.1: Introduction to Shales

The recent focus in unconventional resources fuels the study of fine grained sedimentary rocks. Little agreement exists among geologists and sedimentologists on the terminology to use to define shales which make up approximately 60% of all sedimentary rocks (Boggs, 2009). Some authors recommend using the general class name mudstone to describe all fine grained argillaceous and siliclastic rocks that have particle sizes less than 62 microns, while, some argue that shale only referred to laminated or fissile fine-grained sedimentary rocks (Potter et al., 2005). Shales are typically composed of clays, micas, quartz, feldspar, and carbonates. The amount and the type of clay minerals control the degree of lithification and lamination in shales (Haldar and Tišljar, 2014).

2.2: Organic Matter Origin and Classification

Along with clay minerals, organic matter is also prevalent in most mudstones and shales. Organic matter comes from dead organisms and plants composed of carbohydrates, proteins, and lipids. They are subjected to destruction after deposition. This destruction mainly occurs within the first 100 meters through microbial ingestion or inorganic oxidation (Passey et al., 2010). This process leads to the formation of CO_2, H_2O, or NH_4 byproducts. Only a small portion of the organic compounds (less than 1%) escape this microbial destruction. Those compounds are preserved in non-hydrogen rich material and undergo subsequent thermal and chemical alteration. During the diagenesis process, those compounds react via condensation and sulfur vulcanization to form kerogen (Durand, 1980). Kerogen is defined as the solid portion of the organic matter

that is insoluble in organic solvents such as: ether, acetone, benzene, and chloroform (Durand, 1980). The portion of the organic matter that is soluble in an organic solvent is referred to as bitumen. This definition pertains to organic matter remaining after the rock is treated with HCl or HF solvents (Peters and Casa, 1994).

Tissot et al., (1974) classified kerogen into three types according to their physical and chemical properties. This classification is based on the van Krevalen diagram that was originally developed for coal (Tissot et al., 1974). The description of the different types of kerogen, their origins and the products expelled during maturation process is given in **Table 2.1** and **Fig 2.1**.

Table 2.1: Geochemical parameters describing kerogen type, origin and the product expelled during maturation based on their hydrogen to carbon ratio (H/C) and oxygen to carbon ratio (O/C) (modified from Peters and Cassa, 1994).

kerogen Type	Kerogen Origin	H/C	O/C	Main Expelled Products
I	marine and lacustrine algae	≥1.3	low	Oil
II	living organism and algae	1.2-1.5	average	Mixed oil and gas
III	terrestrial plant and humic	<1	high	Gas
IV	residual kerogen	0.5	high	None

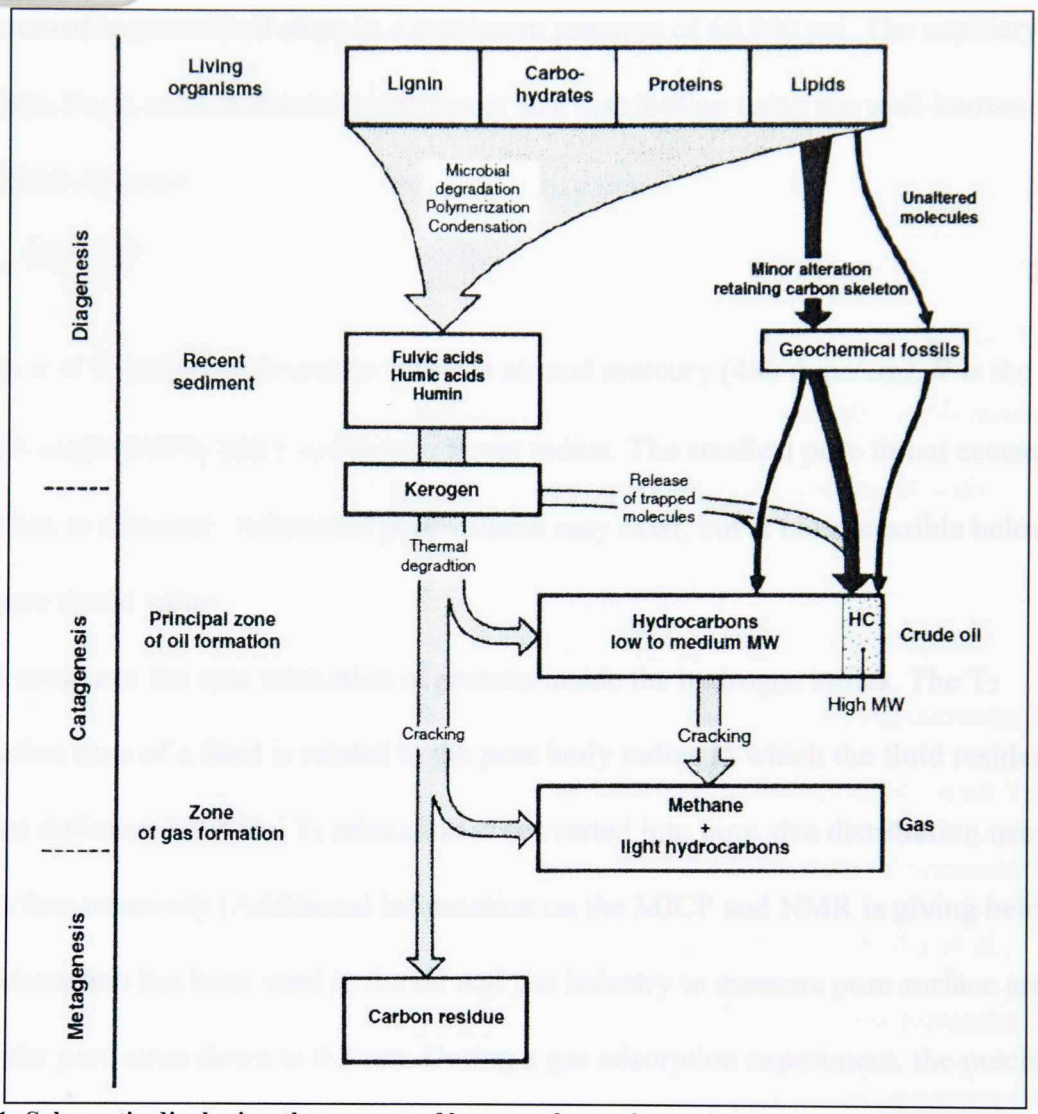

Fig 2.1: Schematic displaying the process of kerogen formation and subsequent chemical and thermal alternation. This picture also shows the byproduct form from organic matter conversion (Tissot and Welte, 1984).

2.3: Shale Microstructure

The storage and deliverability of shale reservoirs is controlled by their microstructure, large scale tectonic, and diagenetic processes. The methods currently used to analyze shale microstructure are challenging and expensive (Bustin et al., 2008). These methods include: Mercury Injection Capillary Pressure (MICP), Nuclear Magnetic Resonance (NMR), gas absorption, and Scanning Electron Microscopy (SEM) imaging. During an MICP test, the incremental volume of injected mercury is recorded at each pressure as it

is increased in prescribed steps to a maximum pressure of 60,000 psi. The capillary pressure, Pc, is converted into a pore throat size distribution using the well-known Washburn equation.

$$p_c = \frac{2\gamma \cos\theta}{r} \quad 2.1$$

Where γ is the interfacial tension between air and mercury (480 dyne/cm), θ is the contact angle (140°), and r is the pore throat radius. The smallest pore throat accessible is 3.8 nm in diameter. Additional pore volume may exist, but is not accessible below this pore throat value.

NMR measures the spin relaxation of protons inside the hydrogen atoms. The T_2 relaxation time of a fluid is related to the pore body radius in which the fluid resides. In the fast diffusion limit, the T_2 relaxation is converted into pore size distribution using the surface relaxivity (Additional information on the MICP and NMR is giving below).

Gas adsorption has been used in the oil and gas industry to measure pore surface area and infer pore sizes down to 0.3 nm. During a gas adsorption experiment, the precise volume of the uptake gas (N_2, CO_2, and H_2O) at constant temperature is recorded as a function of the relative adsorption pressure P/P_o where P_o is condensation pressure of the uptake gas at reservoir conditions. The surface area is calculated by applying the Branauer, Emmett, and Teller (BET) theory. BET theory is considered as an extension of Langmuir's theory to multilayer adsorption (Thommes, 2010). The pore size distribution derived from gas adsorption is computed from the traditional Barrett-Joyner-Halenda (BJH) method for slit pores (Barett et al., 1951). This method is based on the Kelvin equation which relates the change in vapor pressure during capillary condensation to the radius of the liquid-vapor meniscus (Kulia, 2011). However, the

BJH method cannot be used to investigate microscopic pores whose pore diameter is less than 2 nm. Adesida et al., (2011) used the Density Functional Theory (DFT) and molecular simulation to model and characterize the pore distribution at the microscopic scale. Clarkson et al., (2012) compared the pore distribution derived from BJH and DFT method to the widely accepted MICP pore distribution and found the DFT method had better agreement with MICP pore size distribution. A similar observation was made by Tinni (2013), who suggested that the DFT slit provides the best agreement with experimental data.

Chalmers and Bustin (2008) and Ross and Bustin (2009) applied gas adsorption methods to investigate the relationship between the composition and microstructure of a mature gas shale from Canada. They observed an increase in microporosity with TOC content. This increase in microporosity is a reflection of the formation of connected pore systems within the organic matter during the diagenesis process. Kulia et al., (2012) relied on a similar method to study 19 samples from the Niobrara formation. The results from Rock Eval® pyrolysis analysis placed those samples in the immature to the early portion of the oil window. Kulia et al., (2012) reported a good correlation between the specific surface area and clays (smectite plus illite content).The lack of correlation between microporosity and TOC was explained by the fact that the samples obtained from Niobrara have not reached a thermal maturity threshold to develop pores inside the organic matter. Instead, the organic matter is absorbed into the clay during the sedimentation process and resulted in a decrease of surface area (Kulia et al., 2012). Tinni (2013) reported results similar to Kulia et al., (2012) for Haynesville, Wolfcamp and Avalon shales as shown in the **Fig 2.2**. Valenza et al., (2013) also studied the

change in shale microstructure as function of maturity for 30 North American shale samples using gas adsorption and geochemical methods. They also observed an increase in nanopores with maturity. This increase in porosity is also related to the cracking of kerogen and bitumen under high pressure and temperature to form hydrocarbon molecules.

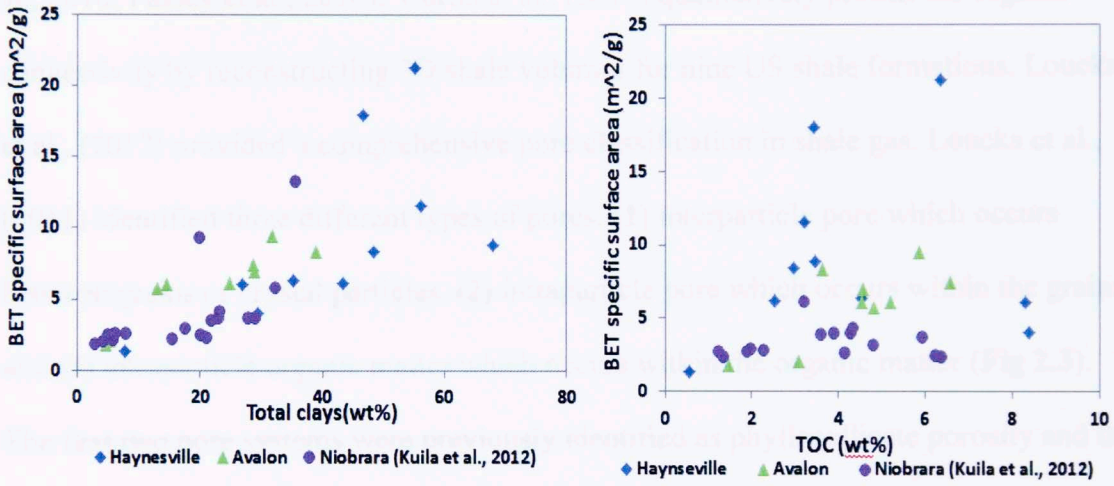

Fig 2.2: Specific surface area as function of total clays a) and TOC b) for the Haynesville, Wolfcamp, Avalon and Niobrara shale. No relationship exists between specific surface area and TOC. The surface area is affected by the total clay content of the sample (Tinni, 2013).

Recent improvements in ion milling and SEM technologies have provided the ability to visualize the shale microstructure. In order to obtain an image, the ion milled sample is coated with gold or carbon and irradiated with high energy electrons. These electrons are accelerated from an electron gun across high voltages that range from a few hundred to 40 Kv (Curtis et al., 2010). Significant research interest in exploring micro-and nano-pore sizes has been reported in recent years (Wang and Reed, 2009; Chalmers et al., (2009, 2012); Schieber et al., 2010; Slatt and O'Brien, 2011; and Curtis et al., (2011, 2012, 1013).

This increase in imaging studies has improved our understanding of shale microstructure and pore structure. Loucks et al., (2009) and Moncrieff (2009) were the first to document the presence of nanometer scale pores within the organic matter. The pore volume associated with the organic matter is substantial for some shale. This porosity system may account for up to 50 % of the total organic porosity (Sondergeld et al., 2010; Passey et al., 2010). Curtis et al., (2011) qualitatively probed the organic connectivity by reconstructing 3D shale volumes for nine US shale formations. Loucks et al., (2012) provided a comprehensive pore classification in shale gas. Loucks et al., (2011) identified three different types of pores: **(1)** interparticle pore which occurs between grains or crystal particles, **(2)** intraparticle pore which occurs within the grains, and **(3)** intraparticle organic matter which occurs within the organic matter (**Fig 2.3**). The first two pore systems were previously identified as phyllosyllicate porosity and the pore within the organics was identified as organophyllic porosity by Curtis et al., (2010). The latter porosity system is believed to develop during the shale maturation process. According to Dow (1977), a vitrinite reflectance of 0.6 % Ro has to be reached before the conversion from bitumen (kerogen) to hydrocarbon starts. The primary and secondary cracking of kerogen and bitumen leads to formation of oil and gas under the effects of pressure and temperature (Jarvie, 2001). However, this interpretation oversimplified the process of hydrocarbon formation during maturation (Curtis et al., 2012). Curtis et al., (2013) studied the microstructure of eight samples from Woodford over a range of maturities from 0.51 to 6.3 % Ro (**Fig 2.5**). The images reveal the absence of organic porosity for the samples that have low vitrinite reflectance (< 0.9 % Ro) and the presence of organic porosity for samples that have higher vitrinite

reflectance (>1.23% Ro). However, the 2 % Ro sample did not show any organic porosity. Furthermore, one sample that has a 1.28% Ro exhibited areas of organic porosity alongside (within a few microns) areas that do not have any organic porosity. These observations suggest that the maturation is a complex process which depends on both the organic type and the compaction experienced by the rock (Curtis et al., (2013).The images also reveal some features peculiar to the shale samples located in the oil window: the presence of fractures contained only within the organic matter (see **Fig 2.4**). Subsequent examination of oil producing shale has confirmed the lack of organophyllic porosity and the presence of the fracture porosity within the organic. Those fractures have not been observed in gas shale (Curtis et al., 2013). These fractures can provide high conductive paths for fluid migration. Their contribution needs to be taken into account since they can be affected by stress.

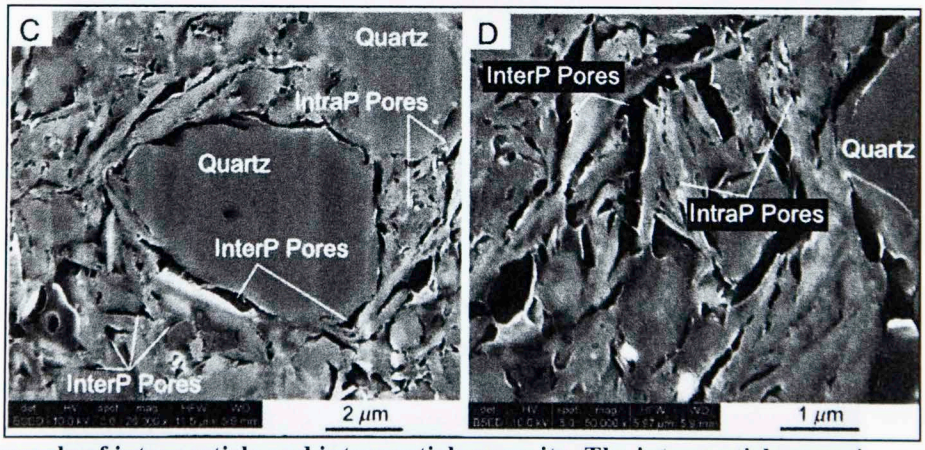

Fig 2.3: Example of interparticle and intraparticle porosity. The interparticle porosity occurs at the contact between the grain and intraparticle are located at the cleavage planes between the clay particles (Loucks et al., 2012).

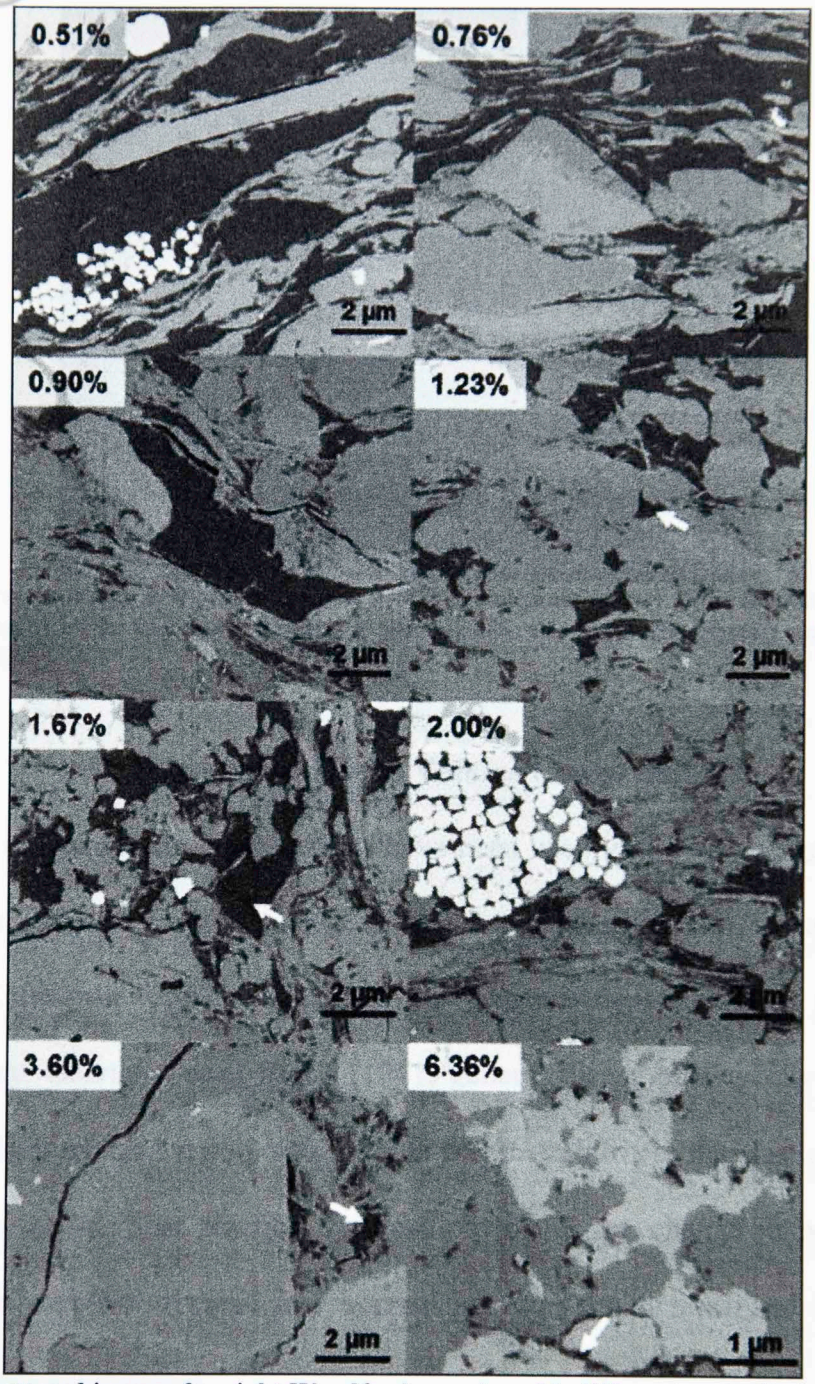

Fig 2.5: Back scattered images for eight Woodford samples with different maturity levels indicated by their % vitrinite reflectance. Note the lack of porosity for the immature samples and the presence organic porosity for mature sample depicted with a white arrow (Curtis et al., 2012).

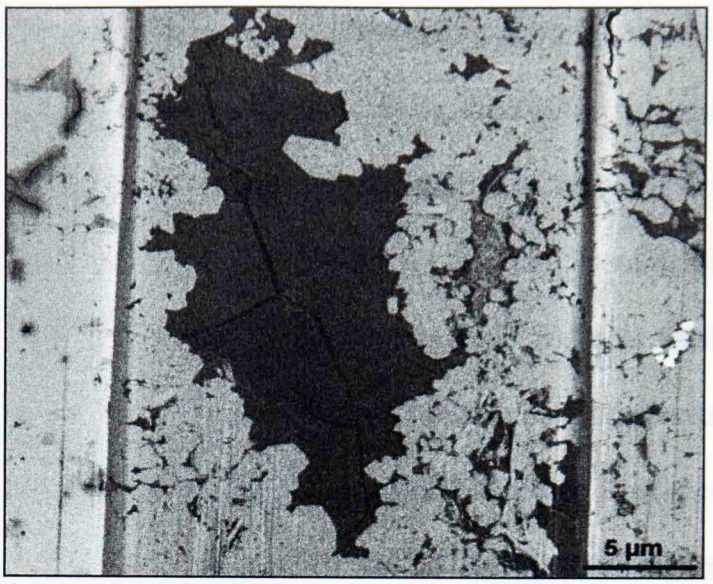

Fig 2.4: Backscatter image of fracture located within the organic matter. This fracture extends only within the organic matter and ends abruptly at the boundary between the organic and inorganic (Curtis et al., 2013).

2.4: Overview of Pore Volume Compressibility

Pore volume compressibility correlations have been used in the oil and gas industry to determine the extent of porosity change as function of pressure change during reservoir production. Geertsma (1957) recognized the pressure dependence of pore volume compressibility. Geertsma used Biot's (1941) general theory of elasticity to derive an expression which relates the pore and the bulk compressibility to the elastic deformation of the porous media. This practical formulation relates the change in pore and bulk volumes to the applied external and internal pressure for an idealized isotropic and homogenous porous material:

$$\frac{dV_p}{V_p} = C_r dp + \frac{1}{f}(C_b - C_r)(d\sigma - dp) \qquad 2.2$$

Where V_p is the pore volume, C_b is the bulk compressibility, C_r is the matrix compressibility, p is the pore pressure, σ is the confining pressure, and $f = \frac{v_p}{v_b}$.

The pore volume compressibility due to confining pressure, C_P^C, can be measured by keeping the pore pressure constant while varying the confining pressure; Hall (1953) referred to this as "formation compaction." Hall also reported a good correlation between the formation compaction and porosity for ten consolidated sandstones and limestones. This correlation is only valid for reservoir rocks at shallow depths. This correlation was used by the Bureau of Mines to determine the apparent compressibility of the Woodbine aquifer where the compressibility values enabled the prediction of the performance of this reservoir (Hall, 1953). van der Knapp (1959) extended the work of Biot and Geertsma (1957) for the nonlinear stress-strain behavior. They related the bulk and pore volume changes to the changes in the effective pressure. The compressibilities of the rock samples were dependent on the difference between the internal and external pressure as well as the porosity. van der Knapp (1959) developed an empirical relationship that related the pore volume compressibility to the porosity for 23 consolidated limestone samples from the same well. He also noted the influences of fluid type in the measurement of elastic property and the impact of compressibility in the calculation of the propagation rate of acoustic waves in the subsurface (van der Knapp, 1959). Similar previous observations were reported by Born and Owen (1935). Newman (1973) investigated the pore volume compressibility of over 256 rock samples from 40 different reservoirs. Newman also compiled over 79 compressibility measurements from published data. The samples were composed of unconsolidated, friable, and consolidated sandstones and limestones that have porosities ranging from 1 to 35%. The samples were cleaned and saturated with refined oil. The pore compressibility values for the different samples were reported at *in situ* pressure

conditions. The estimated reservoir pressure was equal to three quarters of the lithostatic pressure and the lithostatic pressure was computed assuming a lithostatic gradient of 1 psi/ft. **Fig. 2.6** shows the plot of pore volume compressibility and porosity. Hall's correlation was also included. Hall's correlation shows a decrease of compressibility with increasing porosity. Hall's relationship was deemed fortuitous by Zimmerman (1984) since it does not follow the behavior predicted by the theory of poroelasticity. Neither Fatt (1957) nor Newman (1973) found any consistent correlation between pore volume compressibility and porosity. Newman (1973) concluded that the measured pore volume compressibility displayed a wide variability. This wide variability precluded the establishment of a general compressibility-porosity relationship. Pore volume compressibility-porosity correlation can be determined only for well consolidated sandstones that have similar burial histories (Newman, 1973). A fundamental equation that related formation compressibility and porosity was developed for consolidated sandstone and limestone. The proposed hyperbolic equation has the following form for consolidated sandstones with porosity between 2 and 23% (Craft and Hawkins, 1991):

$$C = \frac{97.32 * 10^{-6}}{(1+55.9821*\varphi)^{1.43}} \qquad 2.3$$

and for carbonates with porosity between 2 to 33%:

$$C = \frac{0.8535}{(1+2.467*10^{6}\varphi)^{0.93}} \qquad 2.4$$

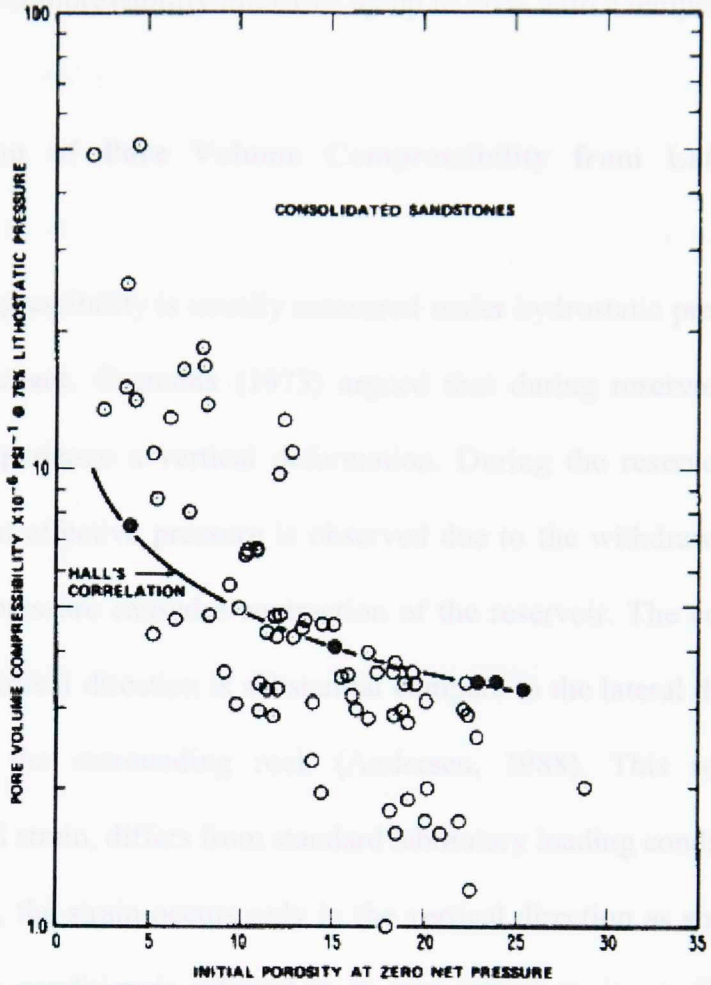

Fig 2.6: Pore volume compressibility reported at 75 % of the lithostatic pressure as a function of porosity for the 79 consolidated sandstone sample. The Hall correlation (solid line) is also included. Note the presence of correlation between the porosity and the pore volume compressibility for the consolidated sandstone samples (Newman, 1973).

Zimmerman (1991) showed that reservoir rocks, e.g. sandstones, followed the effective pressure law introduced by Terzaghi (1936). He experimentally verified this by computing the pore volume compressibility as a function of effective pressure on similar samples used by Greenwald (1981). Zimmerman also developed a method of correlating the four compressibilities of a porous material using the low frequency theory of elasticity. Von Gonten and Choudhary (1969) investigated the effect of the temperature on pore volume compressibility, and showed experimentally that there is a dependence of compressibility on temperature in a limited number of rock samples.

They noticed that compressibility increases by up to 20% with a temperature increase of 400° F.

2.4.2: Conversion of Pore Volume Compressibility from Lab to Reservoir Conditions

Pore volume compressibility is usually measured under hydrostatic pressure because of the ease measurement. Geertsma (1973) argued that during reservoir depletion, the reservoir only experience a vertical deformation. During the reservoir depletion, an increase in the net effective pressure is observed due to the withdrawal of pore fluid. This increase in pressure caused a contraction of the reservoir. The contraction of the reservoir in the vertical direction is substantial compare to the lateral direction where it is contained by the surrounding rock (Andersen, 1988). This reservoir loading condition, uniaxial strain, differs from standard laboratory loading condition.

In the subsurface, the strain occurs only in the vertical direction as shown below (**Fig 2.7**). This loading condition is referred to as zero lateral strain condition or uniaxial strain. Teeuw (1971) developed a theoretical expression for isotropic material to correct observations from hydrostatic loading to those for uniaxial loading using the following equation:

$$\sigma_{un} = \frac{1}{3}\left(\frac{1+\vartheta}{1-\vartheta}\right)\sigma_n \qquad 2.5$$

Where σ_{un}= uniaxial pressure

σ_n= hydrostatic pressure

ϑ=Poisson ratio

Nieto and Evans (1994) argued that uniaxial compaction correction using the Teeuw's method is not practical. Instead, *in situ* stress provides a reliable estimate for the

correction and should be used when fracture gradient is available. Teeuw's correction provides only the lower limit on the effective total stress (Nieto and Evans, 1994).

Another method of correction for isotropic rock was introduced by Andersen (1988). This method which simulates more accurately the reservoir loading condition uses the following three steps to correct for this loading condition:

Step1: Curve fit the hydrostatic data to the power law relationship based on stress versus pore volume strain relationship.

$$\Delta V_p = A_n(\sigma_c^n - \sigma_0^n) \qquad 2.6$$

In which:

ΔV_p= change in pore volume as function of stress

A_n= coefficient of fit to hydrostatic data

σ_c= net overburden stress

σ_0 = stress at initial laboratory strain condition

n= power law coefficient

Step 2: Calculate the pore volume using the following equation:

$$\Delta V_p^* = R_{hu}A_n(\sigma_c^n - \sigma_0^n) \qquad 2.7$$

In which R_{hu} is the hydrostatic to uniaxial correction factor. This factor is equal to

$$R_{hu} = \frac{1}{3}\left(\frac{1+\vartheta}{1-\vartheta}\right)$$

where ϑ is Poisson ratio.

Step 3: Calculate the predicted uniaxial pore compressibility using the following expression:

$$C_p^* = \frac{nR_{hu}A_n\sigma_c^{n-1}}{1-\Delta V_p^*} \qquad 2.8$$

where C_p^* is the pore volume compressibility corrected (Andersen, 1988).

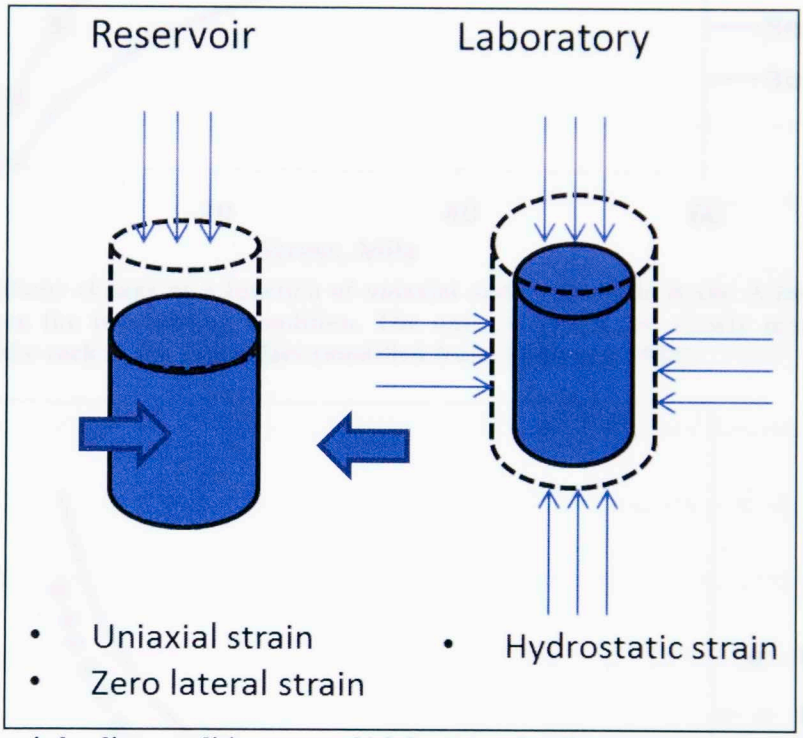

Fig 2.7: a) Reservoir loading condition versus b) laboratory loading condition. In the laboratory, the rock experience stresses in all directions compared unidirectional stresses in the reservoir.

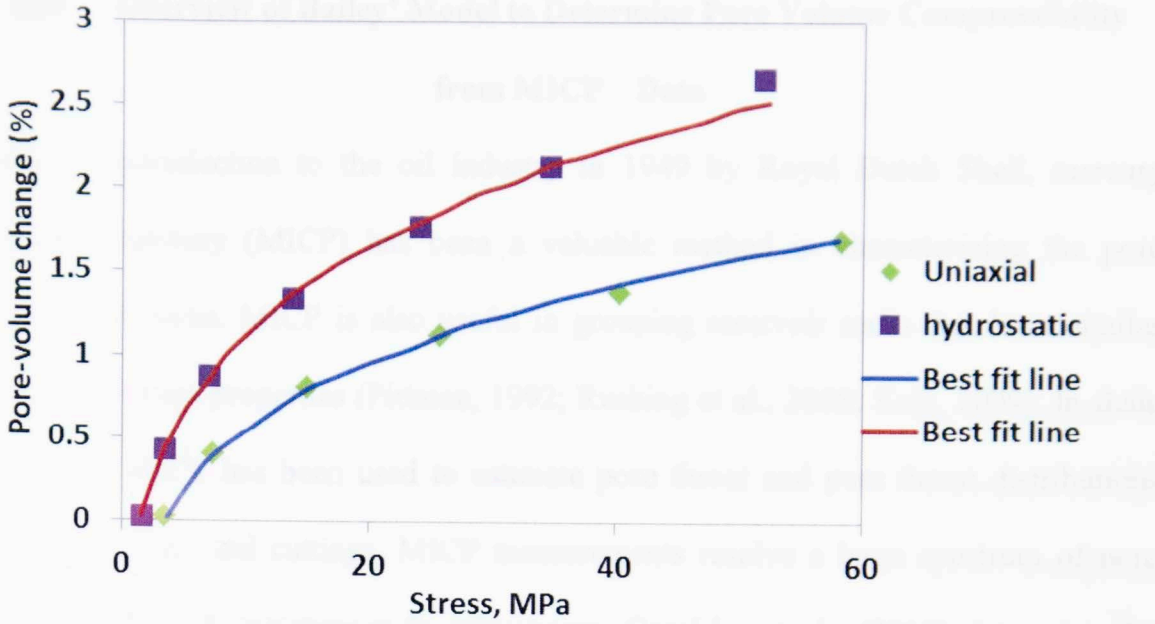

Fig 2.8) Pore volume change as a function of uniaxial and hydrostatic stress. A large difference is observed between the two loading condition. The uniaxial strain test closely matched the stress experienced by the rock in the subsurface (modified from Andersen, 1988).

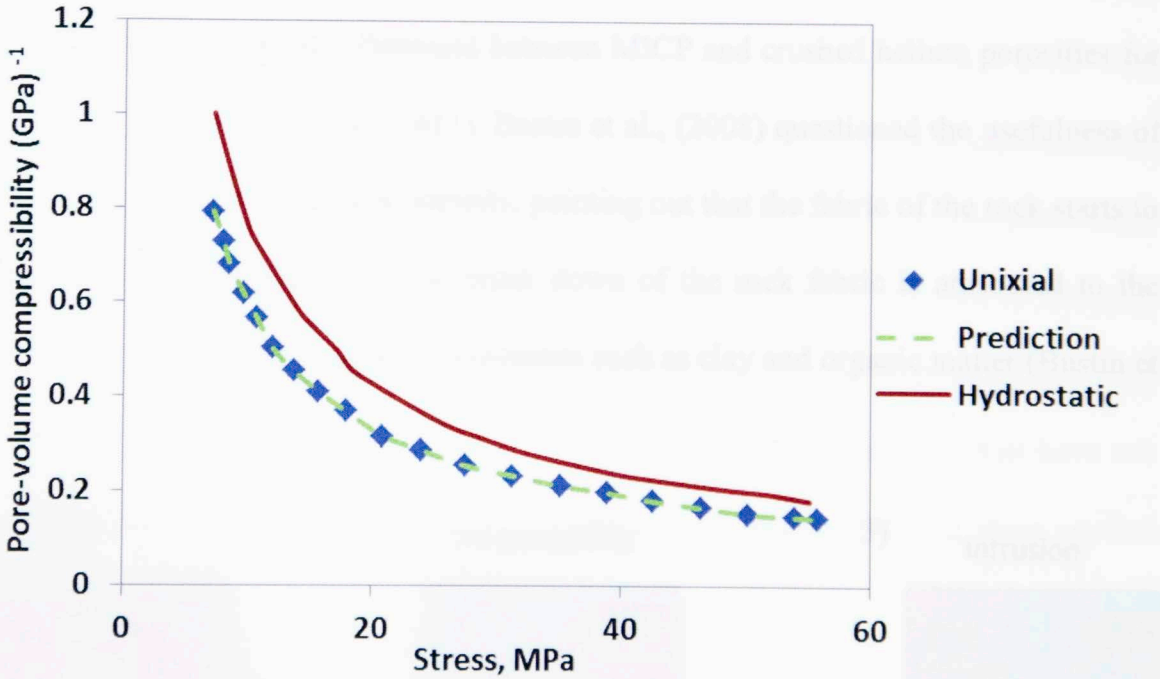

Fig 2.9) Pore volume compressibility changes as the function of stress for a uniaxial and hydrostatic test. The Andersen (1988) model enabled the transform from the hydrostatic test into uniaxial test which more closely mimics the reservoir conditions. This plot also shows the extent of the error when using hydrostatic test to predict compressibility.

2.5: Overview of Bailey' Model to Determine Pore Volume Compressibility from MICP Data

Since its introduction to the oil industry in 1949 by Royal Dutch Shell, mercury injection capillary (MICP) has been a valuable method in characterizing the pore structure of rocks. MICP is also useful in grouping reservoir rocks that have similar flow and storage properties (Pittman, 1992; Rushing et al., 2008; Kale, 2009). In shale reservoirs, MICP has been used to estimate pore throat and pore throat distributions from core plugs and cuttings. MICP measurements resolve a large spectrum of pore throat sizes, from macropores to micropores. Comisky et al., (2011) determine the optimum sample size (-20+35 mesh size) to measure porosity accurately using MICP and reduced the observed differences between MICP and crushed helium porosities for shale samples (Comisky et al., 2011). Bustin et al., (2008) questioned the usefulness of MICP to measure pore size and porosity, pointing out that the fabric of the rock starts to break down at high pressure. This break down of the rock fabric is attributed to the presence in large quantity of soft components such as clay and organic matter (Bustin et al., 2008).

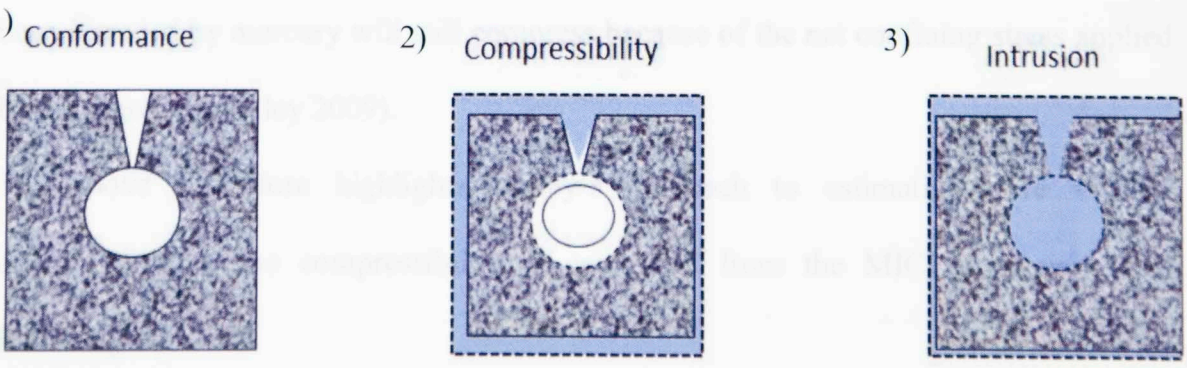

Fig 2.10: Graphically representation of the different stages of pore compressibility during MICP experiment according to Bailey (2009). Sequence shows 1) Hg conforming to the sample geometry, 2) Hg unable to enter the pores, causes compression of the pore, and 3) once Hg intrude the pore, pressure become equalized and the pore no longer compresses.

Bailey (2009) proposed a model to determine pore volume compressibility from MICP. This compressibility is actually an "incremental" or "instantaneous" compressibility. A schematic of his model is shown in **Fig 2.10**. During the MICP measurement, the sample is first subjected to a vacuum to remove any moisture or air present inside sample and the penetrometer. The net stress applied on the sample is zero. Mercury is introduced into the cell at small pressure increments. This initial volume of mercury at low pressure will conform to any rough surface, textures, or unconformities on the external surface of the sample. This false initial intrusion is corrected using the procedure for conformance correction (Bailey, 2009). As the mercury pressure is increased, but, still below the critical intrusion pressure for a given pore throat, the mercury will create an increase in the net confining stress surrounding a pore. This increase in pressure will lead to a decrease in pore volume if the matrix is assumed to be incompressible. The decrease in pore volume will be proportional to the compressibility of the pore space. Once, the mercury pressure reaches the entry pressure of the pore throat, the mercury will intrude the connected pore volume. The pore pressure will then be equal to the external mercury pressure; however, the remaining pores that have not been intruded by mercury will still compress because of the net confining stress applied by the mercury (Bailey 2009).

The above procedure highlights Bailey's approach to estimating pore volume compressibility. The compressibility is calculated from the MICP data using the following equation:

$$C_p^c = \frac{-1}{v_{Hg'}}\left(\frac{dv_{Hg'}}{dP}\right) \qquad 2.9$$

Where v_{Hg}, the portion of the pore space which has not been intruded by mercury and P the mercury confining pressure. The compressibility dependence on P can be modeled with a power law function. The solution suggests that there is a linear relation, in log space, between the mercury pressure and the pore volume compressibility as displayed by equation **2.10**. Any deviation from the linear relationship is caused by either fluid conformance at low pressure or mercury intrusion at high pressure as illustrated in **Fig 2.11**.

$$C_p^c = C_{po} P^{-m} \qquad \textbf{2.10}$$

Taking the log of **2.10** yields:

$$log(C_p^c) = log(C_{po}) - mP \qquad \textbf{2.11}$$

where C_{po}, m and P are, respectively, the log of the y-intercept, the slope, and the mercury capillary pressure.

In general, shales exhibit a high entry pressures (~10,000 psi) compared to conventional reservoir rock. This high entry pressure leads to a large and well defined compressibility interval for shale as shown in **Fig 2.11**.

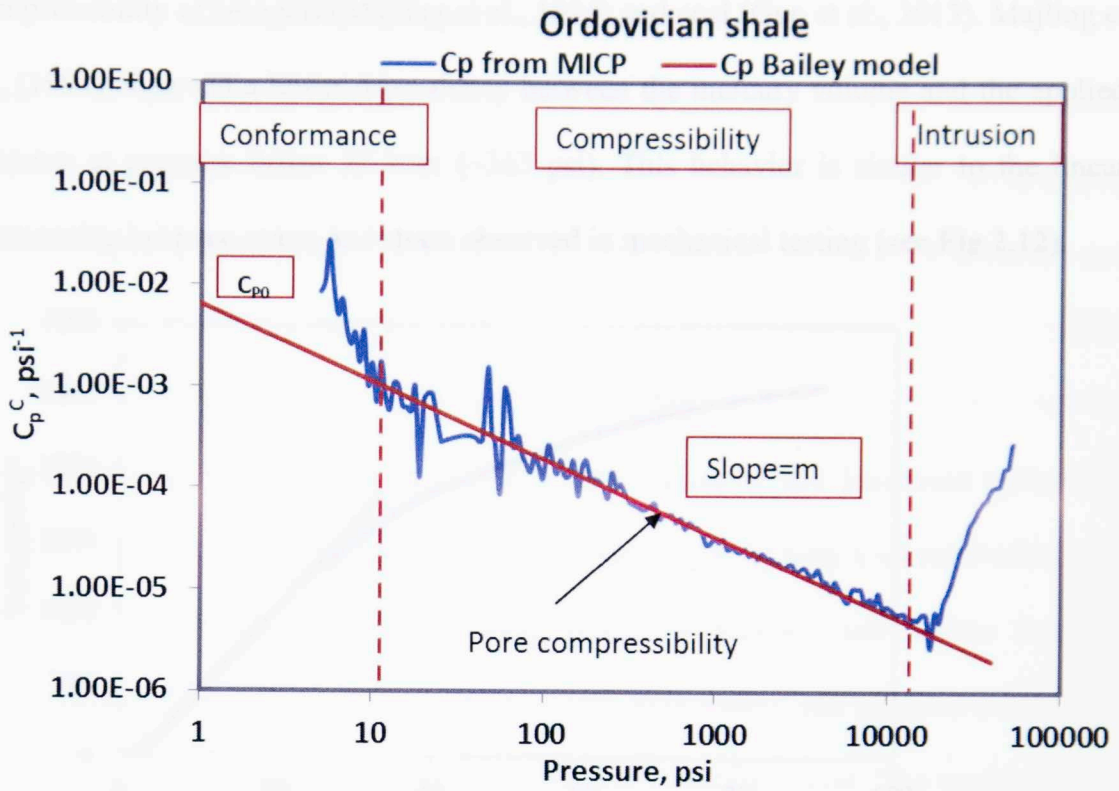

Fig 2.11: Bailey's (2009) pore volume compressibility as a function of pressure using MICP data. The compressibility shows a linear dependency on log pressure. The departure from the linear behavior is caused by either the conformance at low pressure or mercury intrusion at high pressure.

Bailey argued that the model previously described measures the pore volume compressibility in reservoir rocks. However, this model has several limitations. The mercury applied a net confining pressure that results in a bulk volume decrease rather than a pore volume change. At each pressure stage, some portion of the pore volume is lost because of the collapse of pore throats or intrusion of mercury into pores, thus V_o is changing. Those pores no longer contribute to the total compression of sample. The compressibility is calculated based on the remaining pores which represent only a fraction of the initial total pore volume.

Compressibility measurements from MICP data have been applied in other science and engineering disciplines. In material science, MICP is used to determine the

compressibility of aerogels (Majling et al., 1994) and coal (Guo et al., 2013). Majling et al., (1994) observed a linear dependency between the mercury volume and the applied pressure at pressure below 25 bars (~363 psi). This behavior is similar to the linear relationship between stress and strain observed in mechanical testing (see **Fig 2.12**).

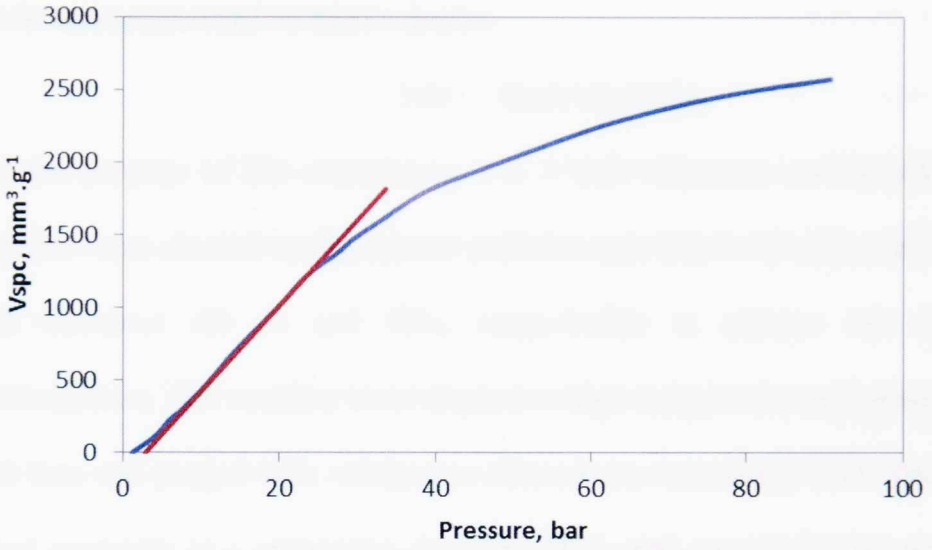

Fig 2.12: Injection pressure versus mercury specific volume Vspc, (mm^3/g), for aerogels. This plot shows a linear relationship between mercury volume and pressure at pressure below 25 bars. This linear relationship implies elastic deformation of the aerogel material. The nonlinear relationship observed above 25 bar implies a strengthening of the material (Majling et al., 1994).

Guo et al., 2013 derived an analytical equation to estimate coal compressibility from MICP:

$$C_p = \frac{1-\emptyset}{\emptyset} C_c \qquad 2.12$$

Where C_p is the pore compressibility, C_c is the matrix compressibility, and $\emptyset$ is the porosity of the material. They also observed a linear relationship between mercury pressure and mercury intrusion volume. This linear relationship was used to determine the matrix and the pore compressibility of coal. The estimated compressibilities displayed a trend which decreased with pressure.

3: EXPERIMENTAL PROCEDURES

Core plugs and crushed samples were used for routine petrophysical measurement. However, only plugs were used for NMR compressibility measurements. Petrophysical measurements such as mineralogy, porosity, total organic carbon (TOC), MICP and NMR were performed on these samples.

3.1: Core Cleaning

For the purpose of this experiment, 1 x 1 inch sandstone and limestone cylindrical samples were cleaned in the solvent extractor (see **Fig 3. 1**) with a mixture of toluene and methanol (80 % and 20%, respectively) to remove salt and/or residual hydrocarbons. The samples were cleaned at high temperature and pressure (130°C and 100 bar) and purged with nitrogen to remove any remaining fluid. The samples were dried overnight in a convection oven at 100°C until no weight loss was observed. In contrast, the shale samples were kept in their "as received" state.

Fig 3.1: High pressure and temperature solvent extractor

3.2: Mineralogy.

The complex mineralogical composition coupled with the presence of organic matter makes the study of shale reservoirs very challenging. Mineralogy is a major control on shale properties and microstructure. Several methods exist to determine mineralogy. These methods include X-ray diffraction (XRD), thin section analysis (TS) and Fourier transform infrared spectroscopy (FTIR). The method used to measure and quantify shale mineralogy in this study is the transmission FTIR spectroscopy (Griffiths and De Haseth, 1986); Sondergeld and Rai (1993); and Herron and Matteson, 1993; Ballard, 2007).

FTIR spectroscopy provides a fast and reliable means to determine shale composition (Sondergeld et al., 2010). FTIR spectroscopy is based on the vibration of covalent bonds caused by the absorption of infrared energy at specific frequencies. This atomic vibration occurs in mid-range infrared region (wavenumber between 400-4000 cm^{-1}) and the absorbance of each mineral depends on the bond type and quantity of mineral present. The latter is summarized by Beer's law:

$$\boldsymbol{A = \sum_{i=1}^{n} \varepsilon_i l c_i} \qquad 3.1$$

where A is the total absorbance, ε_i is the absorptivity of the i^{th} component, l is the absorption path length which correspond to the pellet thickness, and c_i is the concentration of the i^{th} component.

The measurements were performed on the Nicolet 6700 FTIR spectrometer manufactured by Thermo Scientific used in transmission mode. The FTIR measures the amount of energy transmitted (transmittance) through a thin disc containing a mixture of the unknown minerals and potassium bromide (KBr). The transmittance, T, is

converted to absorbance, A, using the following formula (Griffiths and De Haseth, 1986):

$$A = -log_{10}(\frac{T}{100}) \quad 3.2$$

Each mineral possess well-defined peaks which occur at specific wavenumbers (see **Fig 3.2**). For instance, the main peak for quartz occurs around 1100 wavenumber and calcite around 1450 wavenumber.

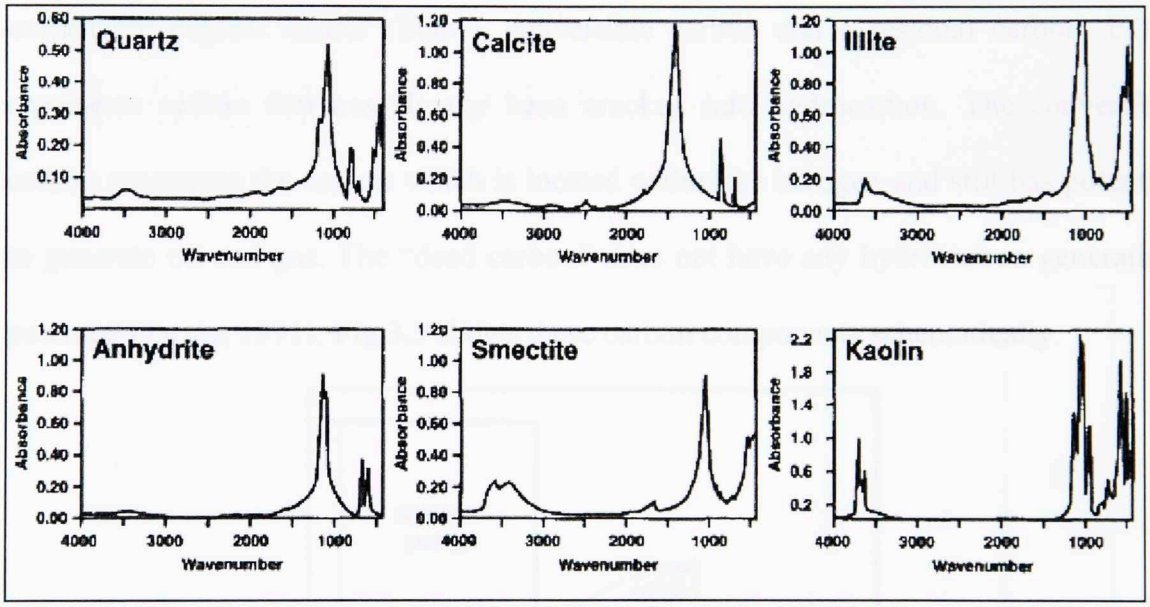

Fig 3.2: FTIR absorbance spectra of different minerals present in sedimentary rock. The position of the peak can be used to qualitatively distinguish between minerals. For instance Quartz peak occurs around 1100 wavenumber, calcite around 1450 wavenumber and most clay above 3000 wavenumber (Sondergeld and Rai, 1993).

These peaks in the diagnostic spectra enable us to qualitatively distinguish between the different minerals. The absorbance spectrum is inverted using the partial least squares method to quantify the mineral concentration for a given sample (Sondergeld and Rai, 1993; Ballard, 2007). KBr salt has no absorbance bands in mid-range infrared region. The measurements steps for the FTIR are provided in the **Appendix A**.

The FTIR spectroscopy is currently able to quantify over 16 minerals which include: quartz, calcite, dolomite, illite, smectite, kaolinite, chlorite, pyrite, orthoclase, oligoclase, mixed clays, albite, anhydrite, siderite, apatite, and aragonite (Ballard, 2007).

3.3: Total Organic Carbon (TOC) and Maturity Measurements

Total Organic Carbon (TOC) represents the hydrocarbon generation potential for source rock and is usually measured as weight percent (Jarvie, 1991). TOC is divided into extractable organic matter (EOM), convertible carbon and a residual carbon. EOM represents carbon that has already been cracked into hydrocarbon. The convertible carbon represents the carbon which is located within the kerogen and still has potential to generate oil and gas. The "dead carbon" does not have any hydrocarbon generation potential (Jarvie, 1991). **Fig 3.3** shows these carbon components schematically.

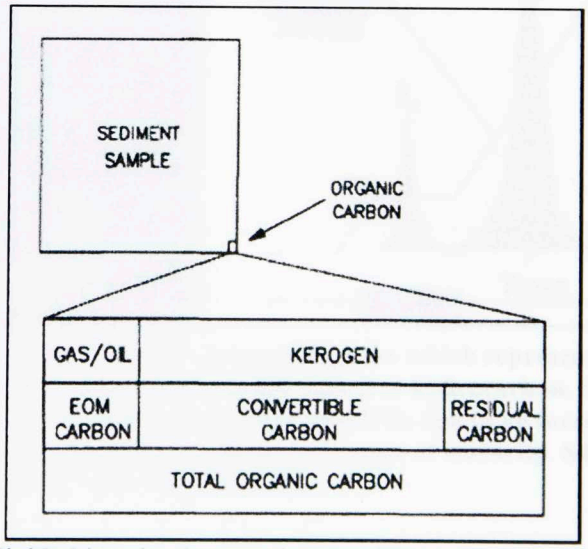

Fig 3.3: Organic matter divided into its three main components: EOM, convertible and residual carbon. The last two are part of the kerogen (Jarvie, 1991).

TOC is measured either by combustion of carbon using a LECO C844 TOC analyzer or through a combination of pyrolysis and oxidation with a Source Rock Analyzer (SRA)

(Fig **3.4 and 3.5**). The procedures for the measurements using the LECO and SRA are summarized in the **Appendix A.**

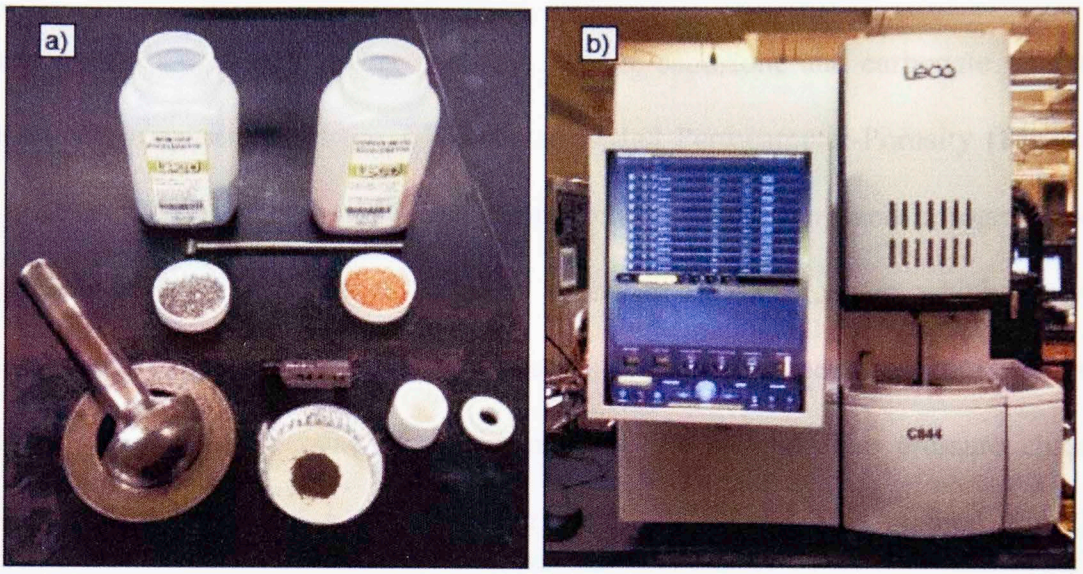

Fig 3.4: a) crucible, mortar, pestle, accelerators, catalysts, and sample used for preparing the sample before TOC measurement b) C-844 LECO TOC analyzer (Calderon, 2012).

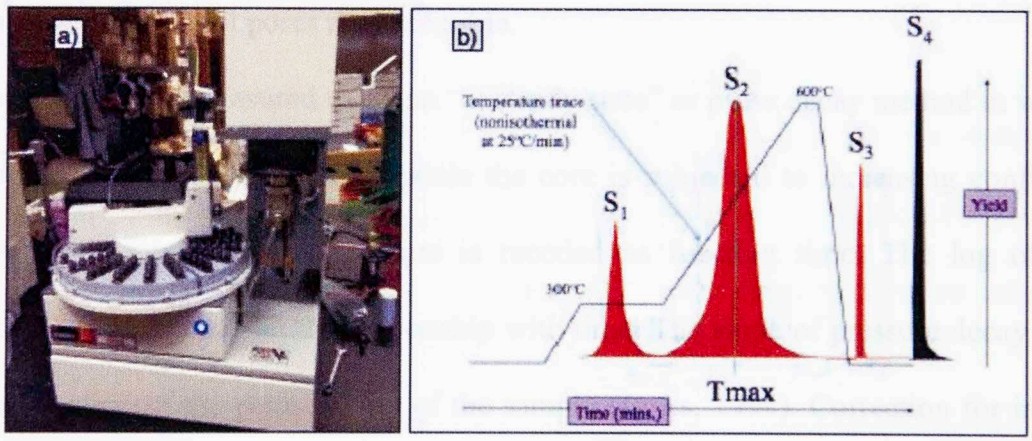

Fig 3.5: a) Source Rock Analyzer b) SRA pyrogram peaks which represents the product of the pyrolysis of the sample. The S_1 peak is associated with free hydrocarbon. S_2 and S_3 are associated with cracking of organic matter into hydrocarbon and CO_2 due to an increase in temperature. Tmax is associated with S2 peak and provide an indication of maturity. S4 represents the burning of the inert carbon or "dead carbon"(Jarvie, 1991).

3.4: Porosity and Permeability Measurements

Porosity is defined as the ratio of pore volume (Vp) over the bulk volume (V_B). It is often reported as fraction or a percent:

$$\phi = \frac{V_P}{V_B} \times 100 = \frac{V_B - V_G}{V_B} \times 100 \qquad 3.3$$

V_G is the matrix or grain volume.

Several methods exist to measure porosity. For the sandstone and carbonate samples, porosity was measured with the AP-608 Automated Permeameter-Porosity (**Fig 3.6**). This instrument measures porosity and permeability using helium and nitrogen gases, respectively. The porosity measurement is based on Boyle's Law in which a given volume of gas (helium) is allowed to expand at constant temperature from a known reference volume to the same volume containing the sample. The pressure change recorded is converted into a volume using the Boyle's Law. This method typically measures the total porosity assuming that the helium molecules are much smaller than the pores and almost all pores are accessible.

The permeability is measured using an "unsteady state" or pulse decay method in which nitrogen is flowed through a core while the core is subjected to increasing confining pressure. The nitrogen inlet pressure is recoded as function time. The log of the differential pressure has linear relationship with time. The slope of pressure decay with time is function of the permeability of the sample (Jones, 1994). Correction for inertia effects is also performed.

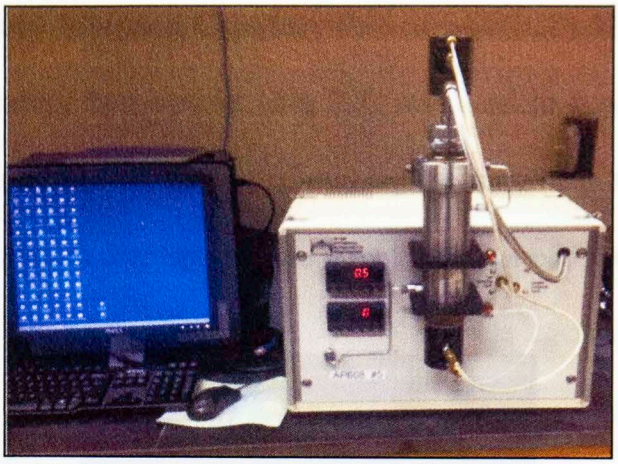

Fig 3.6: AP-608 Automated Permeameter-Porosimeter used for sandstone and limestone permeability and porosity measurements. The system has a confining pressure capacity of 10,000 psi.

The porosity and permeability of shales cannot be measured with AP-608 because of their low values. The porosity of the shale samples was measured with a low pressure pycnometer (LPP) following a procedure described by Karastathis (2007). The steps to measure porosity using LPP are summarized in the **Appendix A.**

This method also relies on Boyle's Law and gas expansion to measure the skeletal or grain density of samples. The measured grain volume and the calculated LPP porosity ($\bar{\phi}_{lpp}$) need to be corrected for the weight loss during the sample preparation using the following formula:

$$\overline{V_G} = V_G + \frac{\Delta_m}{\rho_G} \qquad \textbf{3.4}$$

$$\bar{\phi}_{lpp} = \frac{V_B - \overline{V_G}}{V_B} \qquad \textbf{3.5}$$

$\overline{V_G}$ is the corrected grain volume and Δ_m is the weight loss during sample preparation.

3.5: Mercury Injection Capillary Pressure (MICP) Measurements

An Autopore IV Mercury Porosimeter (**Fig 3.7**) was used in this study for the MICP measurements. This machine is capable of making measurement over a pressure range of 1 psi to 60,000 psi which correspond pore throat diameters of 360 to 0.003 μm.

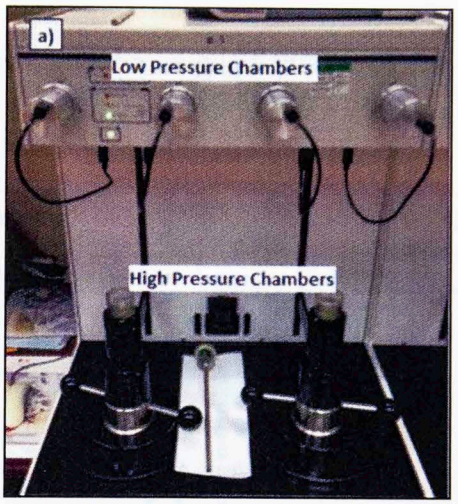

Fig 3.7: a) Autopore IV used for MICP measurement: Note the presence of four low pressure chamber on top and two high pressure chambers at the bottom (Asgarov, 2013).

The mercury volume is measured by the change of capacitance of the stem which behaves similar to a cylindrical capacitor in which the injected mercury serves as one electrode. The mercury volume is recorded at each predefined pressure step after pressure equilibrium is reached. The data is reported as incremental Hg intrusion volume versus capillary pressure (See **Fig 3.8a**). Typical mercury intrusion pressure for shales begins around 10,000 psi which corresponds to a pore diameter of about 18 nanometers (see **Fig 3.8b**).

A Blank and conformance errors have been identified as two common errors associated with MICP measurements. The blank error occurs at high pressure (above 10,000 psi) and is attributed to the compression of sample, mercury, and the penetrometer. A blank correction for the intrinsic components and machine is made by subtracting the

intrusion curve for a blank or completely mercury filled penetrometer (Sigal, 2009). A conformance error occurs at low pressure and is caused by the irregularities and roughness of the sample. The conformance error is significant for crushed and irregular shape samples that have high surface area. For plugs, the error due to conformance is usually insignificant; therefore, no conformance correction was applied to the capillary pressure curves. For crushed samples, a good review of the conformance correction is provided by Bailey (2009) and Comisky et al., (2011).

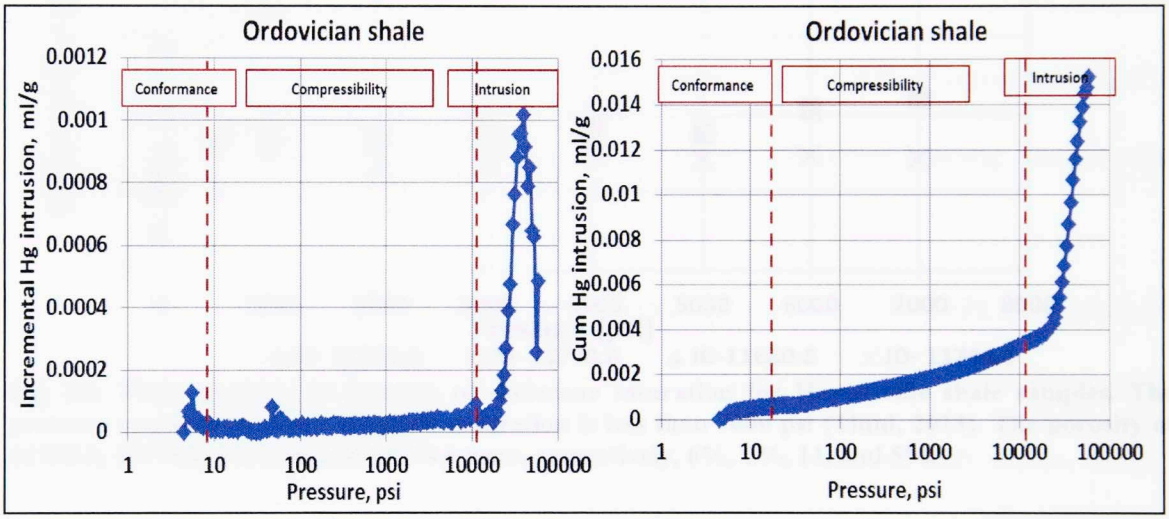

Fig 3.8: a) The incremental mercury intrusion as function of capillary pressure. b) The cumulative mercury intrusion as function of capillary pressure. The early part of the intrusion is dominated by conformance, followed by compressibility and intrusion at high pressure.

3.6: Sample Saturation Procedures

After cleaning and drying, the sandstone and limestone samples were placed in a steel pressure vessel and evacuated. The samples were saturated with 25,000 ppm NaCl brine solution. The pressure inside the cell was maintained at 2,500 psi for 24 hrs. After saturation, the weight of each sample was recorded.

Horizontal shale plugs, 1 inch long by 1 inch in diameter were placed inside a pressure vessel and evacuated for 2 hrs. The samples are then saturated with dodecane at 7,000

psi for 48 hrs. Following the saturation, the sample is weighed and gravimetric porosity is calculated. The selection of the saturation pressure was based on studies done by Odusina (2011) and Tinni (2012) in which they found that 7,000 psi saturation pressure is enough to reach complete saturation in most shales (see **Fig 3.9**).

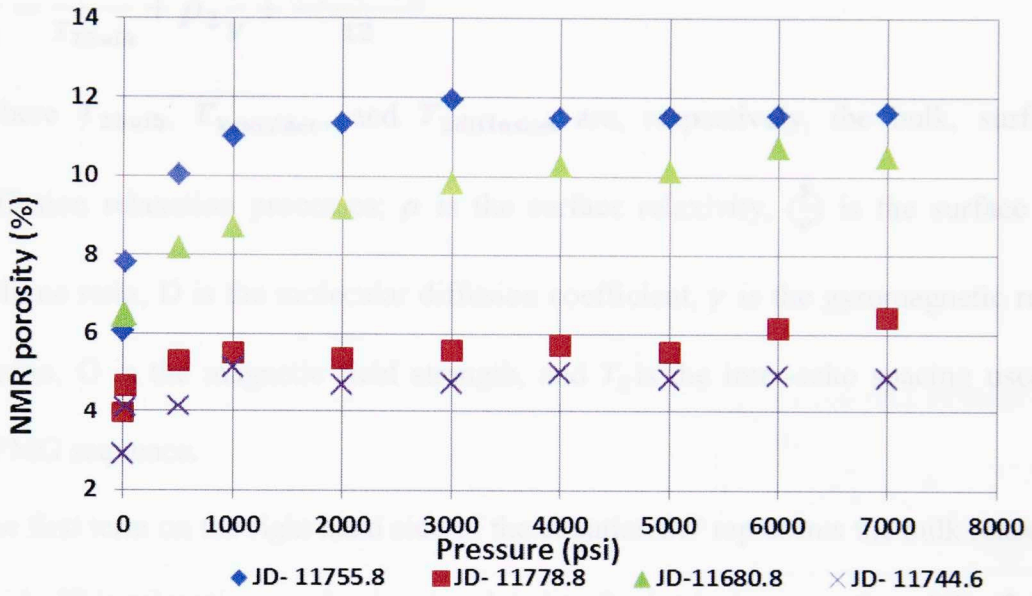

Fig 3.9: NMR porosity as function of dodecane saturation for Haynesville shale samples. The pressure required to reach complete saturation is less than 7000 psi (Tinni, 2013). The porosity of 11755.8, 11778.8, 11680.8, and 11744.6 were, respectively, 6%, 6%, 11, and 5%.

3.7: NMR Compressibility Measurement Procedures

Nuclear magnetic resonance or NMR has been instrumental in assessing storage type (Sigal and Odusina, 2011), fluid type (Washburn, 2013), and wettability (Odusina, 2011; Sulucarnain, 2013) in shale plays. In conventional plays, NMR has been used to provide information about the fluid type and content independent of lithology (Sondergeld et al., 2010). NMR measurements rely on the precession of protons whose frequency is controlled by an external magnetic field. Transverse T_2 relaxation is caused by the interaction between the magnetic field and protons. Three independent

mechanisms control the T_2 relaxation in porous media (Coates et al., 1999) are described by the following equations:

$$\frac{1}{T_2} = \frac{1}{T_{2bulk}} + \frac{1}{T_{2surface}} + \frac{1}{T_{2diffusion}} \quad 3.6$$

$$\frac{1}{T_2} = \frac{1}{T_{2bulk}} + \rho_2 \frac{S}{V} + \frac{D\gamma^2 D^2 T_E^2}{12} \quad 3.7$$

Where T_{2bulk}, $T_{2surface}$, and $T_{2diffusion}$ are, respectively, the bulk, surface and diffusion relaxation processes; ρ is the surface relaxivity, $(\frac{S}{V})$ is the surface to pore volume ratio, D is the molecular diffusion coefficient, γ is the gyromagnetic ratio of a proton, G is the magnetic field strength, and T_E is the inter-echo spacing used in the CPMG sequence.

The first term on the right hand side of the equation **3.7** represents the bulk relaxation of fluid. This relaxation mechanism is related to the intrinsic properties of the fluid, such as viscosity and chemical composition (Coates et al., 1999). In the bulk states, the T_2 relaxation of water and oil is much longer than water and oil in the porous the media (**Fig 3.10**). In the fast diffusion domain, the relaxation times for the fluid are dominated by the fluid interaction with the solid surface. This interaction leads to faster relaxation for water and oil (Brown and Fatt, 1956).

Compressing the sample forces fluids out of the pore space. In our configuration this excess fluid is forced into the larger cavities inside the Peek end caps in which the water has a slower relaxation time (see **Fig 3.12**). The contrast between the fast relaxation times of the pores and the slower relaxation of the bulk water yields to a measure of the fluid displaced as function of the applied pressure. The cumulative fluid displaced is converted into compressibility using equation **1.1**. The fluid displaced measured using

the NMR closely represents the internal fluid change that occurs within the pore space which is subjected to an increase effective pressure.

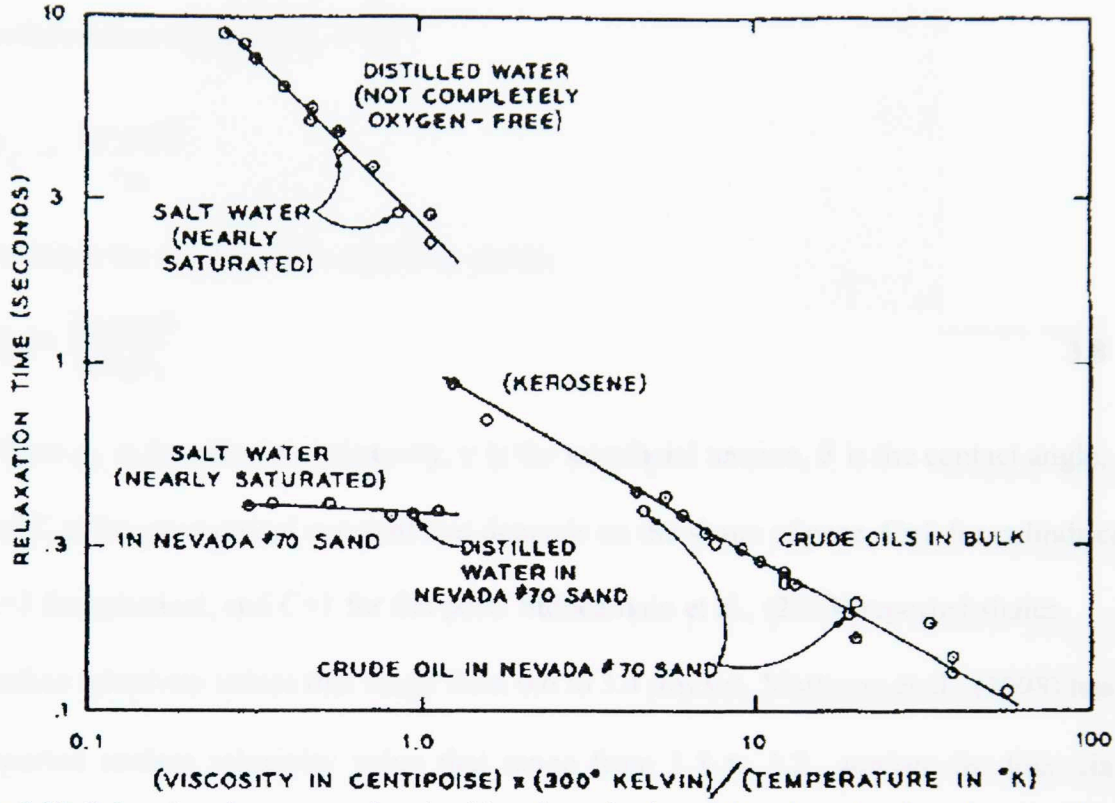

Fig 3.10: Relaxation time versus viscosity. Note the reduction of the relaxation time of water when it is in porous media compared to the bulk state (Dunn, 2002).

NMR T_2 distributions can be converted into pore size distribution, if the effective surface relaxivity is known. The T_2 relaxation time distribution closely matches the MICP pore distribution as noted by Kleinberg (1996), Straley et al.,(1997), Dastidar (2004), and Sulucarnain (2013). The fundamental differences between the NMR pore size distribution and the MICP is that NMR measures the pore body size, whereas, MICP measures the pore throat size. The effective surface relaxivity can be obtained by combining the Washburn equation and the NMR T_2 relaxation equation as shown below:

In the fast diffusion domain, equation **3.7** reduces to:

$$r_b = C\rho_2 T_2$$

where r_b is the pore body radius, r_{th} is the pore throat radius and ρ_e is the effective surface relaxivity and $\rho_e = \frac{r_b}{r_{th}}$

$$P_C = \frac{2\gamma \cos\theta}{r_{th}}$$

Combine the two previous equations yields:

$$\rho_e = \frac{2\gamma \cos\theta}{C P_C T_2} \quad \textbf{3.8}$$

Where ρ_e is the effective relaxivity, γ is the interfacial tension, θ is the contact angle, and C is the geometrical constant that depends on the shape of pore. C=2 for cylindrical, C=3 for spherical, and C=1 for flat pore. Sulucarnain et al., (2013) reported shales surface relaxivity values that range from 0.6 to 3.4 μm/sec. Matteson et al., (1998) has reported surface relaxivity value that range from 1.8 to 3.2 μm/sec for four clays mineral (kaolinite, illite, smectite and glauconite). Kaolinite and glauconite clays have the lowest and highest surface relaxivity, respectively.

Following the saturation, the samples were weighed for gravimetric porosity assessments. The samples were loaded inside a fiberglass pressure vessel (See **Fig 3.11b**).

Fig 3.11: a) NMR Geospec 2 manufactured by Oxford instruments. b) Fiberglass pressure vessel used to hold the sample during compressibility measurements.

NMR measurements were carried out in the Oxford Instruments GeoSpec2 2MHz spectrometer (**Fig 3.11a**). Routine systems calibration was performed before each measurement cycle. The initial spectra were acquired under atmospheric pressure. Initial spectra were obtained using the following parameters: signal to noise ratio (SNR) = 100 and inter-echo spacing T_E = 100 μs with no confining pressure. The same NMR parameters are used throughout the test. The experimental set up is shown below (**Fig 3.12**).

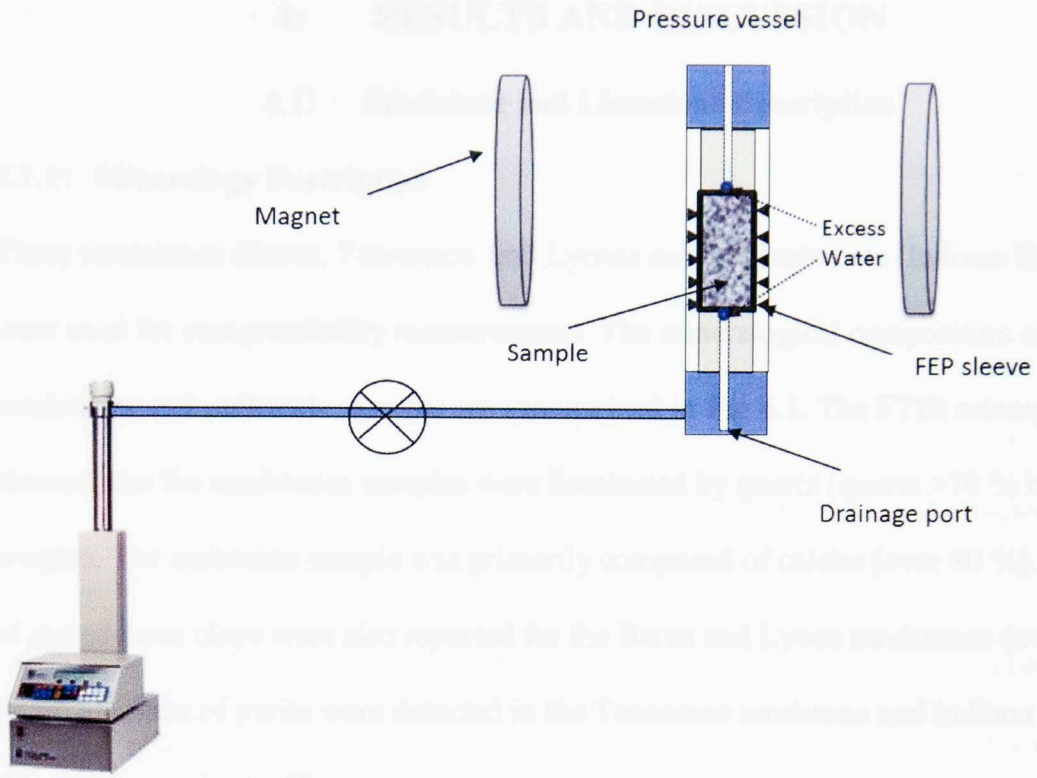

Fig 3.12: Experimental set up used to measure pore compressibility using NMR. The sample is jacketed in a FEP (fluororinated ethylene propylene) sleeve and placed between two end caps made of PEEK. A confining pressure ranging from 0-5000 psi is applied using a Teledyne Isco pump. The applied pressure causes the displacement of the fluid from pore space.

3.8: NMR Data Subtraction

In order to remove the signal associated with the pressure vessel and obtain the relaxation curve for the fluid, a subtraction on the raw NMR decay curve was performed in the time domain. The signal of pressure vessel was obtained without any sample present. The NMR signal of the sample plus the pressure vessel is subtracted from the pressure vessel signal using the TDA (time domain analysis) technique. TDA is more robust than simply differencing the spectra.

4: RESULTS AND DISCUSSION

4.1: Sandstone and Limestone Description

4.1.1: Mineralogy Description

Three sandstones (Berea, Tennessee, and Lyons) and one carbonate (Indiana limestone) were used for compressibility measurements. The mineralogical composition of the sandstones and carbonate samples are summarized in **Fig 4.1.** The FTIR mineralogy showed that the sandstones samples were dominated by quartz (quartz >70 % by weight). The carbonate sample was primarily composed of calcite (over 80 %). Traces of mixed layer clays were also reported for the Berea and Lyons sandstones (over 16%). Small amounts of pyrite were detected in the Tennessee sandstone and Indiana limestone samples (< 5%).

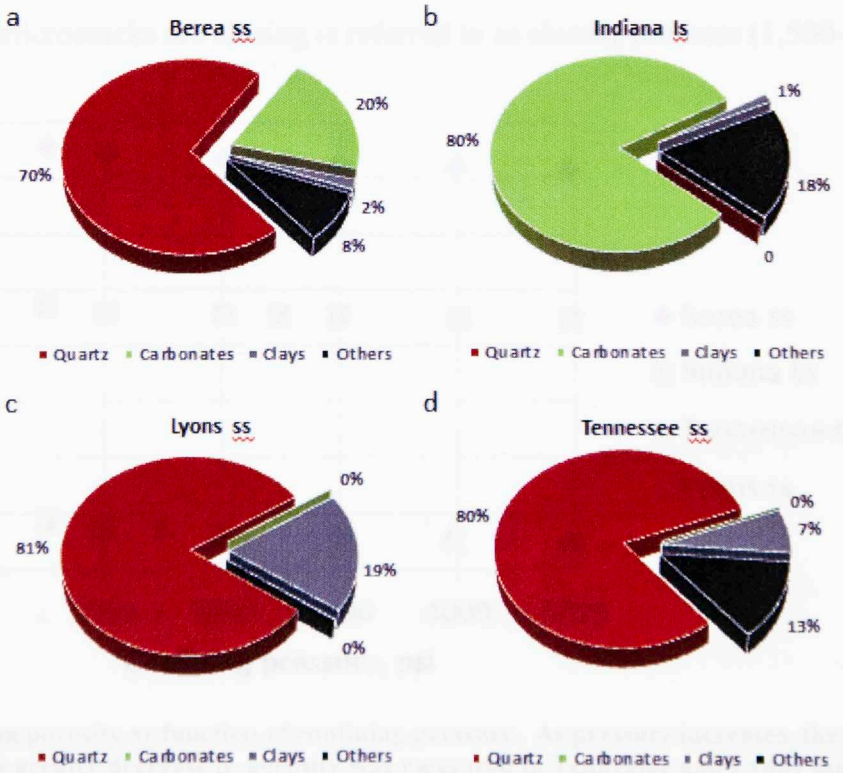

Fig 4.1: Average mineralogy composition for the a) Berea sandstone, b) Indiana limestone, c) Lyons sandstone, d) Tennessee sandstone. Quartz dominates the sandstones while calcite dominates in the limestone.

4.1.2: Porosity and Permeability Description

Porosity and permeability were measured for the sandstone and carbonate samples using the AP-608 Automated Permeameter-Porosimeter. **Fig 4.2** shows the dependence of Φ on the confining pressure. The rate at which the porosity decreased depends on the lithology, pore shape, and cementation. For instance, the highest porosity changes were recorded for Tennessee and Lyons sandstone (12% and 15 %) which have the lowest helium porosity. The lowest porosity change was recorded for the Berea sandstone and Indiana limestone (only 4% each); these samples have the highest porosities. The porosity variation at low pressure is greater than the porosity variation at higher pressure where it approaches an asymptotic value. The higher rate of porosity change noted at early time is attributed to the closing of microcracks. The pressure at which most of the microcracks are closing is referred to as closing pressure (1,500-2,500 psi).

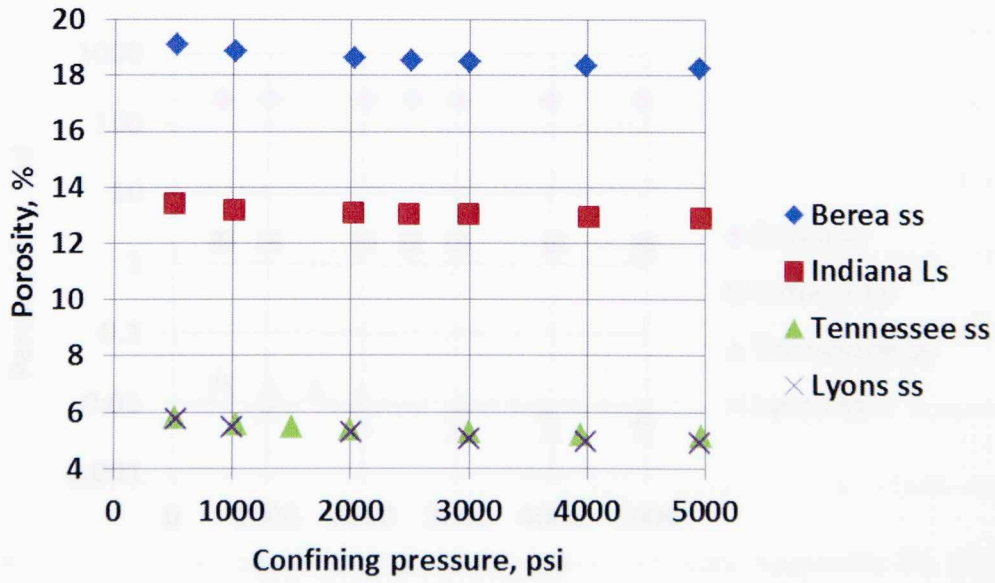

Fig 4.2: Helium porosity as function of confining pressure. As pressure increases, the porosity decreases. The greater decrease in porosity was measured in Tennessee and Lyons sandstone ($\Delta \Phi$ =12 and 15 % over 5000 psi, respectively).

While the porosity difference among this samples is only 15%, the permeability varies by a factor of 10,000 (see **Fig4. 3**). The permeability values range from 0.004 md to 220 md. The highest permeability was recorded for the Berea sandstone and lowest was recorded for the Lyons sandstone which also has the lowest porosity. According to Gangi (1978), the variation of permeability as function of pressure can be explained through asperity contact theory. The rate of change of permeability is different from the change of porosity. For instance, the Berea sandstone, which has a 4% decrease in porosity, experienced only a 2 % decrease in permeability. While, the Indiana limestone which also has a similar decrease in porosity has an 8% decrease in permeability. The highest decrease in permeability was recorded for the Tennessee and Lyons sandstone samples (64 % and 68 % respectively). Most porosity changes occur at pressure below 2,000 psi. **Table 4.2** give a summary of the porosity and permeability as function of confining pressure for the sample studied.

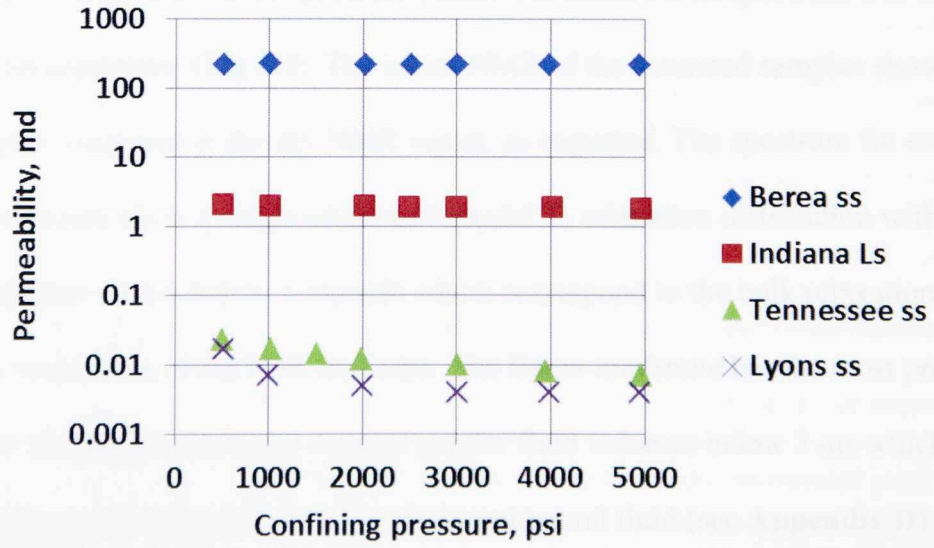

Fig 4.3 Klinkenberg corrected permeability as function of confining pressure. As pressure increases, the permeability decreases. The highest decrease in permeability was measured for the Tennessee and Lyons sandstones (Δk =64 and 68 % over 5000psi, respectively).

Table 4.1: Summary of porosity, permeability and mineralogy for sandstones and limestone samples. The porosity and permeability were reported at 5,000 psi confining pressure.

Samples	$\phi^{5000\ psi}$	$k^{5000\ psi}$	Quartz	Carbonates	Clays	$\frac{d\emptyset}{dp}$	$\frac{dk}{dp}$
	%	md	Wt %	Wt %	Wt %	$kpsi^{-1}$	$md.Kpsi^{-1}$
Berea ss	18.28	217	70%	20%	2%	0.16	1.039
Indiana Ls	12.93	2	0%	80%	1%	0.096	0.0348
Tennessee ss	5.12	0.007	80%	0%	7%	0.14	0.0032
Lyons ss	4.88	0.004	81%	0%	19%	1.15	0.0026

4.2 NMR Pore Volume Changes as Function of Pressures

The pore volume changes as function of pressures measured with NMR are similar to the actual fluid changes that occur in the reservoir during the depletion process. Therefore, NMR provides a reliable estimate of pore volume compressibility which closely matches the compressibility of reservoir rocks, assuming that the reservoir rocks obey the effective pressure law. After pressure saturating the samples with brine, they were loaded in the NMR pressure vessel. An initial NMR spectrum was acquired at room conditions (**Fig 4.4**). The initial NMR of the saturated samples shows a larger signal compared to the dry NMR signal, as expected. The spectrum for each of the sandstones show a single or minor bimodal T_2 relaxation distribution with a dominant peak that occurs below 3 seconds which correspond to the bulk relaxation of brine in the larger hole in the Peek end caps. The Berea sandstone has the most prominent peak. The Tennessee sandstone showed greater fluid volumes below 3 ms which corresponds to the cut off value between free fluid and bound fluid (see **Appendix D**). Fluids that have a T_2 relaxation time less than 10 ms are located in micropores (Dastidar, 2004).

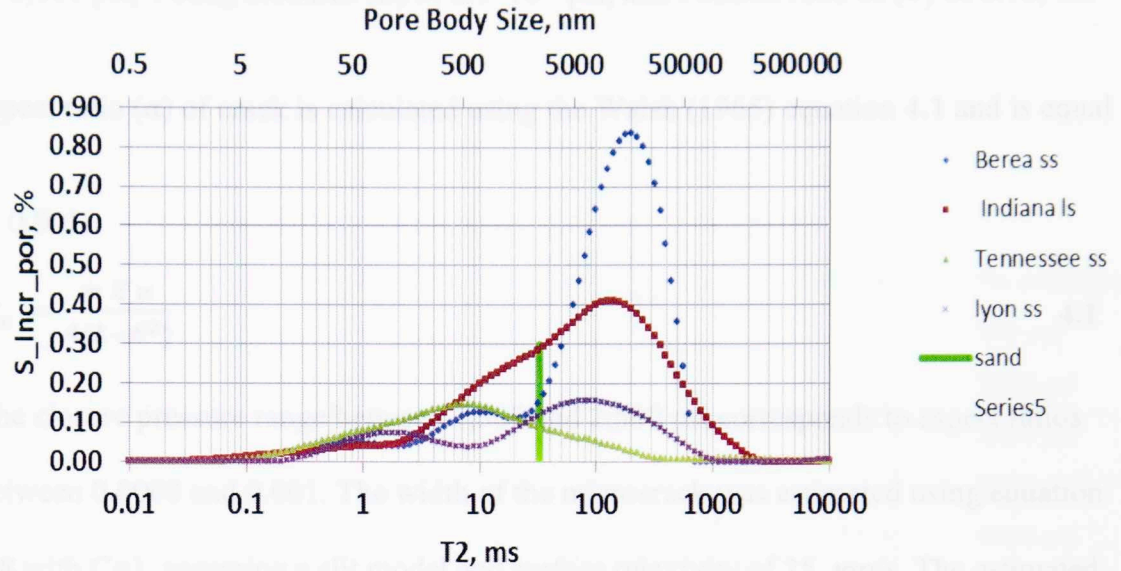

Fig 4.4: Incremental NMR porosity for the sandstone and limestone samples after 2500 psi saturation with brine. Note the bimodal distribution of T2 relaxation time with the most prominent peak corresponding to the Berea sample, the sample with the greatest porosity. The pore size scale was calculated using a surface relaxivity of 25 μm/s (Dunn, 2002).

The T_2 relaxation spectra for the core samples with changing confining pressure are displayed in Fig **4.5 –4.8 a**. In addition to the pore fluid volume change as a function of confining pressure, the NMR identified the pore sizes in which this reduction takes place. Several distinct features are evident in the plot of T_2 relaxation time as function of confining pressure. Most of the reduction in pore volume occurs at small T_2 relaxation times (1-3 ms) with a minor decrease in the prominent peak. Lastly, there is no change in the main T_2 peak relaxation time values. These observations suggest that the decrease in pore volume is taking place mostly in micropores or microcracks that have relaxation time less than 10 ms. The decrease of the prominent peak suggests that a minor pore volume change is occurring in the larger pore bodies. The closure pressures range between 1,500 and 2,500 psi. Assuming an average closure stress (σ_c)

of 2,000 psi, Young modulus (E) of $2.5*10^{-6}$ psi, and Poisson ratio of (ϑ) of 0.18, the aspect ratio (α) of crack is calculated using the Walsh (1965) equation **4.1** and is equal to 0.001:

$$\sigma_c = \frac{\pi E \alpha}{4(1-\vartheta^2)} \qquad \textbf{4.1}$$

The closure pressure range between 1,500 and 2,500 psi corresponds to aspect ratios between 0.0008 and 0.001. The width of the microcrack was estimated using equation **3.8** with C=1, assuming a slit model and surface relaxivity of 25 μm/s. The estimated width of the microcracks was less than 1 μm.

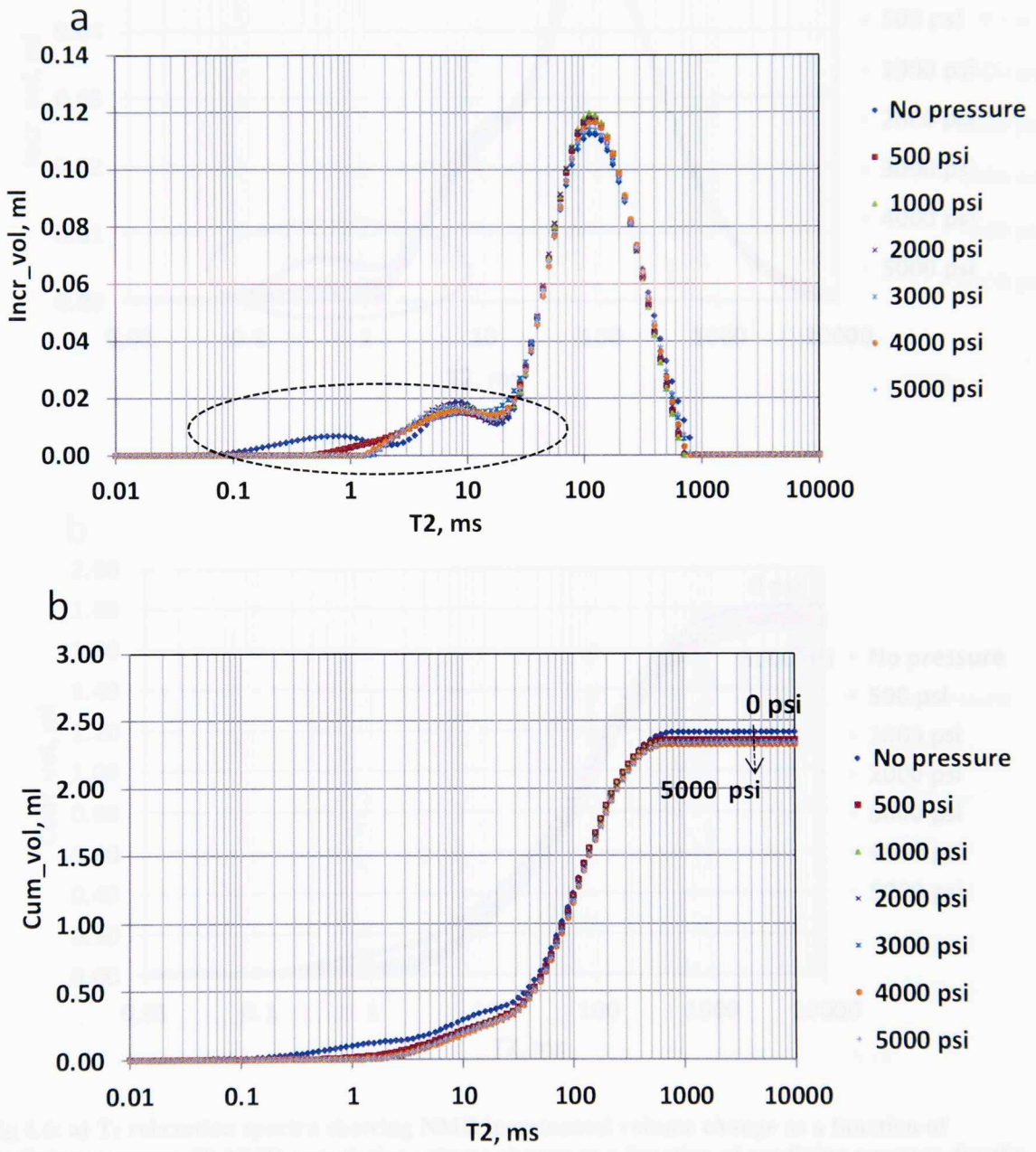

Fig 4.5: a) T_2 relaxation spectra showing NMR incremental volume change as a function of confining pressure. b) NMR cumulative volume change as a function of confining pressure for the Berea ss sample. Note the decrease in pore volume at small T_2 relaxation times (<13ms) and the decrease of the cumulative NMR pore volume as function of increasing confining pressure.

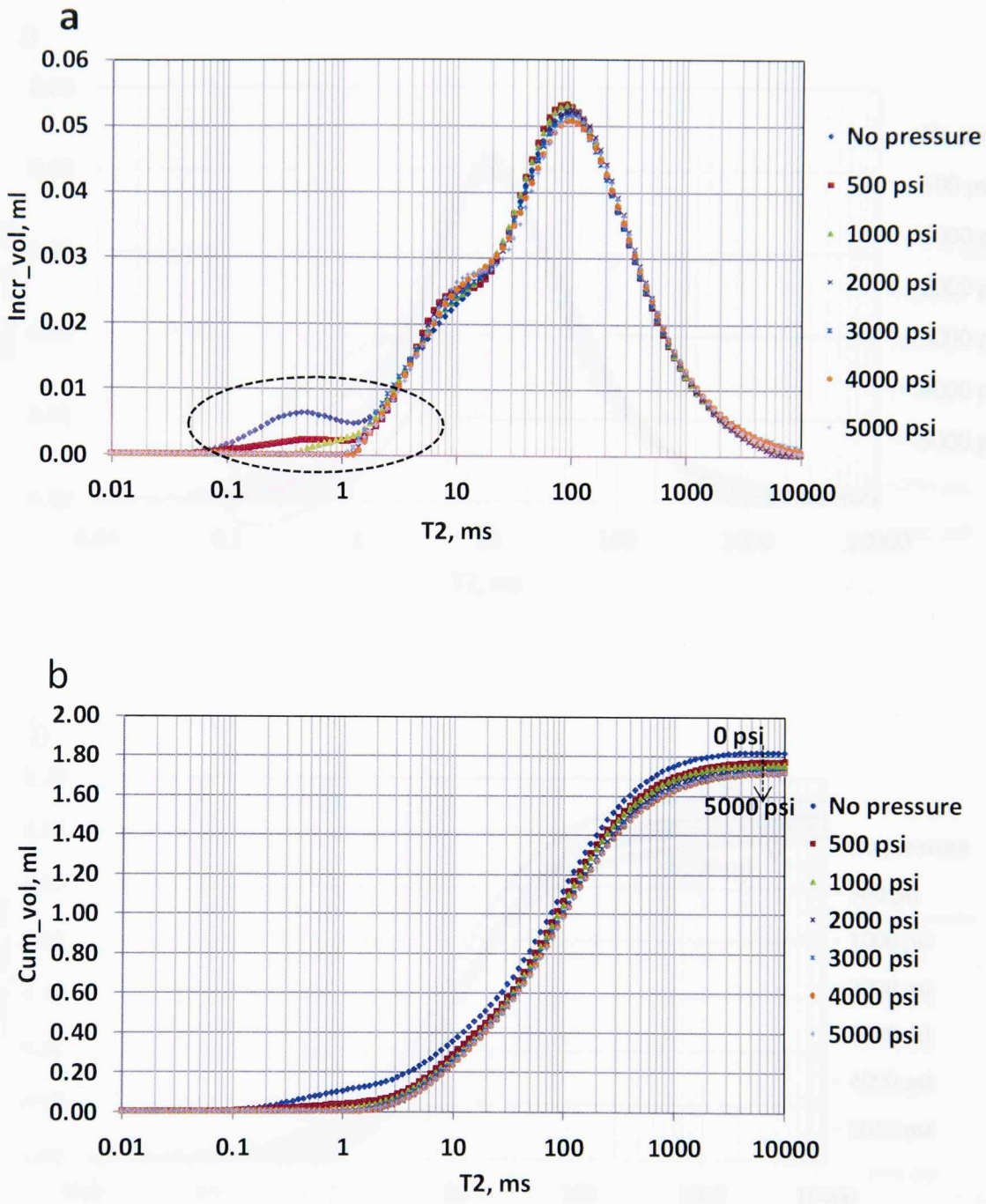

Fig 4.6: a) T_2 relaxation spectra showing NMR incremental volume change as a function of confining pressure. B) NMR cumulative volume change as a function of confining pressure for the Indiana limestone. Note the decrease in pore volume at small T_2 relaxation times (< 3 ms) and the decrease of the cumulative NMR pore volume as function of increasing confining pressure.

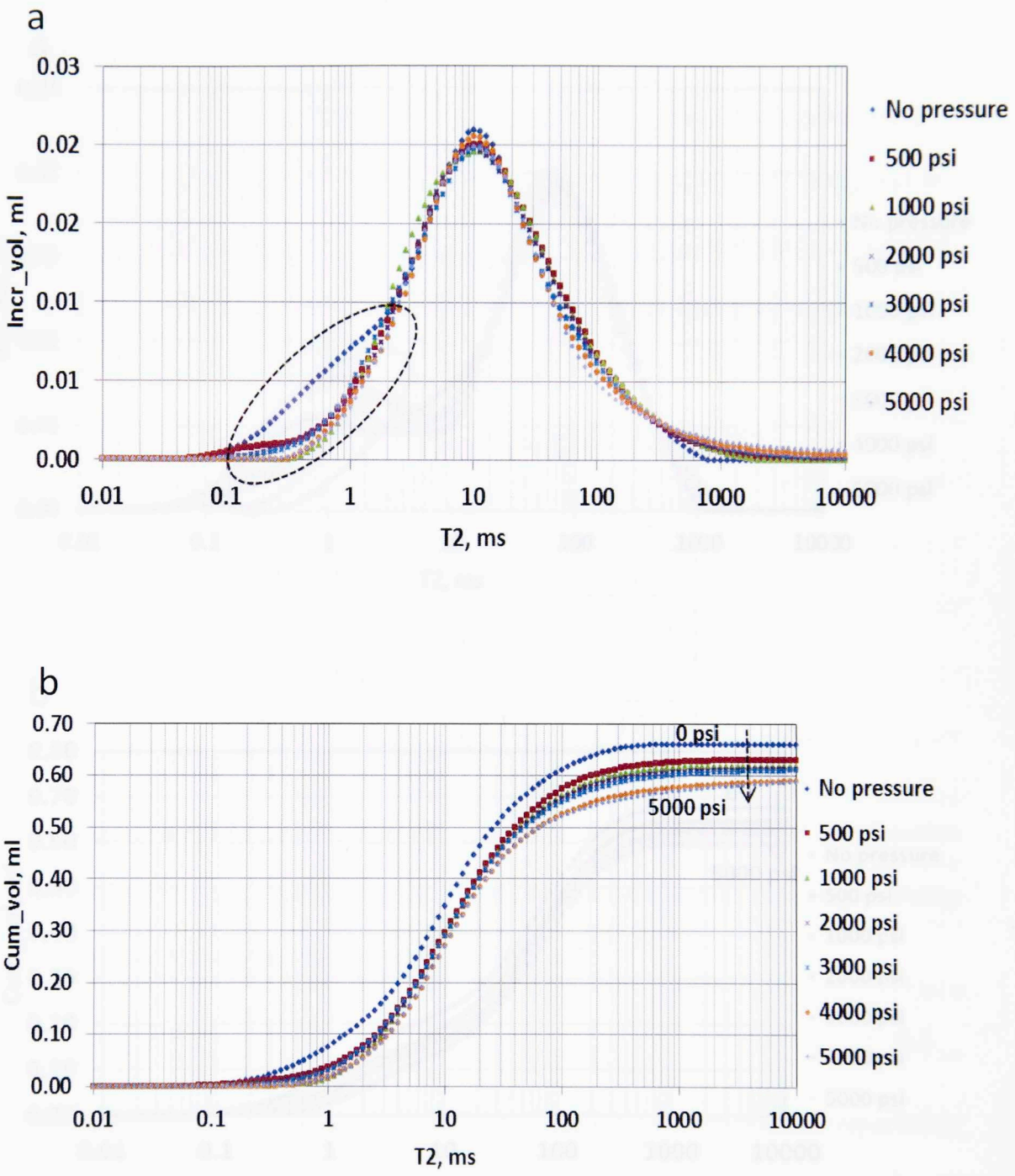

Fig 4.7: a) T_2 relaxation spectra showing NMR incremental volume change as a function of function of confining pressure. B) NMR cumulative volume change as a function of confining pressure for the Tennessee ss sample. Note the decrease in pore volume at small T_2 (< 3ms) relaxation times and the decrease of the cumulative NMR pore volume as function of increasing confining pressure.

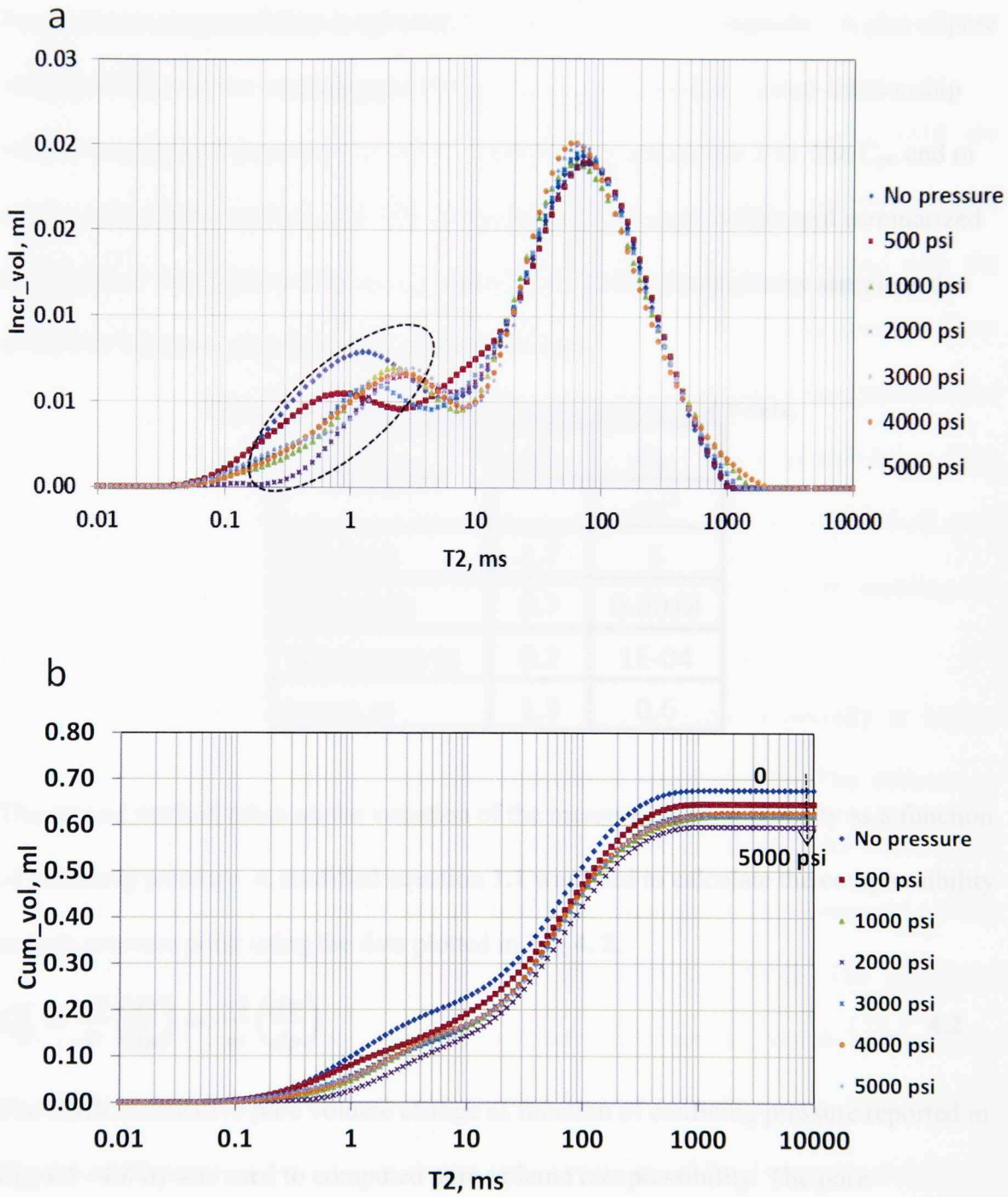

Fig 4.8: a) T_2 relaxation spectra showing NMR incremental volume change as a function of confining pressure. B) NMR cumulative volume change as a function of confining pressure for the Lyons ss sample. Note the decrease in pore volume at small T2 relaxation times(<10 ms) and the decrease of the cumulative NMR pore volume as function of increasing confining pressure.

4.3: Compressibility Measurements Using Different Methods

Pore volume compressibility is calculated using three different methods. A plot of pore compressibility versus confining pressure in log-log space yields a linear relationship whose intercept and slope are C_{po} and m, respectively (see section 2.5). The C_{po} and m values were determined from the MICP data acquired for each sample and summarized in **Table 4.2**. The highest value of C_{po} observed for the Berea sandstone sample is due to the low intrusion pressure in the sample (~20 psi).

Table 4.2: Summary of m and C_{po} derived from MICP data.

Samples	m	C_{po}
	-	psi^{-1}
Berea ss	1.7	5
Indiana ls	0.7	0.0018
Tennessee ss	0.2	1E-04
Lyons ss	1.3	0.6

The second method relies on the variation of the measured helium porosity as a function of confining pressure. A modified equation **1.1** was used to calculate the compressibility at each pressure point using the data plotted in **Fig 4. 2**.

$$C_p^C = \frac{-1}{V}\left(\frac{dv}{dp}\right) = \frac{-1}{\varphi}\left(\frac{d\varphi}{dp}\right) \qquad 4.2$$

The NMR cumulative pore volume change as function of confining pressure reported in **Fig 4.5 –4.8 b)** was used to computed pore volume compressibility. The pore compressibility was calculated using the following formula:

$$C_p^C = \frac{-1}{v_{NMR}}\frac{dv_{NMR}}{dP} \qquad 4.3$$

Where the v_{NMR} is the cumulative NMR pore volume fluid release at each pressure step shown in **Fig 4.5 –8 b)**.

The results of the calculated compressibilities using MICP, AP608, and NMR are reported in **Fig 4.9**. The NMR measurements for Berea, Indiana and Tennessee samples were repeated three times, in order to determine the uncertainty associated with the NMR technique. As presented in **Fig 4.9,** the error in measurement is greater at low pressure and reduces with increasing pressure. The NMR measured compressibilities were also consistently lower than the helium or the MICP compressibilities. One possible explanation for this observation is related to the type and viscosity of fluid used in each the experiment; helium has a smaller diameter than water molecule, enabling the helium to gain more access to the smaller pores.

The MICP, AP608 and NMR compressibilities tend to agree, especially at higher pressure where the error between the measurements is less than 30%. The differences observed at low pressure are mostly related to the presence of microcracks which close at higher pressure. These observations are similar to those made by Greenwald (1980) and Zimmerman (1990) for sandstones (see **Fig 4.10** and **4.11**). The measured compressibility for the Berea sandstone and Indiana limestone, which have similar porosities to the samples used by Zimmerman (initial porosity ranges from 16.5 to 25%), tend to agree. However, the greater compressibility of the Tennessee and Lyons sample compared to the Berea and Indiana samples suggest a higher concentration of microcracks in those samples.

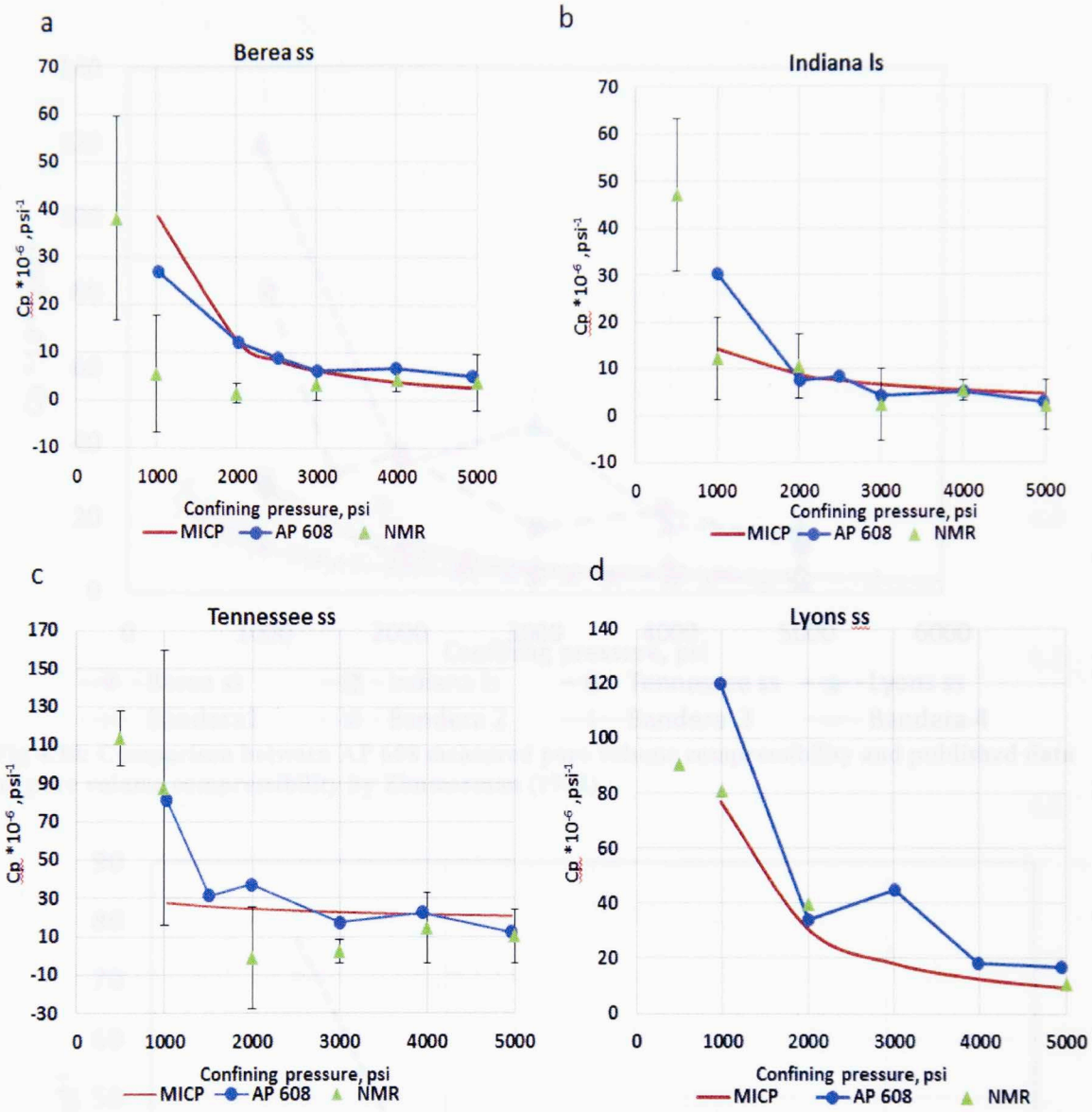

Fig 4.9 : Comparison of compressibility measurements using various method for a) Berea ss, b) Indiana ls c) Tennessee ss and d) Lyons ss. The estimated pore volume compressibilities tend to agree, especially at higher confining pressures. The error in the measurement is less than 30% at high pressure. Note the y-axis scales are different.

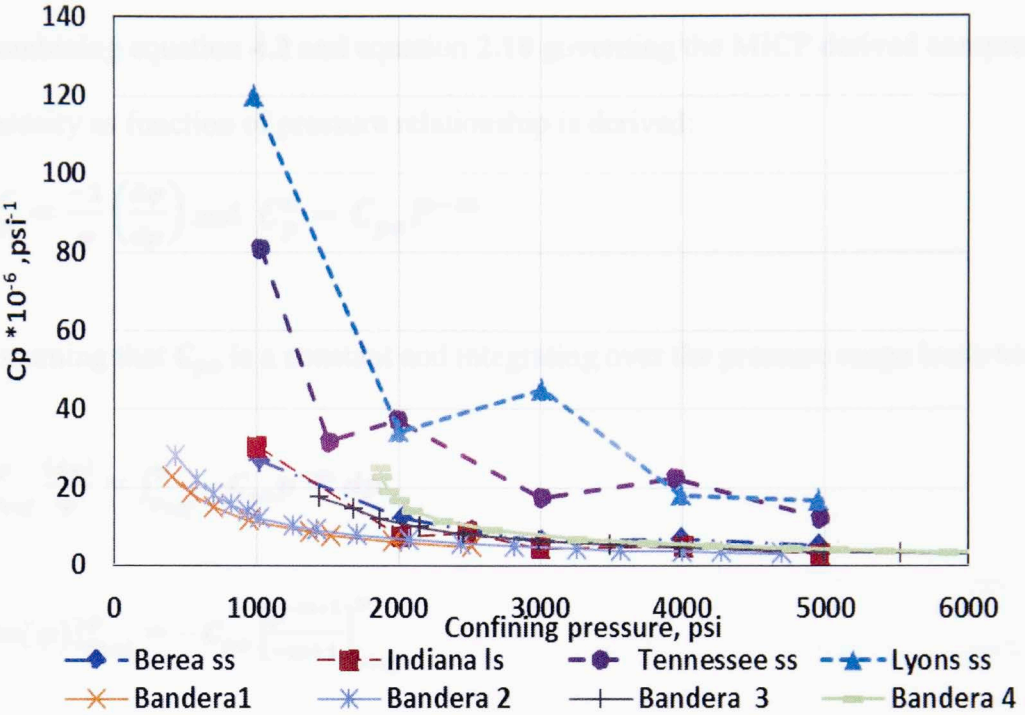

Fig 4.10: Comparison between AP 608 measured pore volume compressibility and published data on pore volume compressibility by Zimmerman (1984).

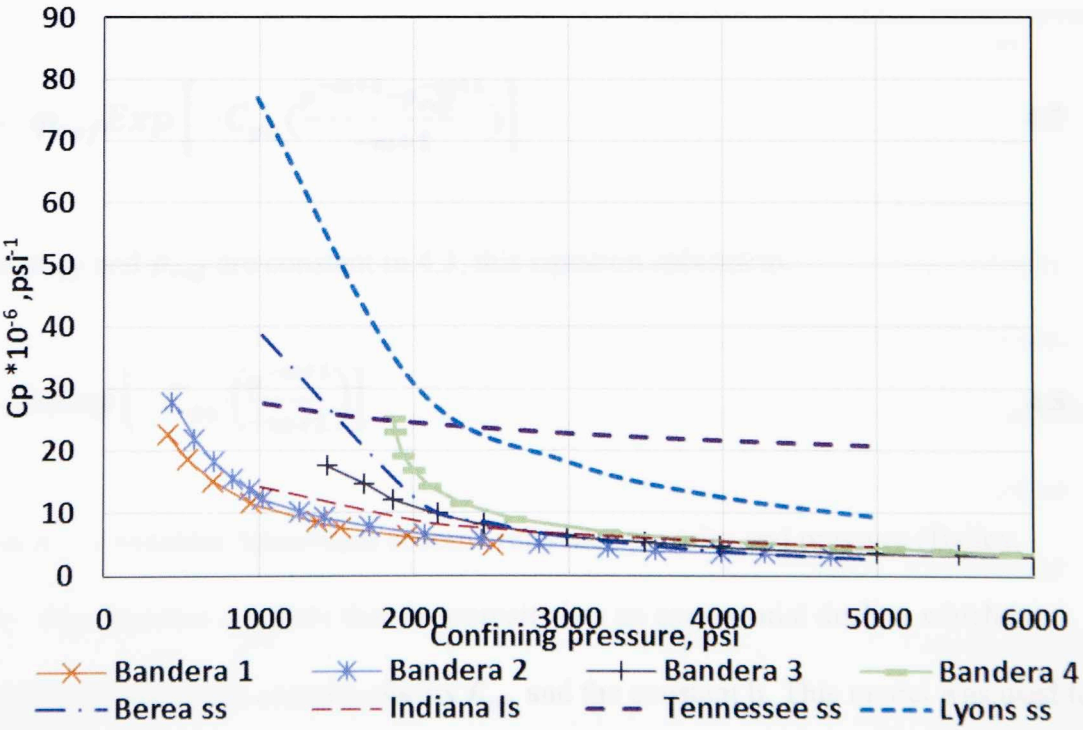

Fig 4.11: Comparison between MICP derived compressibility and published data on pore volume compressibility by Zimmerman (1984).

4.4: Porosity as Function of Pressure Relationship

Combining equation **4.2** and equation **2.10** governing the MICP derived compressibility porosity as function of pressure relationship is derived:

$$C_p^C = \frac{-1}{\varphi}\left(\frac{d\varphi}{dp}\right) \text{ and } C_p^c = C_{po}P^{-m}$$

Assuming that C_{po} is a constant and integrating over the pressure range leads to:

$$\int_{\varphi_{ref}}^{\varphi} \frac{(d\varphi)}{\varphi} = \int_{p_{ref}}^{p} -C_{po}p^{-m}\,dp \qquad \textbf{4.4}$$

$$[ln(\varphi)]_{\varphi_{ref}}^{\varphi} = -C_{po}\left[\frac{p^{-m+1}}{-m+1}\right]_{p_{ref}}^{p} \qquad \textbf{4.5}$$

$$ln\left(\frac{\varphi}{\varphi_{ref}}\right) = -C_{po}\left(\frac{p^{-m+1}-p_{ref}^{-m+1}}{-m+1}\right) \qquad \textbf{4.6}$$

$$\varphi = \varphi_{ref}Exp\left[-C_{po}\left(\frac{p^{-m+1}-p_{ref}^{-m+1}}{-m+1}\right)\right] \qquad \textbf{4.7}$$

Since φ_{ref} and p_{ref} are constant in 4.3, this equation reduces to:

$$\varphi = bExp\left[-C_{po}\left(\frac{p^{-m+1}}{-m+1}\right)\right] \qquad \textbf{4.8}$$

Where b is a constant determined at some reference porosity and pressure (Bailey, 2009). This equation suggests that the porosity has an exponential decline which is controlled by the initial compressibility C_{po} and the constant b. This model was used to calculate the porosity as function of pressure from the MICP data shown in **Table 4.2.** The predicted porosity from MICP is compared to the helium measured porosity and the

results are sown in **Fig 4.12**. The error between the measured AP 608 and the derived MICP porosities was less than 3%. The φ_{ref} and p_{ref} were determined from helium at 1,000 psi.

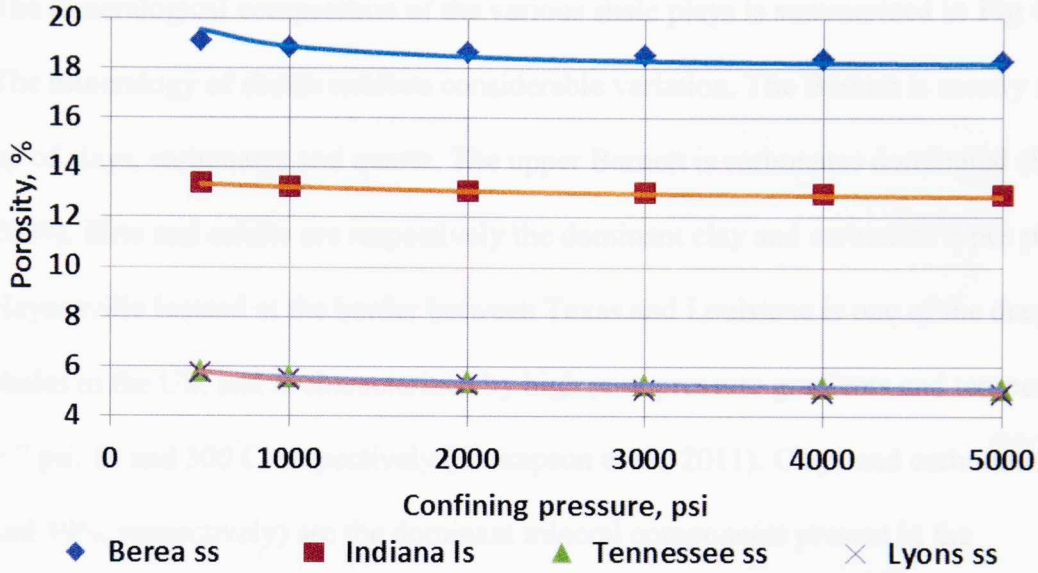

Fig 4.12: Comparison between AP 608 measured porosity and that predicted from MICP measurements. The AP 608 porosity is shown with the different symbols and the MICP derived porosity is shown as solid line. The MICP derived porosity as function of confining pressure agrees well with the measured AP 608 porosity dependence. The error between the two measures of porosity was less than 3 %.

4.5: Shales Description

Routine petrophysical measurements on over 175 organic rich shales of total porosity, mineralogy, TOC, MICP and NMR measurements were acquired. The measurements were made on samples from the following formations: Barnett, Eagle Ford, Haynesville, Wolfcamp, Woodford, and an Ordovician shale. The Barnett, Haynesville, Woodford and Ordovician shale samples are located in the gas generating window; whereas, the Eagle Ford and the Wolfcamp are located on the oil generating window. Eleven samples from Eagle Ford and Wolfcamp shales were selected for the NMR compressibility

measurements. The NMR pore volume compressibility measurements are compared to the MICP derived compressibility.

4.5.1: Mineralogy Description

The mineralogical composition of the various shale plays is summarized in **Fig 4.13**. The mineralogy of shales exhibits considerable variation. The Barnett is mostly made up of clays, carbonates and quartz. The upper Barnett is carbonates dominated (Sagar, 2009). Illite and calcite are respectively the dominant clay and carbonate types present. Haynesville located at the border between Texas and Louisiana is one of the deepest shales in the US, and is characterized by high pore pressure gradients and temperatures, 0.7 psi/ ft. and 300°C, respectively (Thompson et al., 2011). Clays and carbonates (44% and 39%, respectively) are the dominant mineral components present in the Haynesville. Illite and mixed layered clays are the dominant clay types. Calcite and siderite are the dominant carbonates (Asgarov, 2013). The Woodford shale, located in Oklahoma, is mainly composed of clays and quartz (47% and 28%, respectively) (Gupta, 2012). The quartz originated from biogenic silica which formed after the precipitation of radiolarian and sponge spicules (Cardott, 2013). The Wolfcamp shale, located in the Permian basin, has been identified as the source rock for the Midland and Delaware Basin. The Wolfcamp is primarily composed of clays and quartz (41% and 31%, respectively). The dominant types of clay are illite and mixed layer (Calderon, 2013). The Eagle Ford shale, located in Texas, is considered as a source rock for the Austin Chalk and the East Texas fields (Sondhi, 2011). The Eagle Ford is mainly composed of carbonates and traces of clays (80% and 12%, respectively). The dominant type of carbonate mineral present is calcite. The Ordovician shale is mostly clays and

carbonates (52% and 29 %, respectively). Calcite is the dominant carbonate type and illite and mixed layer clays are the dominant clay minerals throughout all the shales studied.

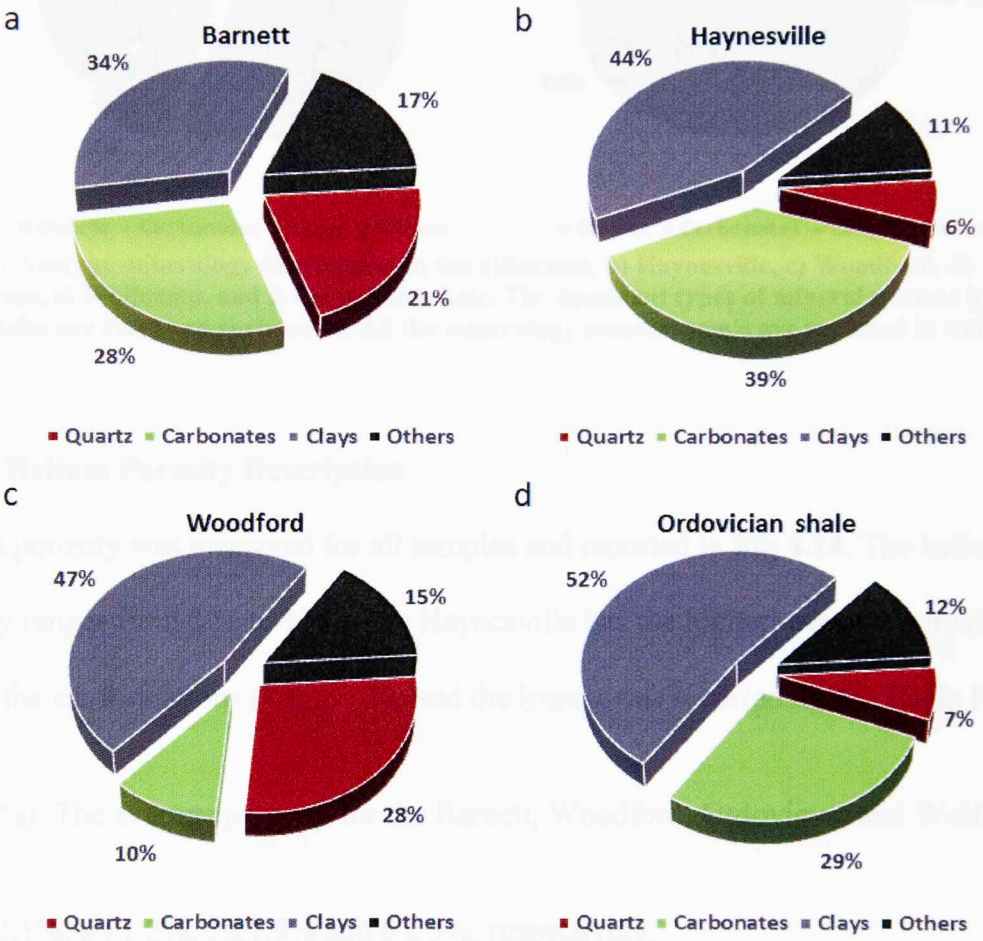

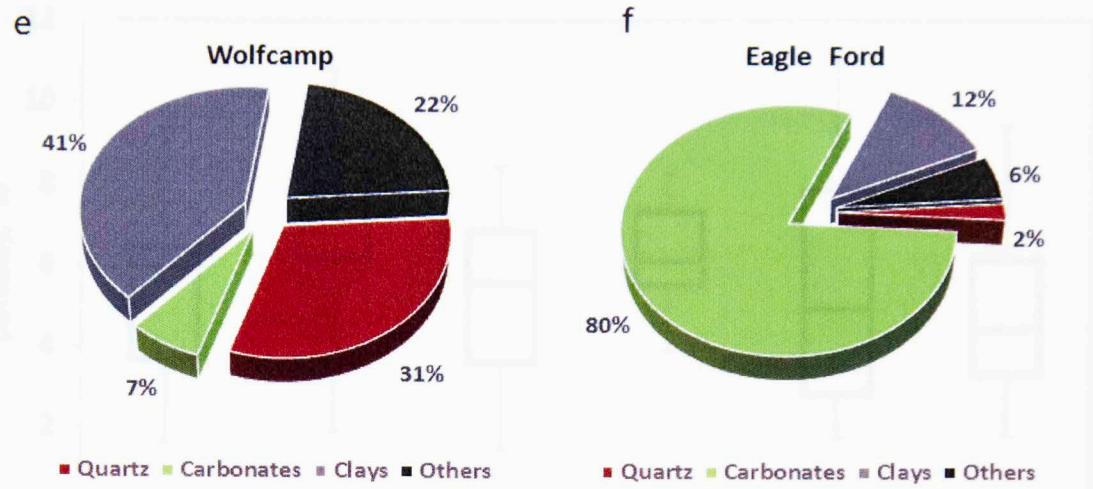

Fig 4.13: Average mineralogy distribution in the a)Barnett, b) Haynesville, c) Woodford, d) Ordovician, e) Wolfcamp, and f) Eagle Ford shale. The dominant types of mineral present in most of the shales are clays and carbonates. All the mineralogy measurements are reported in weight percent.

4.5.2: Helium Porosity Description

Helium porosity was measured for all samples and reported in **Fig 4.14.** The helium porosity ranges from 2 % to 12% .The Haynesville has the highest average porosity among the six formations (7 $\pm$ 2.1 %) and the lowest was reported for the Eagle Ford ($5\pm1.8\%$). The average porosity for the Barnett, Woodford, Ordovician and Wolfcamp are $5\pm2.1\%$, $6\pm1.2\%$, $5\pm1.9\%$ and $6\pm 3\%$, respectively.

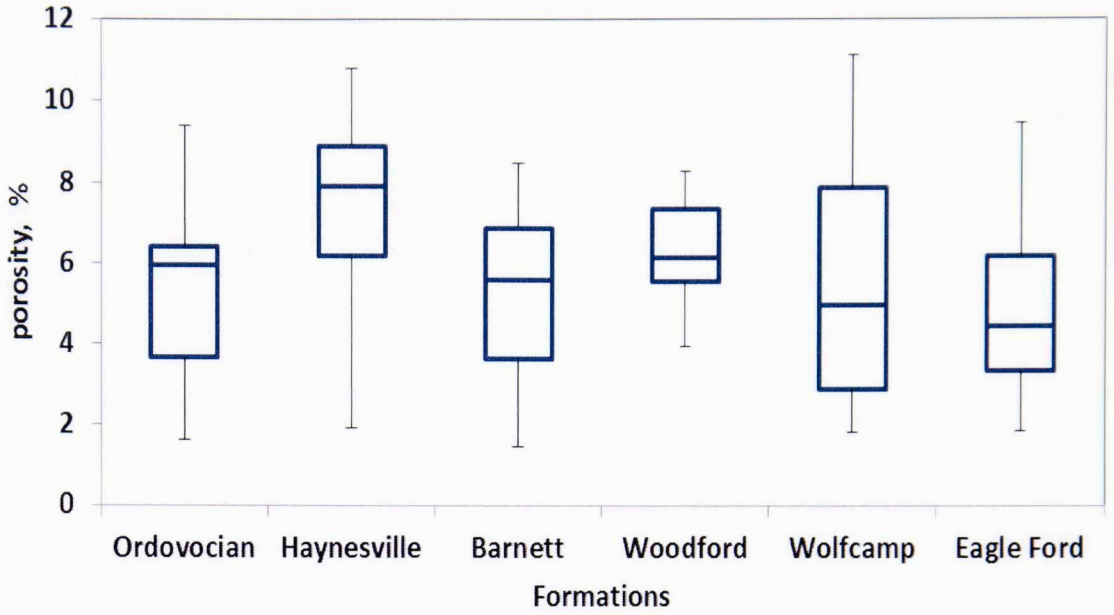

Fig 4.14: Total porosity distribution for the different samples. The highest average porosity was reported for the Haynesville and the lowest was reported for the Eagle Ford formation.

4.5.3: TOC and Thermal Maturity Description

The reported TOC value ranges from 0.2% to 9% by weight as displayed in **Fig 4.15**. The Woodford shale has the highest average TOC value among the six formations (6 ± 2.3 %) and the lowest was reported for the Ordovician shale (1 ±0.75%). The average TOC for the Barnett, Haynesville, Wolfcamp and Eagle Ford are 3 ±2.3%, 3±2.3%, 2.3±1%, and 5± 1.9% , respectively.

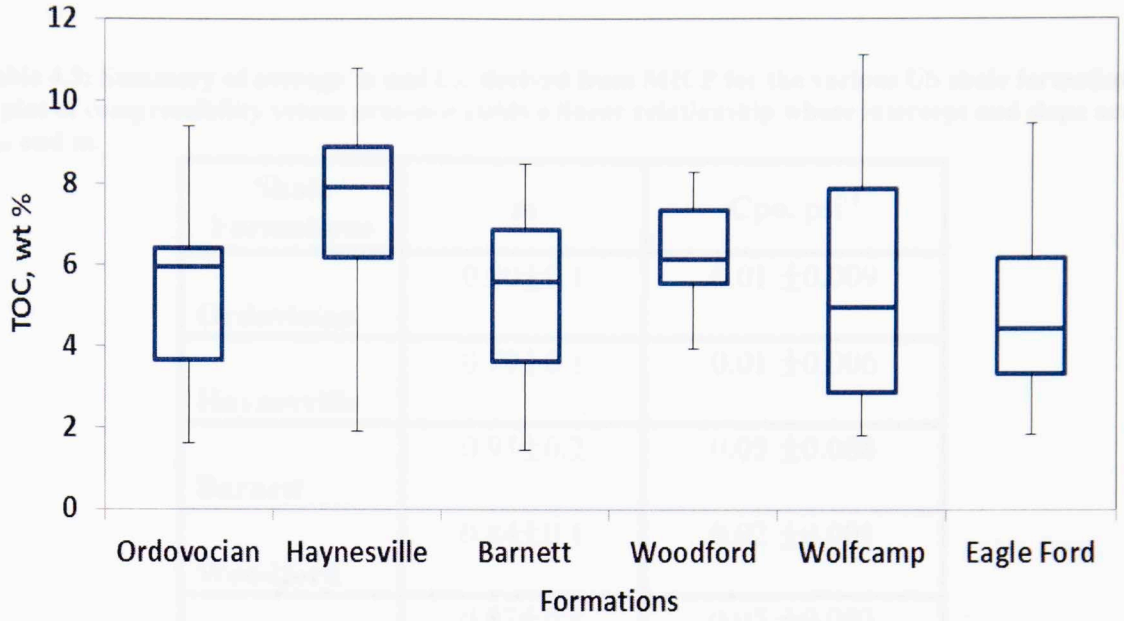

1Fig 4.15: TOC distribution for the different shale samples. The Woodford with an average of 5.6 % has the highest TOC value. While, the lowest value of TOC was recorded for the Ordovician shale (0.9 %). All the data are reported in weight percent.

4.6: MICP Compressibility

Shales have a high intrusion pressure which means compressibility before intrusion may be important. Bailey's pore volume compressibility was derived from MICP data for several shales. The average C_{po} and m values were determined for several shales and summarized in **Table 4.3.**

Table 4.3: Summary of average m and C_{po} derived from MICP for the various US shale formations. A plot of compressibility versus pressure yields a linear relationship whose intercept and slope are C_{po} and m.

Shale Formations	m	Cpo, psi^{-1}
Ordovician	0.80±0.1	0.01 ±0.009
Haynesville	0.79±0.1	0.01 ±0.006
Barnett	0.95±0.2	0.05 ±0.008
Woodford	0.84±0.1	0.02 ±0.001
Wolfcamp	0.87±0.2	0.05 ±0.003
Eagle Ford	0.82± 0.1	0.02 ±0.001

The MICP compressibilities distribution at each confining pressure for the different shale formations are shown in the **Appendix C.** The Barnett, Wolfcamp, and Eagle Ford samples have the highest average MICP compressibilities among the six shale formations.

4.7: NMR Pore Volume Changes as Function of Pressures

Eleven samples from the previously mentioned shale formations were selected for NMR pore compressibility measurements. All samples except the Haynesville (11778) were located in the oil window. These shale samples were selected based on their petrophysical properties which are described in **Table 4.4**. For instance, the TOC values range from 0.8% to 6.4% and clay content varies from 5% to 43% by weight.

The T_2 relaxation spectra as a function of confining pressure are summarized below for six samples (**Fig 4.16- 4.21 a)**. Additional samples are shown in **Appendix B**. The

initial NMR T_2 spectra for the shale samples after dodecane pressure saturation (7,000 psi) showed a bimodal distribution with a first peak occurring around 0.1-0.6 ms and the second around 5-10 ms. The first peak is associated with inorganic pores and the second peak with organic and inorganic pores. Those observations are similar to those made by Odusina (2011) and Tinni (2013).

The shale samples also displayed a decrease in NMR peaks as function of confining pressure. The decrease appears to be mainly in the first peak, while the second peak hardly changes. These two independent observations suggest that the sample is being compressed. As the confining pressure is increased, the fluid present in the pore space is expelled causing a decrease in the peak amplitude.

Table 4.4: Summary of petrophysical properties for 11 shale samples selected for NMR pore volume compressibility measurement.

Sample	Formation	Porosity, %	TOC, wt%	Quartz, wt %	Carbonates, wt %	Clays, wt %	C_{po}, psi^{-1}	m
8097	Wolfcamp	4.2	1.1	45	25	11	0.01	1.1
8123	Wolfcamp	1.8	2.5	42	15	38	0.31	1.25
816.6	Wolfcamp	2.0	3.6	38	16	34	0.2	1.13
8154	Wolfcamp	4.2	2.6	35	1	43	0.32	1.3
8195	Wolfcamp	7.6	1.5	30	5	40	0.0085	0.8
8356	Wolfcamp	7.9	0.8	37	2	31	0.006	0.78
12595	Eagle Ford	8.8	6.1	1	84	9	0.04	1.1
12597	Eagle Ford	2.0	0.9	0	92	5	0.013	0.8
12603	Eagle Ford	8.8	6.2	1	85	8	0.005	0.76
12710	Eagle Ford	6.6	6.4	9	52	37	0.0055	0.75
11779	Haynesville	5.5	2.5	2	44	43	0.008	0.75

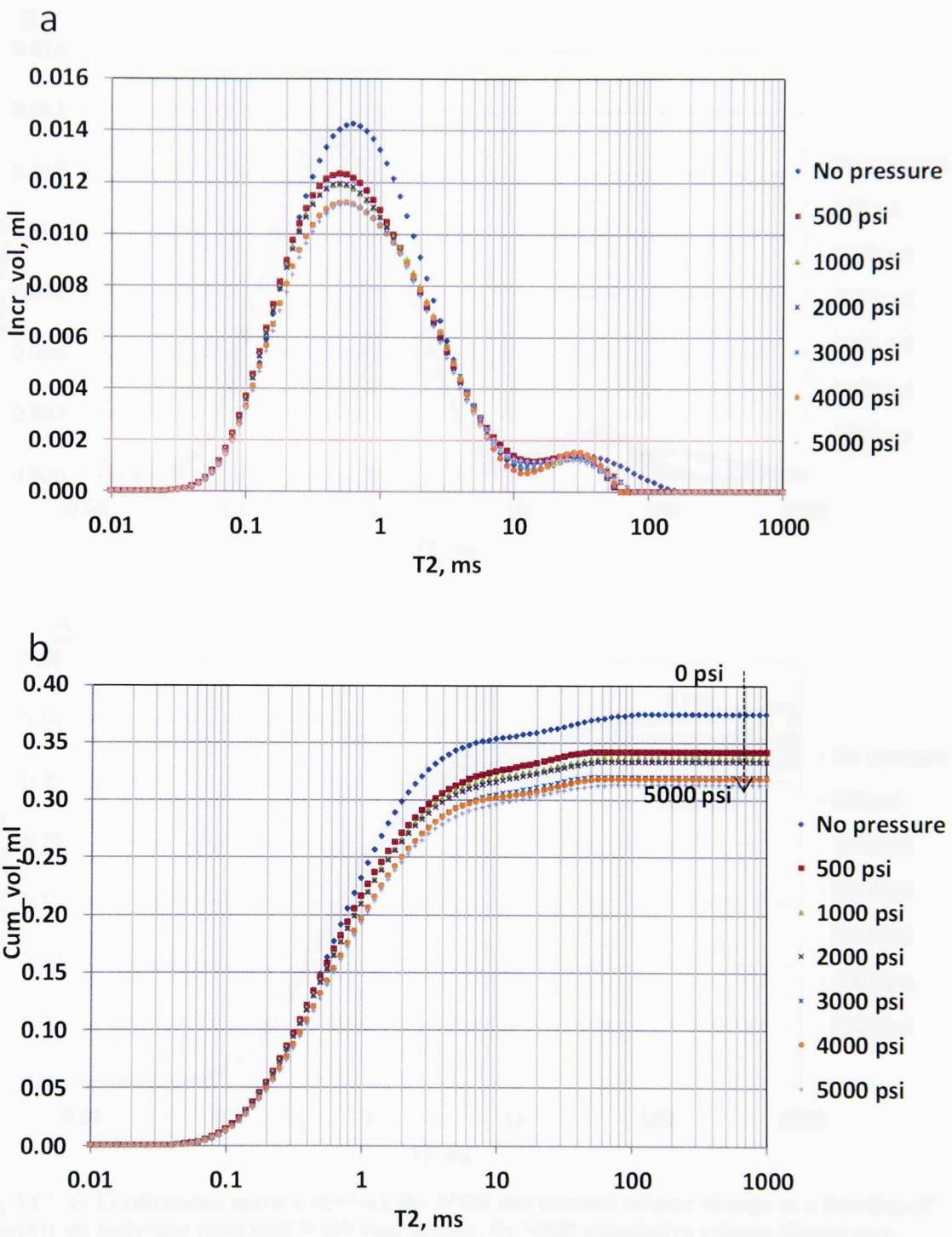

Fig 4.16: a) T_2 relaxation spectra showing the NMR incremental volume change as a function of pressure on dodecane saturated Wolfcamp sample. b) NMR cumulative volume change as a function of function of pressure for the Wolfcamp 8123. Note the decrease in pore volume at small T_2 relaxation time and the decrease of the cumulative NMR pore volume as function of increasing pressure.

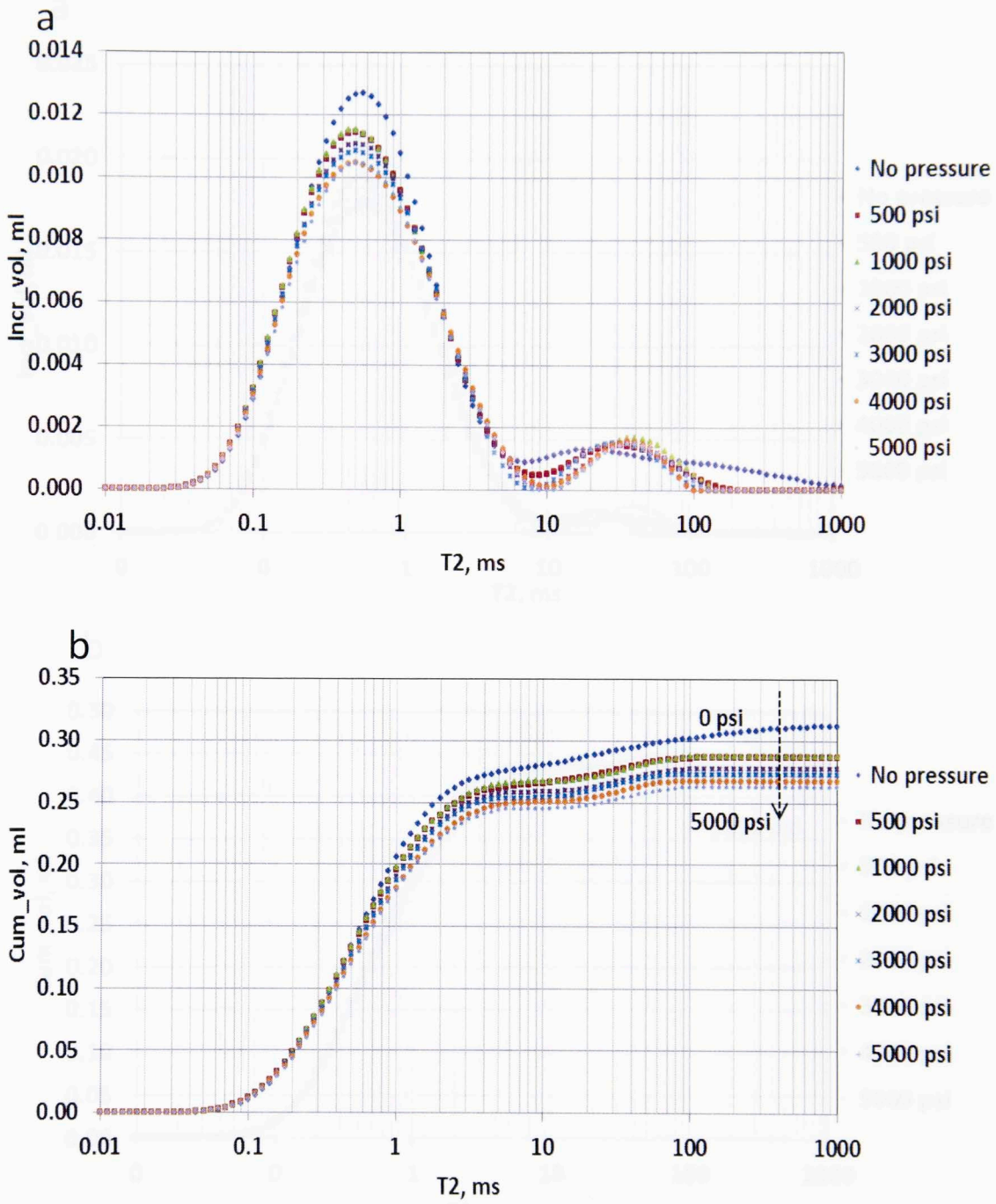

Fig 4.17: a) T_2 relaxation spectra showing the NMR incremental volume change as a function of pressure on dodecane saturated Wolfcamp sample. B) NMR cumulative volume change as a function of function of pressure for the Wolfcamp 8126.6. Note the decrease in pore volume at small T2 relaxation time and the decrease of the cumulative NMR pore volume as function of increasing pressure.

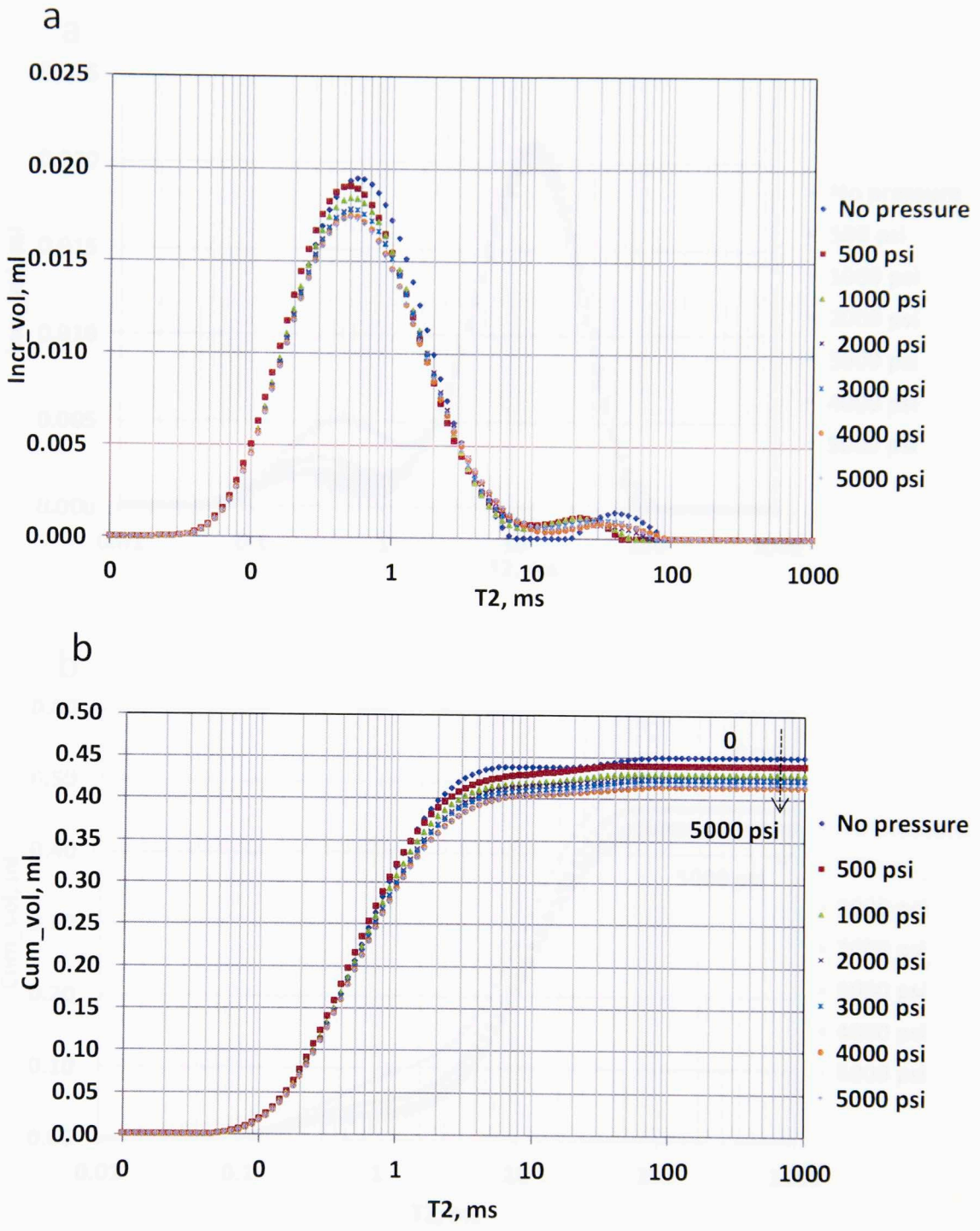

Fig 4.18: a) T_2 relaxation spectra showing the NMR incremental volume change as a function of pressure on dodecane saturated Wolfcamp sample. B) NMR cumulative volume change as a function of function of pressure for the Wolfcamp 8154. Note the decrease in pore volume at small T2 relaxation time and the decrease of the cumulative NMR pore volume as function of increasing pressure.

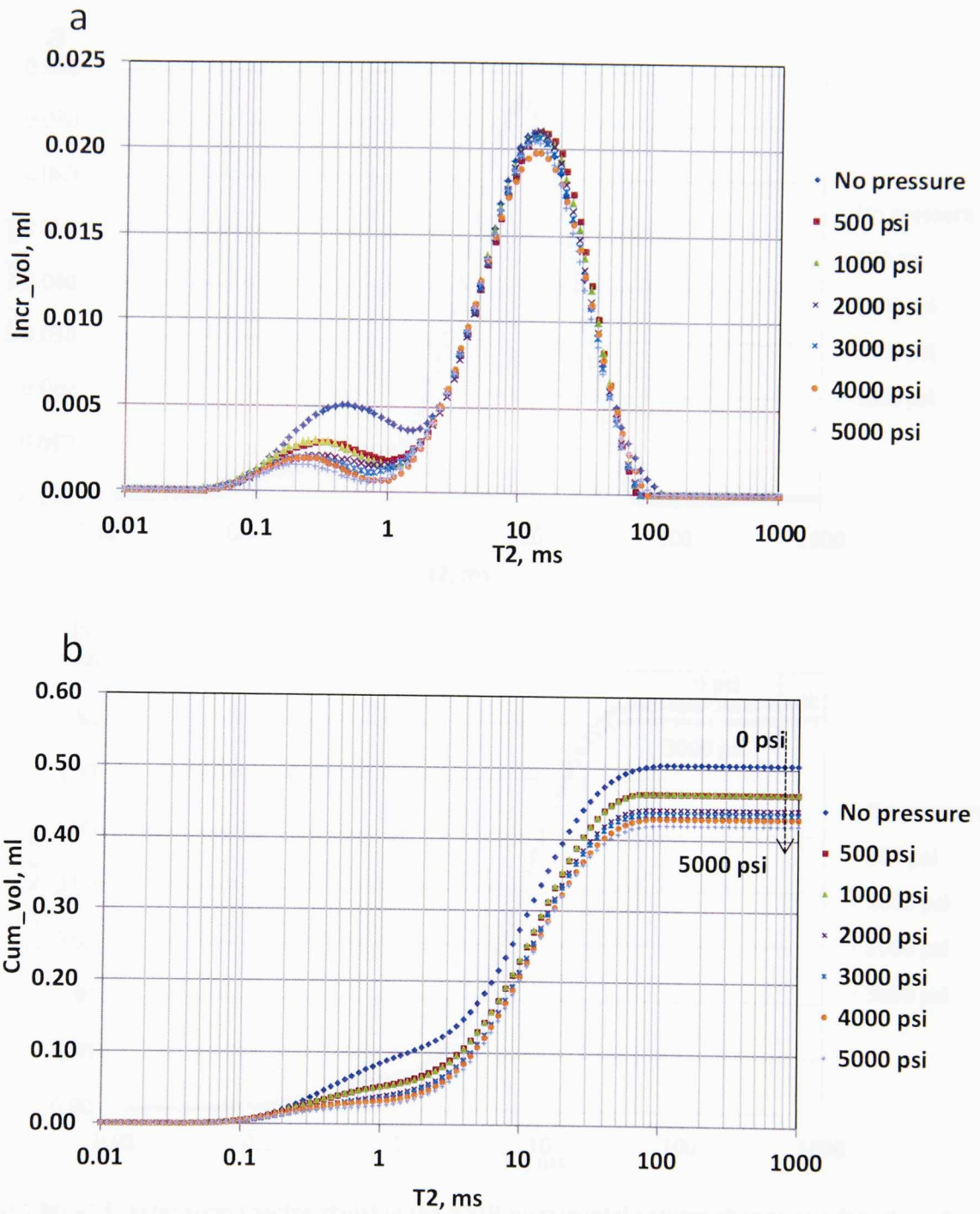

Fig 4.19: a) T_2 relaxation spectra showing the NMR incremental volume change as a function of pressure on dodecane saturated Eagle Ford sample. B) NMR cumulative volume change as a function of function of pressure for the Eagle Ford 12596.6. Note the decrease in pore volume at small T2 relaxation time and the decrease of the cumulative NMR pore volume as function of increasing pressure.

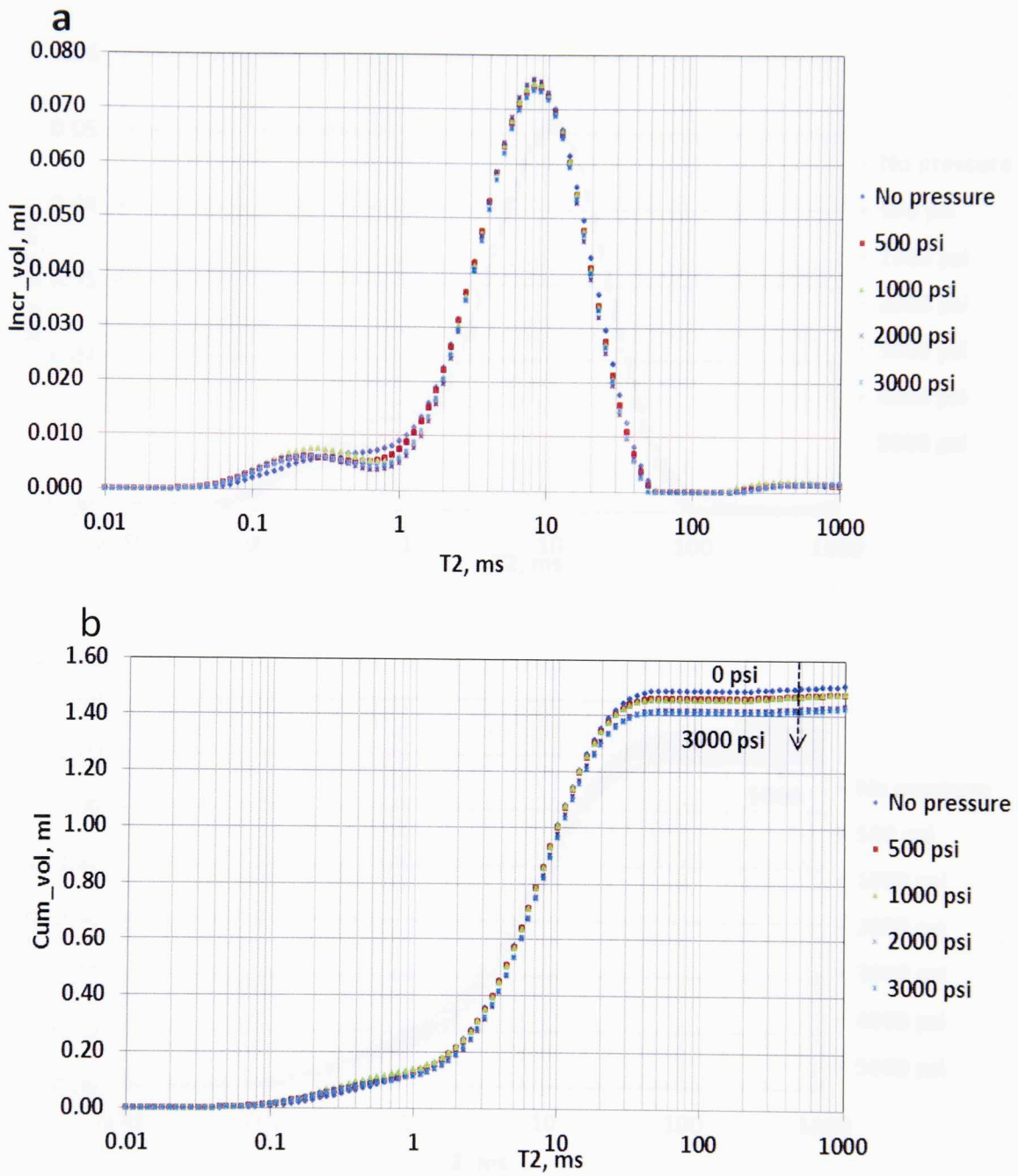

Fig 4.20: a) T_2 relaxation spectra showing the NMR incremental volume change as a function of pressure on dodecane saturated Eagle Ford sample. B) NMR cumulative volume change as a function of function of pressure for the Eagle Ford 12602.35. Note the decrease in pore volume at small T2 relaxation time and the decrease of the cumulative NMR pore volume as function of increasing pressure.

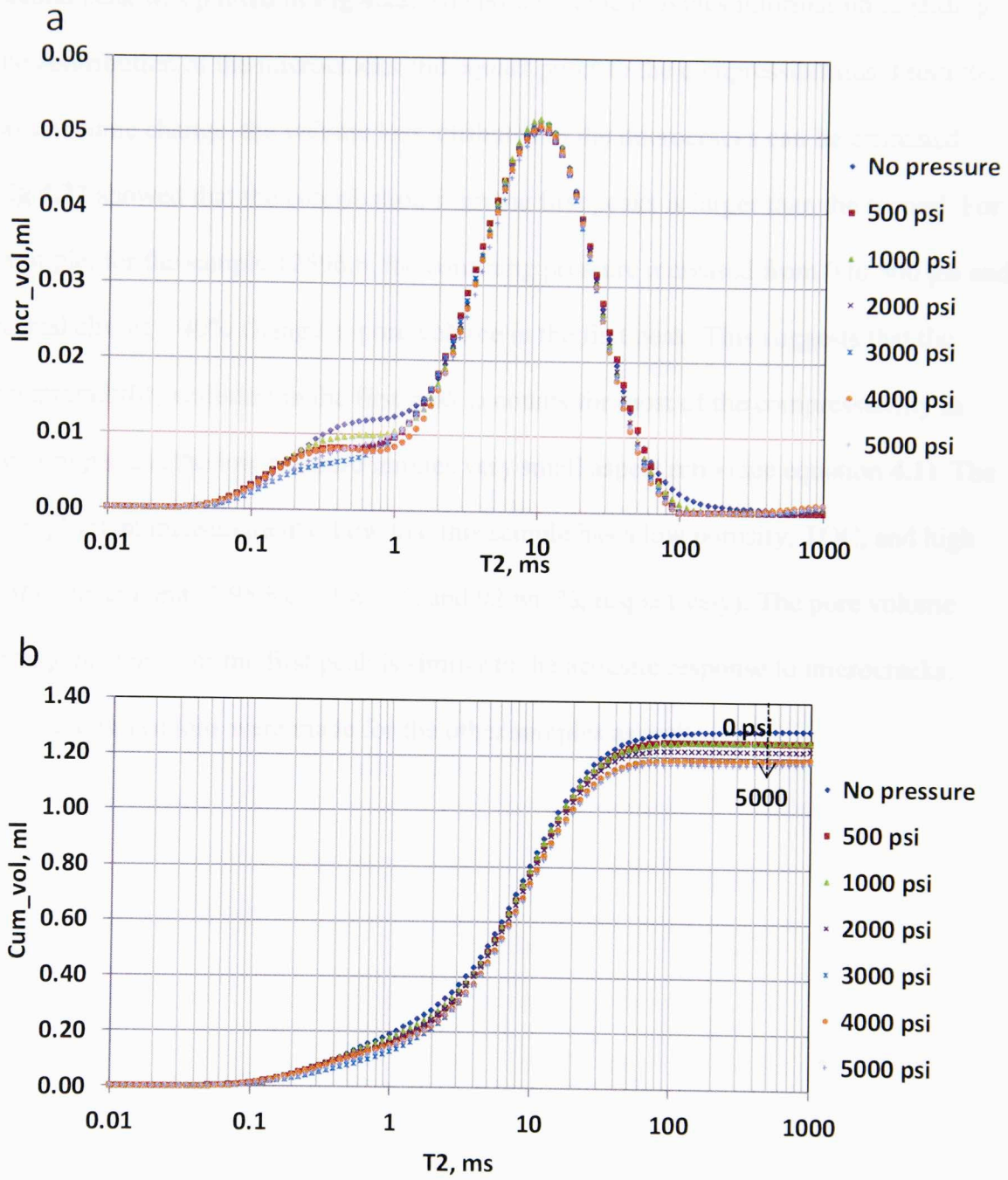

Fig 4.21: a) T_2 relaxation spectra showing the NMR incremental volume change as a function of pressure on dodecane saturated Eagle Ford sample. B) NMR cumulative volume change as a function of pressure for the Eagle Ford f 12709.6. Note the decrease in pore volume at small T2 relaxation time and the decrease of the cumulative NMR pore volume as function of increasing pressure.

The pore volume change is calculated using the difference between the NMR volume at 0 psi and the volume at any given pressure. The pore volume change for the first and

second peak was plotted in **Fig 4.22**. The pore volume provides information regarding the contribution of the microcracks and equant pores to the compressibilities. From the pore volume change, the volume loss attributed to the microcracks can be estimated. **Fig 4.22** showed that the contribution from the first peaks is larger than the second. For example, for the sample 12596.6, the confining pressure increased from 0 to 500 psi and caused almost a 40% change in pore volume in the first peak. This suggests that the compressibility reflected in the first peak accounts for most of the compressibility in this sample and the low pressure implies very small aspect ratio (see equation **4.1**). The petrophysical measurements show that this sample has a low porosity, TOC, and high carbonate content (1.95 %, 0.9 wt. %, and 92 wt. %, respectively). The pore volume change response for the first peak is similar to the acoustic response to microcracks. Similar observations were made for the other samples as well.

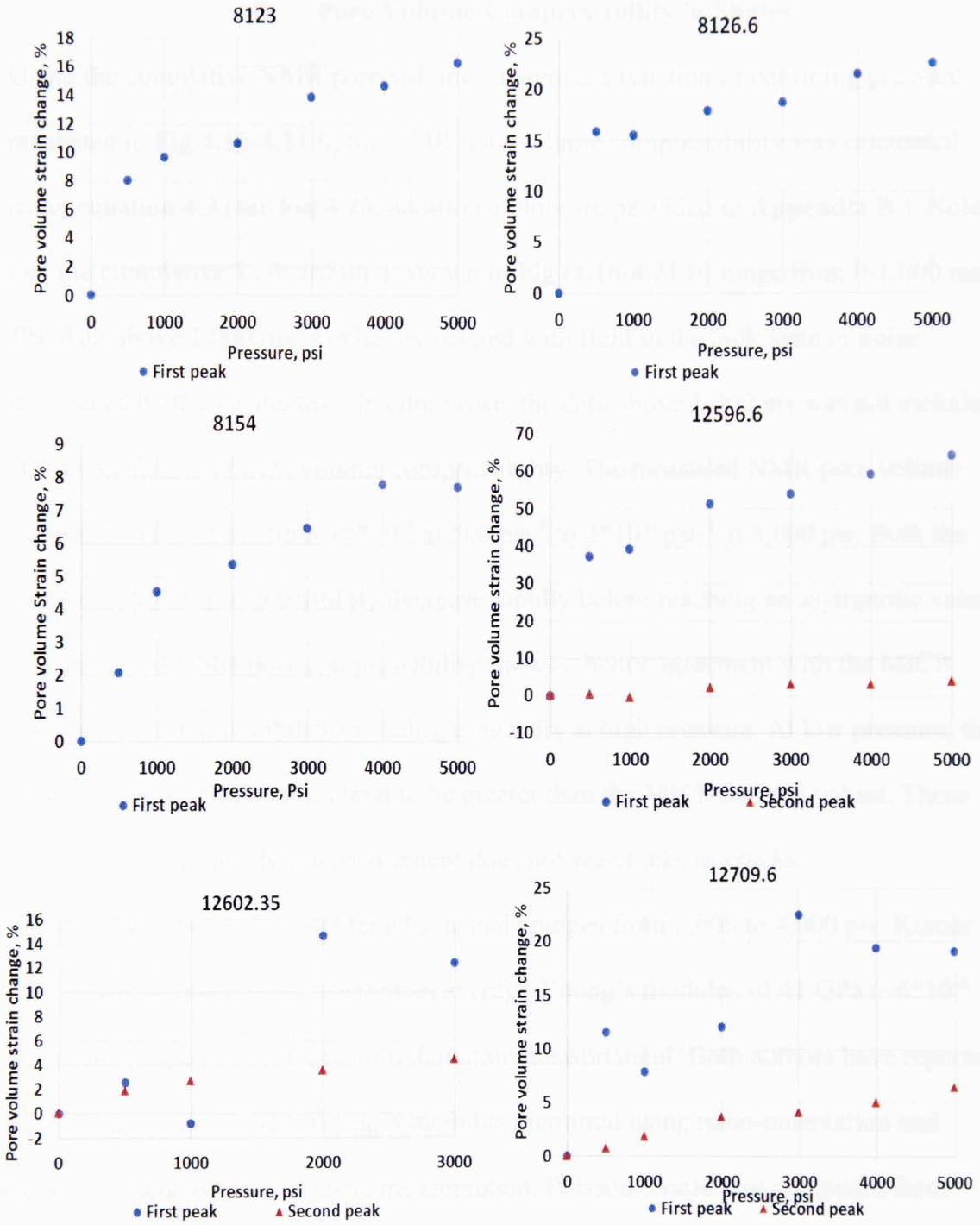

Fig 4.22: Pore volume change as a function of confining pressure for six shale dodecane saturated samples. The pore volume change was estimated from NMR measurements. Pore volume change provides information regarding the relative contributions of microcracks and equant pores to the total compressibility of the sample.

4.8: Pore Volume Compressibility in Shales

Using the cumulative NMR pore volume change as a function of confining pressure presented in **Fig 4.16-4.21 b**, the NMR pore volume compressibility was calculated using equation **4.3** (see **Fig 4.23**, additional plots are provided in **Appendix B**). Note that the cumulative T_2 distribution shown in **Fig (4.16-4.21 b)** range from 0-1,000 ms. The data above 1,000 ms is either associated with fluid in the bulk state or noise introduced by the subtraction. In either case, the data above 1,000 ms was not included in the calculation of pore volume compressibility. The measured NMR pore volume compressibility varies from $18*10^{-5}$ at 500 psi^{-1} to $2*10^{-6}$ psi^{-1} at 5,000 psi. Both the NMR and MICP compressibility decrease rapidly before reaching an asymptotic value. The measured NMR pore compressibility shows a better agreement with the MICP derived pore compressibility in shales, especially at high pressure. At low pressure, the NMR compressibility values tend to be greater than the MICP derived values. These differences suggest MICP measurement does not see cracks as cracks.

The closure pressure for microcracks in shale ranges from 2,000 to 4,000 psi. Kumar (2012) and Shukla (2013) reported an average Young's modulus of 41 GPa (~$6*10^{-6}$ psi) in the Eagle Ford from nano-indentation measurement. Both authors have reported a good correlation for the Young's modulus measured using nano-indentation and dynamic modulus from acoustic measurement. Poisson's ratio was computed from acoustic measurement using the following the equation:

$$\vartheta = \frac{V_p^2 - 2V_s^2}{2(V_p^2 - V_s^2)} \qquad 4.9$$

Where V_p and V_s are, respectively, the compressional and shear wave velocities. The average Poisson's ratio for the Eagle Ford samples was 0.3. The aspect ratio calculated for the shale samples ranged from $3.9*10^{-4}$ and $8*10^{-4}$. The average surface relaxivity for the shale samples was determined from equation **3.8** using both NMR and MICP data. The average surface relaxivity for the Eagle Ford samples was 0.6 μm/sec. The estimated width for microcracks in the Eagle Ford ranged from 0.1 to 10 μm, quite reasonable numbers. These values are consistent with the micro-CT observations of mercury impregnated shale samples (Curtis, 2012)

A comparison between the MICP derived compressibilities and Zimmerman's (1984) pore compressibilities is presented in **Fig 4.24**. This plot suggests that shales have greater compressibilities than sandstones even at higher pressure. This higher compressibility could be explained by the presence of micro fractures (see Fig **4.25**). The average width of fractures in these images was around 60 μm.

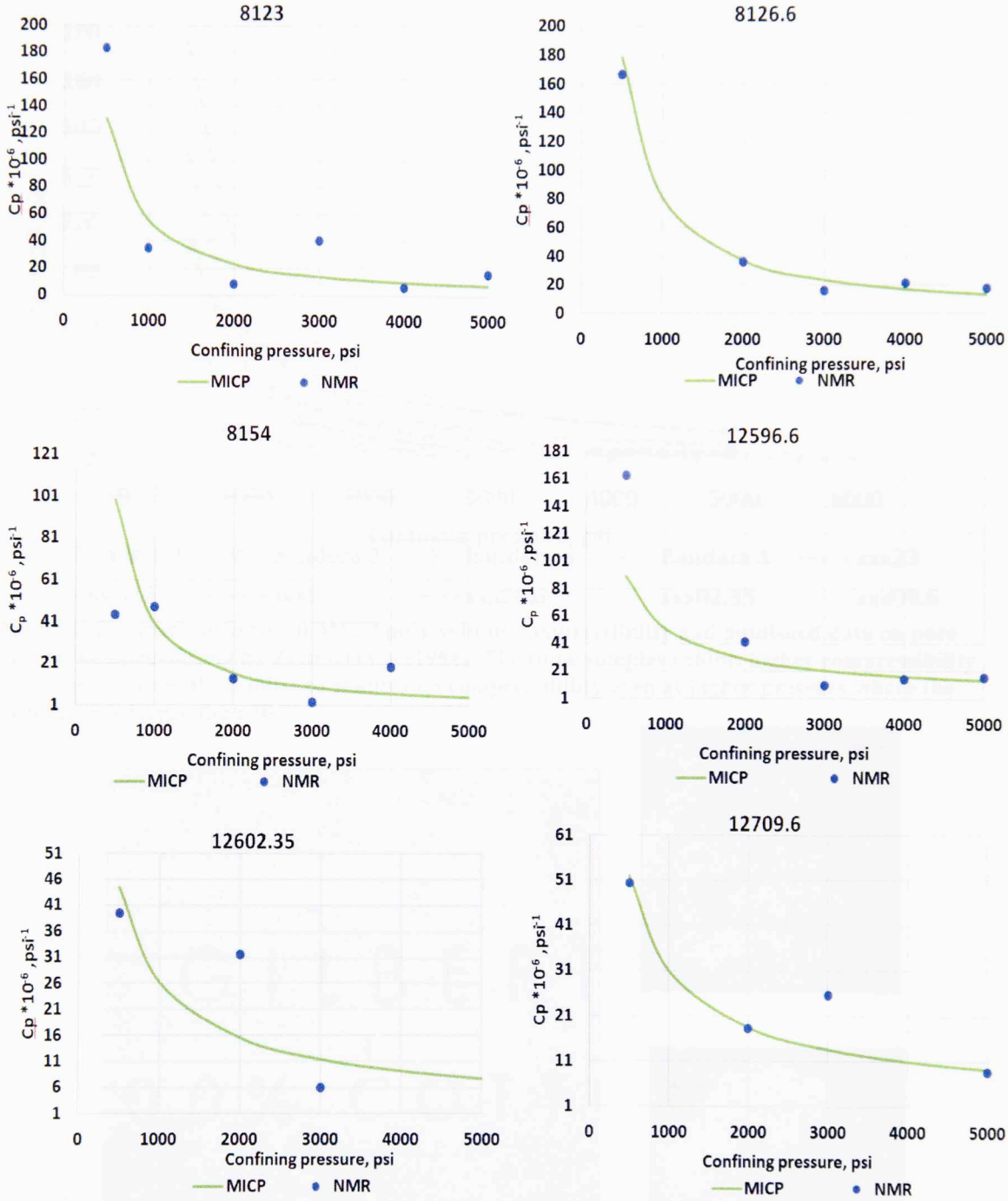

Fig 4.23: Comparison between NMR and compressibilities calculated from MICP measurement for selected shale samples. The measured NMR compressibility tends to agree with MICP derived compressibility. The agreement between the compressibility values is better at higher pressures.

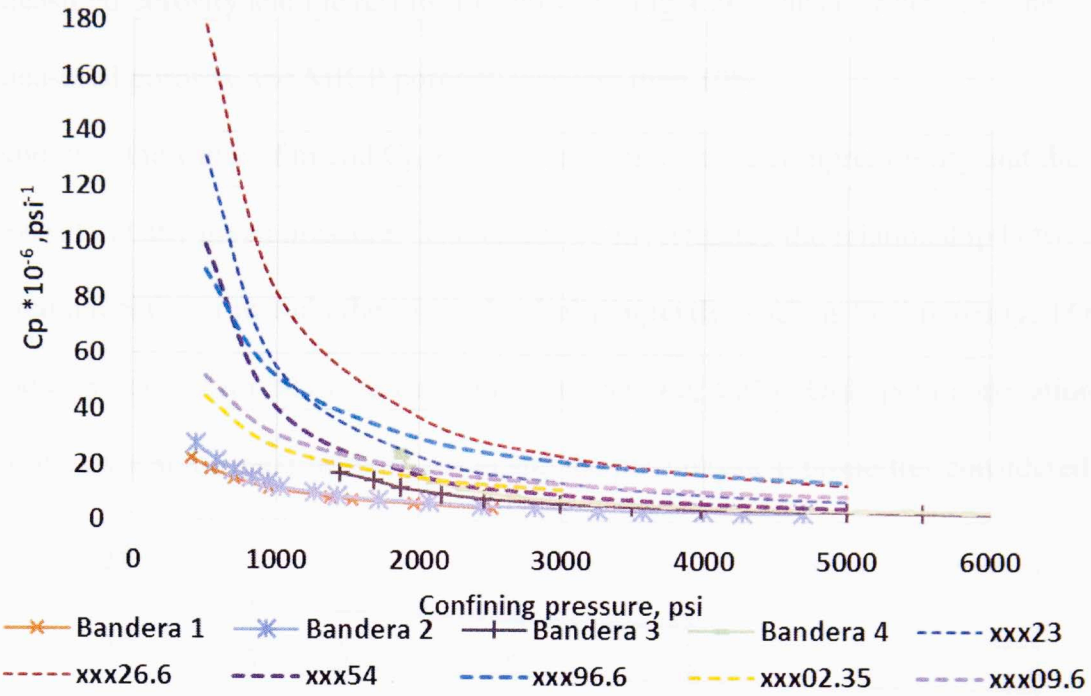

Fig 4.24: Comparison between MICP pore volume compressibility and published data on pore volume compressibility by Zimmerman (1984). The shale samples exhibit higher compressibility values compare to the published sandstones compressibility even at higher pressure where the difference is larger than 30 %.

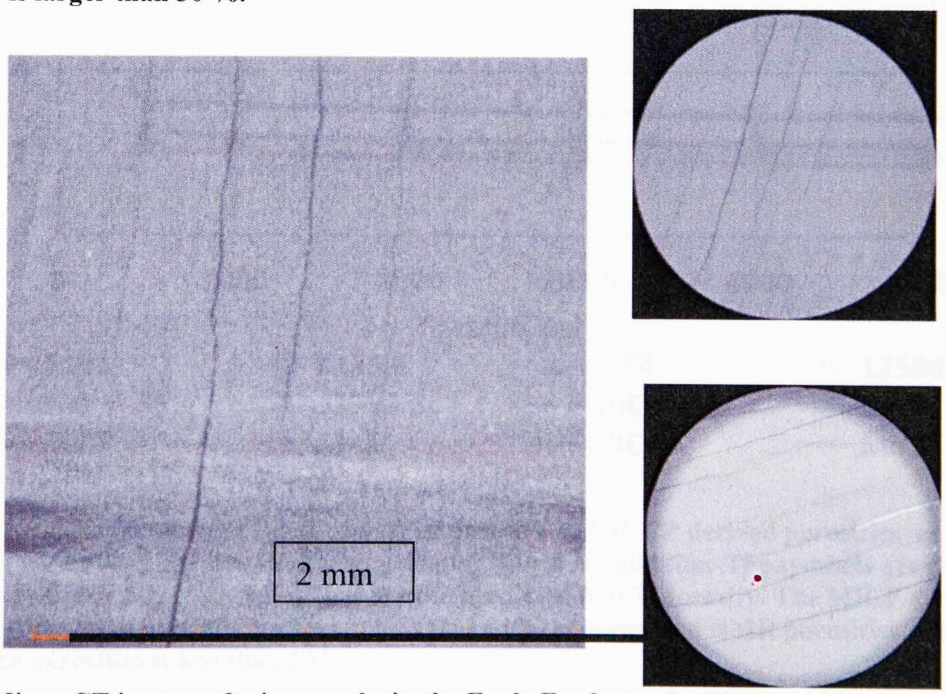

Fig 4.25: Micro-CT images of microcracks in the Eagle Ford sample (12596.6.) The average width of the imaged fracture is around 60 µm.

Based on the equation **4.5**, the MICP porosity as a function of pressure was computed for the selected samples. The predicted porosity from MICP was compared to the NMR

measured porosity and the results are shown in **Fig 4.26**. The error between the measured porosity and MICP porosity was less than 10%.

Knowing the value of m and C_{po} enables us to predict the compressibility and the porosity at any given pressure. Therefore, we investigated the relationship between the parameters C_{po} or m and other petrophysical **properties** such as total porosity, TOC, and clay content for all the shale formations (See **Fig 4.27**). Only poor correlations exist between the parameters C_{po} or m and the petrophysical properties considered.

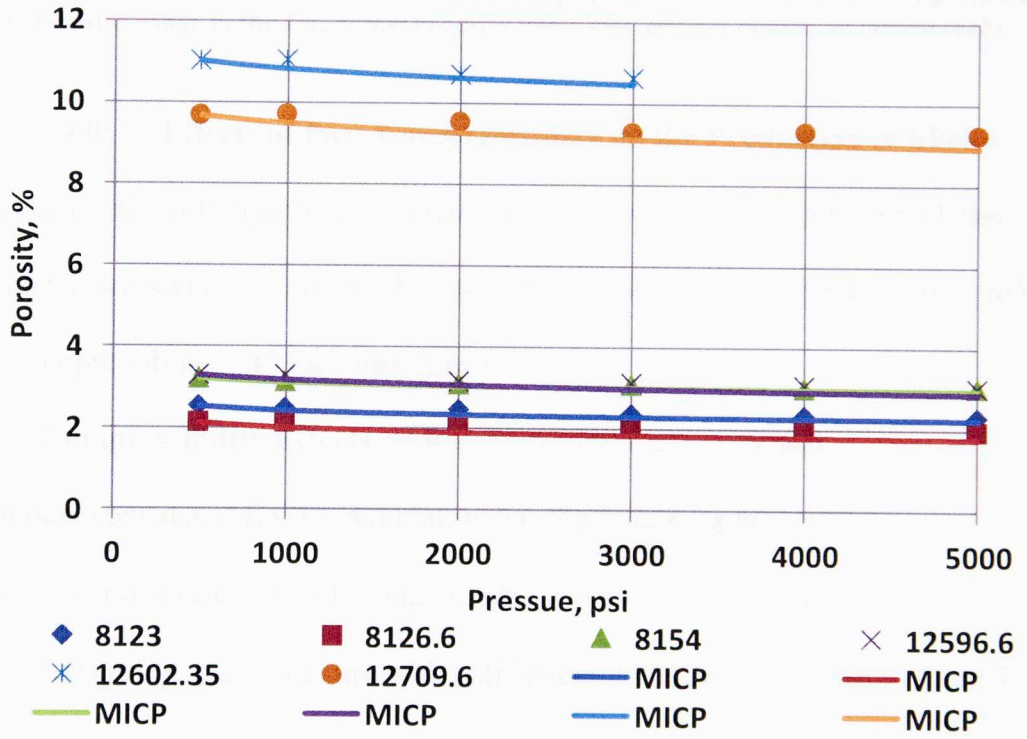

Fig 4.26: Comparison between NMR measured porosity and MICP derived porosities as function of pressure for Eagle Ford and Wolfcamp samples shown as solid line. The symbols are the measure NMR porosities. The solid lines are the predicted MICP porosity. The MICP derived porosities as function of confining pressures agree with the measured NMR porosities. The error between the porosities is less than 10%.

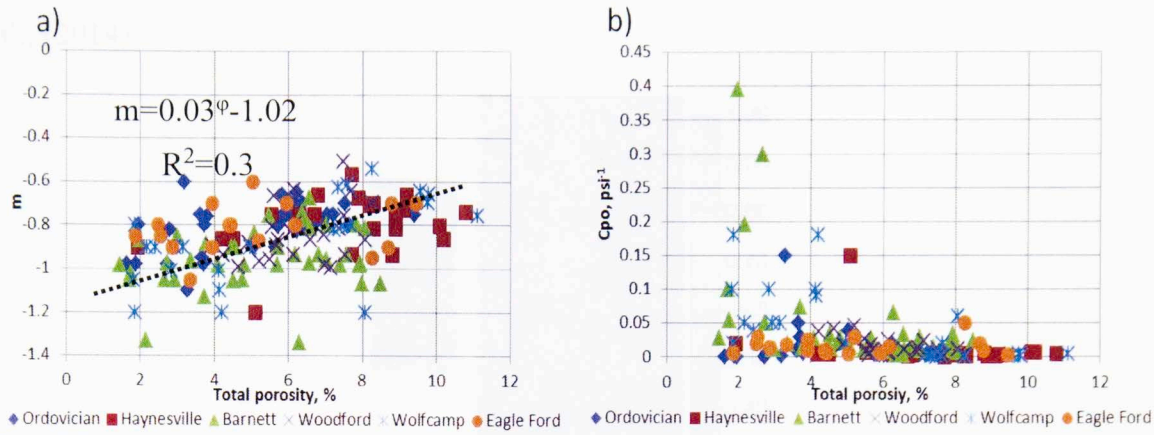

Fig 4.27: a) Plot of the m versus total porosity and b) Plot of C_{po} versus total porosity. No relationship was observed between m or C_{po} and any of the of the petrophysical properties of the shales. Greater range in the C_{p0} at low porosity value may greater density of microcracks.

4.9: Effects of Pore Compressibility on the Production in Shales

We examine the consequences of neglecting shale compressibility in model reservoirs. We model two scenarios outlined below, both are oil window models but one include shale compressibility and the other does not.

4.9.1: Compressibility Effects on Reservoir Simulation Model

The model considered for this simulation has the following parameters:

- Reservoir size: 1,325 ft. long, 525 ft. wide and 60 ft. thick
- 1 stage hydraulic fracture with half-length 250 ft. and a conductivity of 4 md-ft.
- Logarithmically spaced grids in the vicinity of the fracture
- Initial reservoir was 5,000 psia and the bottom hole pressure was set at 1,000 psi
- Maximum production rate was 420 Mscf per day

The reservoir is assumed to have similar reservoir fluid, porosity, and permeability as an Eagle Ford well located in the gas condensate window. A top view of the reservoir

model is shown in **Fig 4.28.** A full review of this model is also provided by Sanaei et al., (2014).

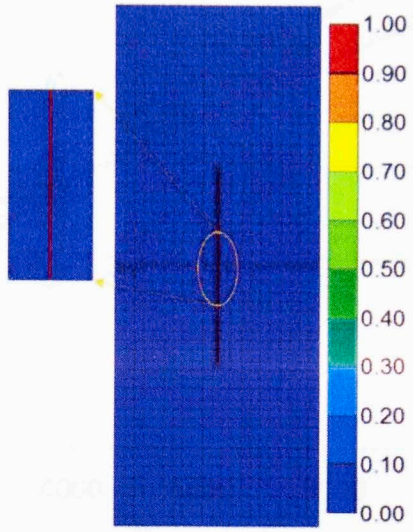

Fig 4.28: Top view of the reservoir model used for simulation (Sanaei et al., 2014).

4.9.2: Simulation Results

The effect of pore volume compressibility on the cumulative gas and oil condensate for a 30 year production history from the simulated reservoir is shown in **Fig 4.29-4.31**. The results of the simulation indicated that 2-15% higher production and recovery is predicted when compressibility is included. For instance, an increase of pore compressibility from 0 to $8*10^{-6}$ psi^{-1} caused 8% increase in production. A 15 % increase in production was achieved when the pore compressibility increased from $3*10^{-6}$ to $16*10^{-6}$ psi^{-1} This increase in production is driven by the decrease in the pore space due to higher compressibility and it is referred to as "formation compaction" (Hall, 1957). No substantial changes in gas production when the measured pore compressibility was included in the simulation; this was to be expected.

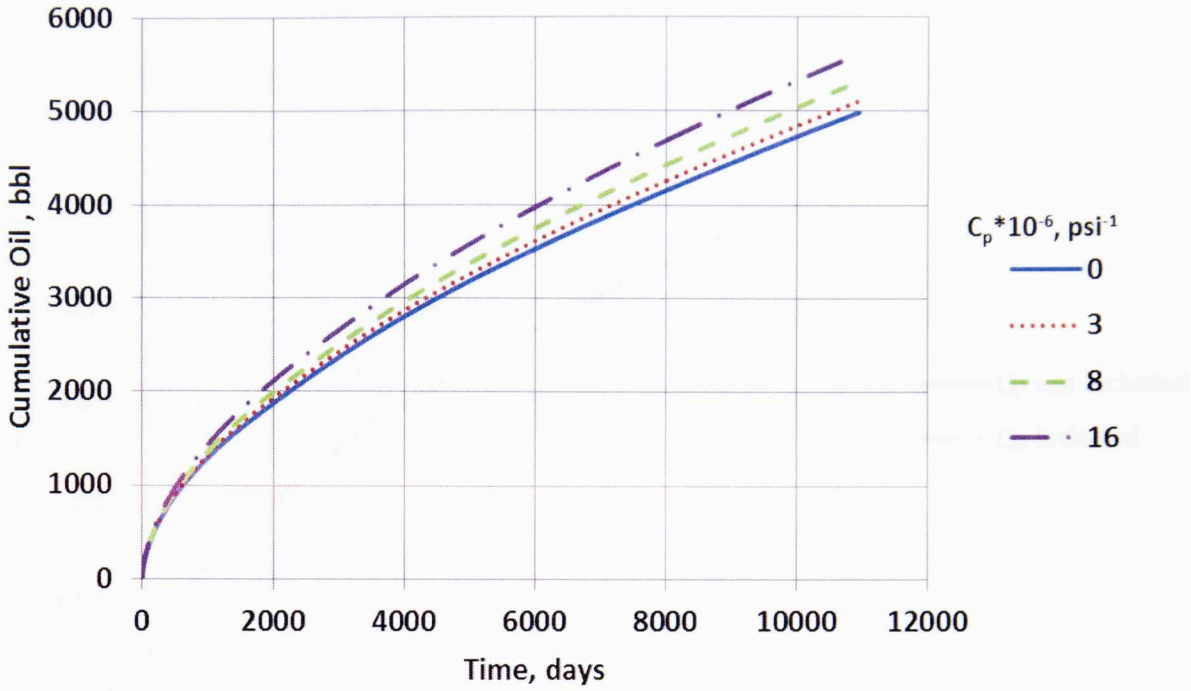

Fig 4.29: Cumulative oil production over 30 year period for an oil or condensate reservoir. Over 15 % increase in oil production was observed when the pore compressibility was increased from 3*10^{-6} to 16*10^{-6} psi^{-1}. All compressibility values are reported at 5,000 psi confining pressure.

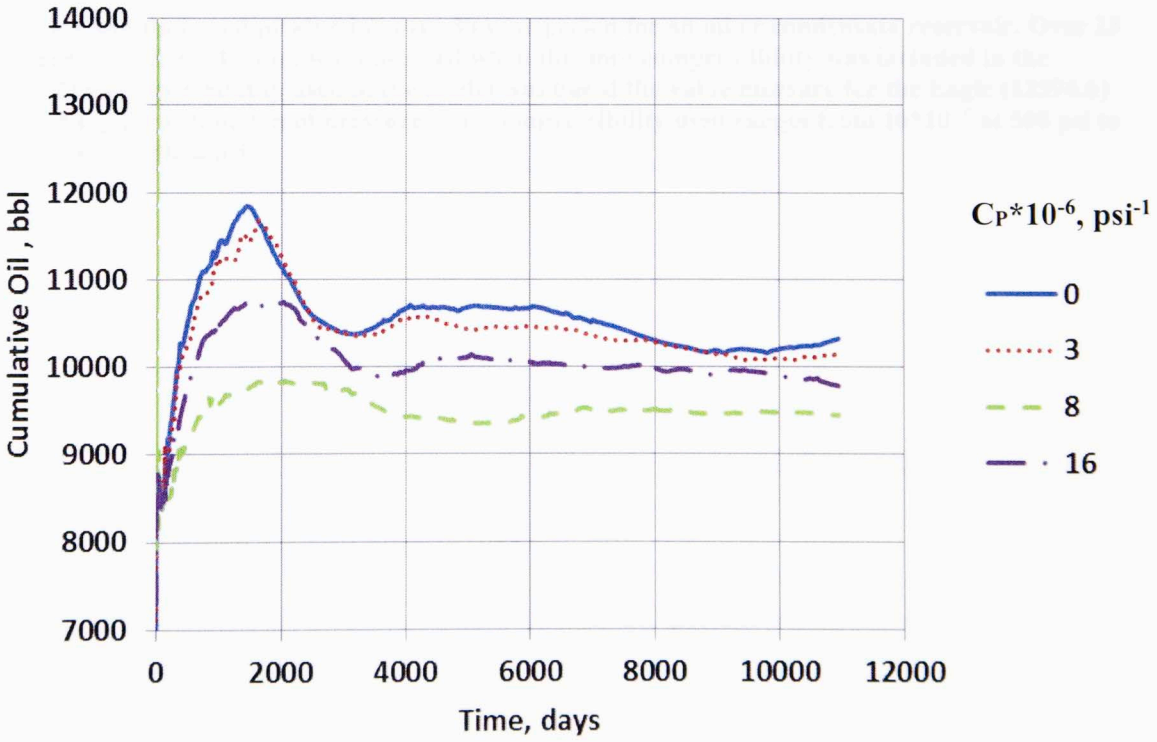

Fig 4.30: GOR for a 30 year period for an oil or gas condensate reservoir. Note the decrease in GOR caused by an increase in oil production when pore compressibility increases. All compressibility values are reported at 5,000 psi confining pressure.

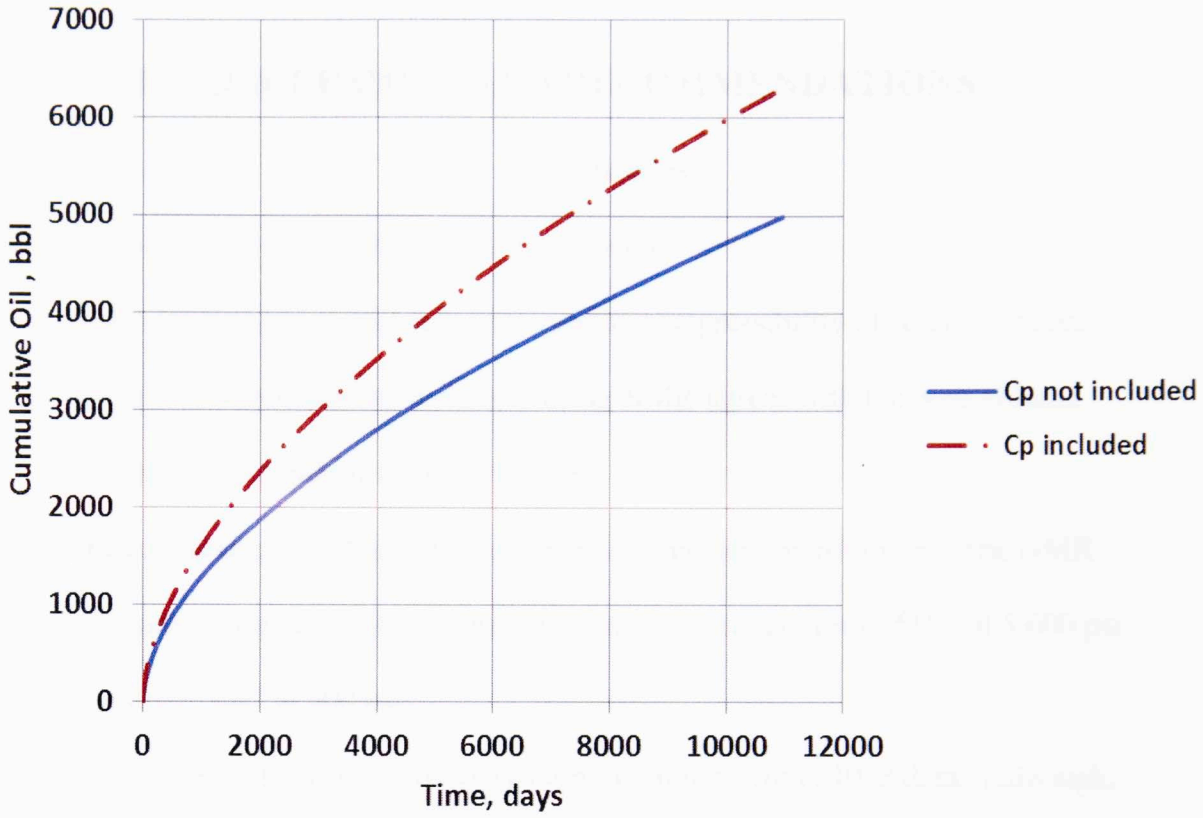

Fig 4.31: Cumulative oil production over 30 year period for an oil or condensate reservoir. Over 25 % increase in oil production was observed when the pore compressibility was included in the model. The compressibility used in the model was based the value measure for the Eagle (12596.6) and is changing as function of pressure. The compressibility used ranges from $16*10^{-5}$ at 500 psi to $16*10^{-5}$ psi-1 at 5000 psi^{-1}

5: CONCLUSIONS AND RECOMMENDATIONS

5.1: Conclusions

The main conclusions of this study are the following:

1. NMR can be used to measure pore volume compressibility of reservoir rocks. The pore compressibility measured using NMR agrees with the pore volume compressibility measured with AP 608.
2. Shale reservoirs exhibit significant pore volume compressibilities. The NMR measured compressibility for the different shales range from $2*10^{-6}$ at 5,000 psi to $18*10^{-5}$ psi^{-1} at 500 psi.
3. Bailey's model was used to derive compressibility from MICP data. Although, the Bailey's model has several limitations, the derived MICP compressibility closely match the NMR measured pore volume compressibility. Therefore, MICP can provide an estimate of pore compressibility in shales. The MICP compressibility ranges from $2*10^{-7}$ at 5, 000 psi to $12*10^{-5}$ psi^{-1}at 500 psi.
4. NMR measured pore volume compressibilities agree with the derived MICP compressibilities especially at high pressure.
5. Shale compressibility is mostly controlled by microcracks at low pressure, but this is not sensed in the MICP data.
6. Simulation results indicated that a significant production increase is predicted when the pore volume compressibility of shales is incorporated.
7. 2-25% errors in the prediction of oil and condensate reservoir occur if the compressibility is neglected.

REFERENCES

1. Adesida, A. 2011. Pore Size Distribution of Barnett Shale using Nitrogen Adsorption Data. Master's Thesis, University of Oklahoma, Norman, Oklahoma.
2. Adesida, A. G., Akkutlu, I. Y., Resasco, D. E., and Rai, C. S. 2011. Kerogen Pore Size Distribution of Barnett Shale Using DFT Analysis and Monte Carlo Simulations. SPE 147397 presented at the Annual Technical Conference in Denver, Colorado, USA, 30 October- 2 November.
3. Aguilera, R. F., and Radetzki, M. 2013. Shale Gas and Oil: Fundamentally Changing Global Energy Markets. *Oil and Gas Journal*. **V 11**. http://www.ogj.com/articles/print/volume-111/issue-12/exploration-development/shale-gas-and-oil-fundamentally-changing-global-energy-markets.html
4. Andersen, M. A. 1988. Predicting Reservoir-Condition PV Compressibility from Hydrostatics Stress Laboratory Data. *SPE Reservoir Engineering*, **V *3***, p 1-78. SPE 14213.
5. Bailey, S. 2009. Closure and Compressibility Corrections to Capillary Pressure Data in Shales. DWLS Workshop presented 19 October 2009, Golden, Colorado.
6. Barrett, E. P., Joyner, L. G., and Halenda, P. P. 1951. The determination of Pore Volume and Area Distributions in Porous Substances. I. Computations From Nitrogen Isotherms. *Journal of the American Chemical society*, **V 73**, P 373-380.
7. Ballard, B. 2007. Quantitative Mineralogy of Reservoir Rocks Using Fourier Transform Infrared Spectroscopy. SPE 113023 presented at the Annual Technical Conference and Exhibition, Anaheim, California, 11-14 November.
8. Berg, R. R., and Avery, A. H. 1995. Sealing properties of tertiary growth faults, Texas Gulf Coast. *AAPG bulletin*, v.*79*, p. 375-392.
9. Biot, M. A. 1941. General Theory of Three-Dimensional Consolidation. *Journal of applied physics*, **V 12**, p 155-164.
10. Boggs, S. 2009. *Petrology of Sedimentary Rocks*. Second edition. New York: Cambridge University Press.
11. Brown, R. J., and Fatt, I. 1956. Measurements of Fractional Wettability of Oil Fields' Rocks by the Nuclear Magnetic Relaxation Mmethod. SPE 743, paper presented at the Fall Meeting of the Petroleum Branch of AIME, Los Angeles, California, 14-17 October.
12. Bohacs, K. M., Pasey, Q. R., Rudnicki, M., Esch, W. L., and Lazar, O. R. 2013. The Spectrum of Fine-Grained Reservoirs from 'Shale Gas' to 'ShaleOil'/Tight Liquids: Essential Attributes, Key Controls, Practical Characterization. IPTC 16676 presented at the International Petroleum Technology Conference, Beijing, China, 26-28 March.
13. Born, W. T., and Owen, J. E. 1935. Effect of Moisture Upon Velocity of Elastic Waves in Amherst Sandstone. *AAPG Bulletin*, **V 19**, p 9-18.
14. Bustin, R. M., Bustin, A. M., Cui, A., Ross, D., and Pathi, V. M. 2008. Impact of Shale Properties on Pore Structure and Storage Characteristics. SPE 119892

presented in SPE Shale Gas Production Conference, Fort Worth, Texas, USA, 16-18 November

15. Calderon, W.B. 2012. Acoustic and Topological Characterization of Organic Matter in Shales. Master's Thesis, University of Oklahoma, Norman, Oklahoma.
16. Calderon, W.B., Sondergeld, C., and Rai, C. 2013. Acoustic Mapping and Characterization of Organic Matter in Shales. SPE 166331, presented at SPE Annual Technical Conference in New Orleans, Louisiana, USA, 30 september-October .
17. Coates, G. R., Xiao, L., Prammer, M. G., and Logging, NMR. 1999. Principles and Applications. *Halliburton Energy Services, Houston*.
18. Chalmers, G. R., and Bustin, R. M. 2008. Lower Cretaceous Gas Shales in Northeastern British Columbia, Part I: Geological Controls on Methane Sorption Capacity. *Canadian petroleum geology Bulletin*, **V 56**, p 1-21.
19. Chalmers, G., Bustin, M., and Power, I. 2012. Characterization of Gas Shale Pore System by Porosimetry, Pycnometry, Surface Area, and Field Emission Scanning Electron Microscopy/Transmission Electron Microscopy Image Analyses: Examples from the Barnett, Woodford, Haynesville, Marcellus, and Doig Units. *AAPG Bulletin V* **96**, p 1099-1119.
20. Clarkson, C. R., Wood, J., Burgis, S., Aquino, S., and Freeman, M. 2012. Nanopore-Structure Analysis and Permeability Predictions for a Tight Gas Siltstone Reservoir by Use of Low-Pressure Adsorption and Mercury-Intrusion Techniques. SPE155537 presented at the Americas Unconventional Resources in Pittsburgh, Pennsylvania, 5-7 June.
21. Comisky, J. T., Santiago, M., McCollom, B., Buddhala, A., and Newsham, K. E. 2011. Sample Size Effects on the Application of Mercury Injection Capillary Pressure for Determining the Storage Capacity of Tight Gas and Oil Shales. SPE 149432, paper presented at the Canadian Unconventional Resources Conference, Alberta, Canada, 15-17 November.
22. Curtis, M., Cardott, B., Sondergeld, C., and Rai, C. S. 2012. Development of Organic Porosity in the Woodford Shale with Increasing Thermal Maturity. *International Journal of Coal Geology*. **V 103**, p 26-31.
23. Curtis, M. E., and Rai, C. S. 2013. Relationship Between Organic Shale Microstructure and Hydrocarbon Generation. SPE 164540, paper presented at the Unconventional Resource Conference, Woodlands, Texas, 10-12 April.
24. Curtis, M., Cardott, B., Sondergeld, C., and Rai, C. S. 2012. Development of organic Porosity in the Woodford Shale Related to Thermal maturity. SPE 160158 presented at the Annual Technical Conference and Exhibition, San Antonio, Texas, 8-10 October.
25. Curtis, M.E., Ambrose, R.J., Sondergeld, C.H., and Rai, C.S. 2010. Structural Characterization of Gas Shales on the Micro- and Nano-Scales. SPE 137693 presented at the Canadian Unconventional Resources & International Petroleum Conference, Calgary, Alberta, Canada, and 19-21 October. 30 October-1 November.
26. Dastidar, R. 2007. Nuclear Magnetic Resonance (NMR) Study of Thawing of Saturated Porous Media and Application to Shale and Pore Volume Compressibility Estimation. PhD Thesis, University of Oklahoma, Norman,

Oklahoma
27. Dastidar, R. 2004. Integrating NMR with other Petrophysical Parameters to Characterize a Turbidite Reservoir. MS thesis, University of Oklahoma, Norman, Oklahoma.
28. Dow, W. G. 1977. Kerogen Studies and Geological Interpretations. Journal of Geochemical Exploration, **V 7**, p 79-99.
29. Durand, Bernard, ed. 1980. *Kerogen: Insoluble Organic Matter From Sedimentary Rocks*. Paris: Editions Technip.
30. Dunn, K. J., Bergman, D. J., and LaTorraca, G. A. 2002. *Nuclear Magnetic Resonance: Petrophysical and Logging Applications*. Handbook of Geophysical Exploration. Elsevier.
31. EIA, 2011 Annual Energy Outlook. U.S. Department of Energy, Washington, DC
32. EIA, 2012 Annual Energy Outlook. U.S. Department of Energy, Washington, DC
http://www.eia.gov/energy_in_brief/article/about_shale_gas.cfm
33. Geertsma, J. 1956. The Effect of Fluid Pressure Decline on Volumetric Changes of Porous Rocks. SPE 728G paper presented at the Fall Branch Meeting of American Institute of Mining, Metallurgical, and Petroleum Engineers, Los Angeles California, 14-17.
34. Geertsma, J. 1966. Problems of Rock Mechanics in Petroleum Production Engineering. Presented at the 1st ISRM Congress, Lisbon, Portugal, 25 September- 1 October.
35. Greenwald, R. F., and Somerton, W. H. 1981. Pore Volume Compressibility Data For Bandera Berea And Boise Sandstones. SPE 9746.
36. Griffiths, P., and De Haseth, J. A. 1986. *Fourier Transform Infrared Spectrometry*.New Jersey: John Wiley & Sons.
37. Guo, X. Q., Liu, D. M., Yao, Y. B., Cai, Y. D., and Li, J. Q. 2013. Influence of Pressure on Application of Mercury Injection Capillary Pressure for Determining Coal Compressibility. Applied Mechanics and Materials, **V 295**, p 2726-2731.
38. Haldar, S. k., and Tišljar, J.2014. *Introduction to Mineralogy and Petrology*. Oxford, UK: Elsevier
39. Hall, H. N. 1953. Compressibility of Reservoir Rocks. *Journal of Petroleum Technology*, **V 5**, p 17-19.
40. Herron, M. M., and Matteson, A. 1993. Elemental Composition and Nuclear Parameters of Some Common Sedimentary Minerals. *The International Journal of Radiation Applications and Instrumentation. Part E. Nuclear geophysics*, **V 7**, p 383-406.
41. Herron M., A. Matteson, and Gustavson. G. 1997. Dual-Range FT-IR Mineralogy and the Analysis of Sedimentary Formations, paper 9729 presented at the International Symposium of the Society of Core Analysts, 7 – 10September.
42. Hildenbrand, A. A., and Urai, J. L. 2003. Investigation of the Morphology of Pore Space in *Mudstones-First Results. Marine and Petroleum Geology*, **V 20**: 1185-1200.

43. Jarvie, D. M., Claxton, B., Henk, B., and Breyer, T. 2001. Oil and Gas from Barnett Shale, Ft Woryh Basin, Texas. Presentation given at the AAPG National Convention, Denver, Colorado, 3-6 June.
44. Kale, S. 2009. Petrophysical Characterization of Barnett Shale Play. Master's Thesis, University of Oklahoma, Norman, Oklahoma.
45. Karastathis, A. 2007. Petrophysical Measurements on a Tight Gas Shale, Master's Thesis, University of Oklahoma, Norman, Oklahoma.
46. Kleinberg, R. L. 1996. Utility of NMR T2 Distributions, Connection With Capillary Pressure, Clay Effect, and Determination of the Surface Relaxivity Parameter ρ2 . *Magnetic Resonance Imaging*, **V *14***, p 761-767.
47. Klinkenberg, L. J., 1941. The Permeability of Porous Media to Liquids and Gases: *Drilling and Production Practice* ,**V 41**: p 200-213.
48. Kulia, U., Prasad, M., Derkowski, A., and McCarty, D. K. 2012. Compositional Controls on Mudrock Pore-Size Distribution: An Example from Niobrara Formation. SPE 160141 presented at the SPE Annual Technical Conference and Exhibition, San Antonio, Texas, 8-10 October.
49. Loucks, R. G., Reed, R. M., Ruppel, S. C., and Hammes, U. 2012. Spectrum of Pore Types and Networks in Mudrocks and a Descriptive Classification for Matrix-Related Mudrock Pores. *AAPG bulletin*, **V *96*,** p 1071-1098.
50. Loucks, R. G., Ruppel, S., Reed, R., and Hammes, U. 2011. Origin and Classification of Pores in Mudstones from Shale-Gas Systems. AAPG Search and Discovery Article#40855.
51. Loucks, R. G., Reed, R. M., Ruppel, S. C., and Jarvie, D. M. 2009. Morphology, Genesis, and Distribution of Nanometer-ScalePpores in Siliceous Mudstones of the Mississippian Barnett Shale. *Journal of Sedimentary Research*, **V 79**, p 848-861.
52. Majling, J., Komarneni, S., and Fajnor, V. S. 1995. Mercury Porosimeter as a Means to Measure Mechanical Properties of Aerogels. *Journal of Porous Materials*, **V 1**, p 91-95.
53. Moncrieff, J. 2009. Microstructure of Shale. Poster presentation SPWLA Annual meeting in Houston, Texas.
54. Nelson, J.S and Simoons, E.S. 1992. The Quantification of Diffusive Hydrocarbon Loss Through Cap Rocks of Natural Gas Reservoirs-Re-Evaluation, *AAPG bulletin*, **V *76***, p.1839-1841.
55. Newman, G. H. 1973. Pore-Volume Compressibility of Consolidated Friable and Unconsolidated Reservoir Rocks Under Hydrostatic Loading. *Journal of Petroleum Technology,* **V 2**, p 129-134.
56. Evans, R. J., Nieto, J. A., and Yale, D. P. 1994. Improved Methods for Correcting Core Porosity to Reservoir Conditions. *The Log Analyst*, **V 35**.
57. Odusina, E. 2011. An NMR Study of Shale Wettability. Master's Thesis, University of Oklahoma, Norman, Oklahoma.
58. Passey, Q. R., Bohacs, K. M., Esch, W. L., Klimentidis, R., and Sinha. S. 2010. From Oil-Prone Source Rock to Gas-Producing Shale Reservoir-Geologic and Petrophysical Characterization of Unconventional Shale-Gas Reservoirs. SPE 131350 presented at the CPS/SPE international OIL& Gas Conference and Exhibition, Beijing, China, 8-10 June.

59. Passey, Q. R., Creaney, S., Kulla, J. B., Moretti, F. J., and Stroud, J. D. 1990. A Practical Model for Organic Richness from Porosity and Resistivity Logs. *AAPG bulletin*, **V.*74***, p.1777-1794.
60. Peters, K., and Cassa, M. R. 1994. Applied Source Rock Geochemistry. *The Petroleum System, From Source to Trap*. Chap 5, p 93-120. AAPG Memoir 60.
61. Potter, P. E., J. B. Maynard, and P. J. Depetris. 2005. *Mud and Mudstones*: Berlin Springer.
62. Pittman, E. D. 1992. Relationship of Porosity and Permeability to Various Parameters Derived from Mercury Injection-Capillary Pressure Curves for Sandstone. *AAPG bulletin*, **V *76***, p 191-198.
63. Purcell, W. R. 1949. Capillary Pressures-Their Measurement Using Mercury and the Calculation of Permeability Therefrom. Journal of Petroleum Technology, V 1,p 39-48. SPE 949039.
64. Rieke III, H. H., Oliver, D. W., Fertl, W. H., and McCord, J. P. 1983. Successful Application of Carbon/Oxygen Llogging to Coalbed Exploration. Presented at 55 th Annual Technical Conference of the Society of Petroleum Engineers, Dallas Texas 21-24, 1980.
65. Ross, D. J., and Bustin, R. M. (2008). Characterizing the Shale Gas Resource Potential of Devonian–Mississippian Srata in the Western Canada Sedimentary Basin: Application of an integrated formation evaluation. *AAPG bulletin*, **V *92***, p 87-125
66. Rushing, J. A., Newsham, K. E., and Blasingame, T. A. 2008. Rock Typing: Keys to Understanding Productivity in Tight Gas Sands. SPE 114164, paper presented at the Unconventional Reservoirs Conference, Keystone, Colorado, 10-12 February.
67. Schieber, J.2010. Common Themes in the Formation and Preservation of Intrinsic Porosity in Shales and Mudstones-Illustrated with Examples Across the Phanerozoic. SPE 132370, paper presented at the Annual SPE Unconventional Gas Conference in Pittsburg, Pennsylvania, USA, 23-25 February.
68. Schlömer, S., and Krooss, B. M. 1997. Experimental Characterization of the Hydrocarbon Sealing Efficiency of Cap Rocks. *Marine and Petroleum Geology*, **V *14***, p.565-580.
69. Schmoker, J. W. 1979. Determination of Organic Content of Appalachian Devonian Shales from Formation-Density Logs. *AAPG Bulletin*, **V *63*,** p. 1504-1509.
70. Schmoker, J. W. 1981. Determination of Organic-Matter Content of Appalachian Devonian Shales from Gamma-Ray Logs. *AAPG bulletin*, **V *65***, p.1285-1298.
71. Sigal, R. F. 2009. A Methodology for Blank and Conformance Corrections for High Pressure Mercury Porosimetry. *Measurement Science and Technology*, V *20*.
72. Sigal, R. F., and Odusina, E. 2011. Laboratory NMR Measurements on Methane Saturated Barnett Shale Samples. *Petrophysics*, **V *52***, p 32-49.
73. Slatt, R. M., and O'Brien, N. R. 2011. Pore Types in the Barnett and Woodford Gas Shales: Contribution to Understanding Gas Storage and Migration Pathways in Fine-Grained Rocks. *AAPG bulletin*, **V 95**, p 2017-2030.

74. Sondergeld, C., Ambrose, R. J., Rai, C. S., and Moncrieff, J. 2010. Micro-Structural Studies of Gas Shales. SPE 131771 presented at the Unconventional Gas Conference, Pittsburgh, Pennsylvania, 23-25 February.
75. Sondergeld, C.H. and Rai, C.S. 2011. Elastic Anisotropy of Shales. *The Leading Edge* **30**: p 324-331.
76. Sondergeld, C.H. and Rai, C.S. 1993. A New Concept in Quantitative Core Characterization. *The leading Edge* **V 12**: p 774-779.
77. Kale, S. 2009. Petrophysical Characterization of Shale Play. Master's Thesis, University of Oklahoma, Norman, Oklahoma
78. Sondhi, N. 2011. Petrophysical Characterization of Eagle Ford Shale. Master's Thesis, University of Oklahoma, Norman, Oklahoma.
79. Straley, C., Rossini, D., Vinegar, H. J., Tutunjian, P., and Morriss, C. E. 1997. Core Analysis by Low-Field NMR. *Log Analyst*, V *38*, p 84-94.
80. Sulucarnain, I. 2013. An NMR Study of Shale Wettability and Effective Surface Relaxivity. Master's Thesis, University of Oklahoma, Norman, Oklahoma.
81. Teeuw, D. 1970. Prediction of Formation Compaction from Laboratory Compressibility Data. SPE 2973, In *Journal of Petroleum Technology*. **V 22**, p 1049
82. Thommes, M. 2010. Physical Adsorption Characterization of Nanoporous Materials. *Chemie Ingenieur Technik*, **V** *82*(7), 1059-1073.
83. Tiab, D., and Donaldson, E. C.2012. *Petrophysics: Theory and Practice of Measuring Reservoir Rock and Fluid Transport Properties*. Third edition. Oxford: Gulf professional publishing.
84. Tinni, A. 2013. Application of Nitrogen Gas Adsorption Methods to Study the Surface Area and Pore Size Distribution of Various Shales. Presented at the Annual Unconventional Shale Consortium meeting, Norman, Oklahoma, 10-11 June.
85. Tinni, A. 2013. NMR Response of Pressure Saturated Shales. Presented at the Annual Unconventional Shale Consortium meeting, Norman, Oklahoma, 10-11 June.
86. Tissot, B., Durand, B., Espitalie, J., and Combaz, A. 1974. Influence of Nature and Diagenesis of Organic Matter in Formation of Petroleum. *AAPG bulletin*, **V** *58*, p 499-506.
87. Tissot, B. P., and Roucache, J. 1980. Principles of a Genetic Classification of Crude Oils. *Canadian Society of Petroleum Geologist*, p 1-9.
88. Tissot, B. P., Pelet, R., and Ungerer, P.H. 1987. Thermal History of Sedimentary Basins, Maturation Indices, and Kinetics of Oil and Gas Generation. *AAPG bulletin,* **V 71**: p. 1445-1466.
89. Valenza, j., Drenzek, N., Marques, F., Pagels, M., and Mastalerz, M. 2013. Geochemical Controls on Shale Microstructure. http://geology.gsapubs.org/content/early/2013/03/15/G33639.1.full.pdf+html (downloaded 20 September 2013).
90. Van der Knaap, W. 1959. Nonlinear Behavior of Elastic Porous Media. SPE 1124G, presented at The Annual Fall Meeting of SPE, Houston, Texas, 3-8 October..
91. Walsh, J.B. 1981. Effect of Pore Pressure and Confining Pressure on Fracture

Permeability. *Int. J. Rock Mech. Min. Sci. Geomech.* **V 18**: p 429-435.
92. Von Goten, W. D., and Choudhary, B. K. 1969. The Effect of Pressure and Temperature on Pore Volume Compressibility. SPE 2526, paper presented at the Fall Meeting of the Society of Petroleum Engineers of AIME, Denver Colorado, 28 September-1 October.
93. Wang, F. P., and Reed, R. M. 2009. Pore Networks and Fluid Flow in Gas Shales. SPE 125253, paper presented the Annual Technical Conference and Exhibition, New Orleans, LA, 4-7 October.
94. Washburn, E. W. 1921. Note on a Method of Determining the Distribution of Pore Sizes in a Porous Material. *Proceedings of the National Academy of Sciences of the United States of America*, p 115-116.
95. Washburn, K. E., and Birdwell, J. E. 2013. A New Laboratory Approach to Shale Analysis Using NMR Relaxometry. SPE 168798, paper presented at the Unconventional Resources Technology Conference, Denver, Colorado, 12-14 August
96. Winkler, M., Freeman, J., Quint, E., and Caputi, M. 2006 . Evaluating Tight Gas Reservoirs with NMR-The Perception The Reality and How to Make it work. Presented at the SPWLA 47th Annual Logging Symposium, Veracruz, Mexico, 4-7 June.
97. Zimmerman, R. W. 1991. *Compressibility of Sandstones*. New York:USA. Elsevier Science Publisher B.V.

APPENDIX-A

FTIR measurement steps

- A Representative amount of the sample is crushed into fine size powder (with particle < 25 μm)
- The crushed sample is dried at 100° C in vacuum oven for 12 hrs. to remove any moisture
- The sample is oxidized in low temperature (40-50° C) plasma asher to remove any organic carbon or CO_2
- 0.5 mg of the sample is mixed with 300 mg of KBr and pressed into a disc.
- A background is collected using 300 mg of pure KBr pressed into a disc before any measurement
- The pellet disc is inserted into FTIR spectrometer and the unknown sample spectra is collected.
- The background spectra is subtracted from the sample spectra
- The obtained spectra is inverted for mineral contents

Fig A1: Nicolet 6700 Transmission Fourier Transform Infrared Spectrometer (Odusina, 2011).

LECO measurement steps

- 8-10 g of sample finely crushed and sieved sample (40 mesh).
- Inorganic is remove by soaking the sample into HCl for 12 – 16 hrs.
- When no reaction is observed between the sample and acid, the sample is washed and dried inside an oven at 100°C for 15 minutes.
- After drying, the sample is mixed with both copper and iron accelerators.
- The sample is placed inside the Leco TOC analyzer where it is oxidized into CO_2 at high temperature (900° C for 1 minute).
- An infrared detector is used to record the quantity of CO_2 released during the combustion in the high temperature furnace.

SRA measurement steps

- Approximately 100 g of crushed and heated in programmed temperature (25° C/min) in an inert environment.
- A Flame-Ionization Detector (FID) is used to record the quantity of gas released during the heating stage.

- The first stage involves the release of free hydrocarbons characterized by the S1 peak when the temperature is increased to 300°C and held constant.
- The next step involved the release of hydrocarbon and CO_2 yielding the S2 and S3 peaks, respectively. The hydrocarbon expelled at this stage results from the cracking of remaining kerogen and bitumen due to the increase in temperature from 300°C to 600°C.
- The temperature associated with the maximum in the S2 peak is known as Tmax and is expressed in °C. This temperature provides an indication of the maturity level of the sample.
- A fourth peak denoted by S4 is also recorded and represents the residual carbon or "dead carbon".

LPP measurements steps

- Obtain a sample 8-12 g
- Dry sample in a vacuum oven at 100° C for at least 8 hr. to remove any water
- Cool the sample in a desiccator for at least 30 minutes
- Measure sample bulk volume (from mercury displacement or measuring dimensions)
- Record the initial weight w_1 of the sample
- Crush the sample (with extreme care) with a pestle in a sealed crucible.
- Carefully transfer the crushed sample into the pycnometer aluminum cell
- Record the second weight of sample and calculate the weight loss. If weight loss exceeds 0.75% of the initial weight, discard this sample and start over.

- Dry sample again at 100° C for 8 hr. to remove any remaining water or hydrocarbon
- Place the aluminum cell into the AccuPyc II 1330 to determine the average grain volume

Fig A2: a) Micrometrics AccuPyc II 1330 used to measure total porosity for shale. b) Mortar, pestle and sieve used to crushed and measure sample size before measuring total porosity (Comisky et al., 2011).

MICP measurements steps

- 8-10 g of chips, cuttings, or plugs sample is collected and dried for 24 hrs. in a convection oven at 100°C.
- The sample is placed in a desiccator for 30 minutes to cool to room temperature.
- The sample's weight and volume are recorded.
- The sample is placed in a penetrometer which is composed of a cylindrical glass bulb where the sample is placed and a hollow capillary stem which will be filled and pressurized with mercury.
- The penetrometer containing the sample is first placed in the low pressure section of the Autopore IV.
- The sample is evacuated at 50 μmHg pressure for 30 minutes to remove any moisture or air bubbles before the stem is backfilled with mercury.

- The mercury pressure is increased to 30 predefined pressure points (~25 psi) where mercury volume is recorded after pressure equilibrium is reached.
- The low pressure stage stops at approximately 25 psi capillary pressure. The penetrometer containing the sample and the mercury is weighed again and carefully transferred to the high pressure chamber where pressure is increased in logarithmic steps to 60 kpsi.
- After reaching the maximum allowable pressure (60 kpsi), the mercury capillary pressure is decreased to 20 psi. The mercury is drained using fewer pressure points. The hysteresis separating the intrusion and the extrusion is an indication of mercury intruding the sample and provides qualitative index to group similar rock type (Sagar, 2009).

Compressibility measurement steps

The sample was first jacketed in a FEP (Fluororinated ethylene propylene) sleeve and placed between two solid and cylindrical end plugs made of Peek (Polyetheretherketones). O-rings were placed above and below the end plugs to provide a seal for the saturated sample. Confining pressure ranging from 0 to 5000 psi was applied in steps on sample using fluorinet fluid (FC770). Fluorinet has no hydrogen; thus it does not generate any NMR signal. A Teledyne Isgo pump was used to increase the pressure inside the vessel. At each of the defined pressure points, a one hour waiting period is required for pressure equilibrium. Throughout the experiment the temperature was maintained at 35°C.

APPENDIX-B

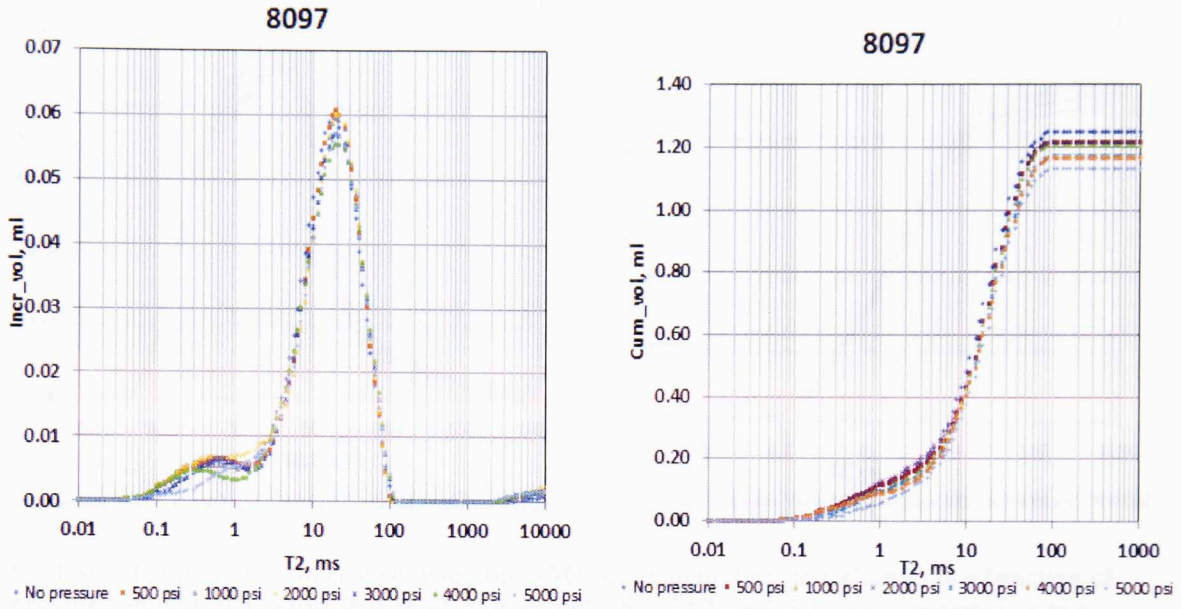

Fig B1:a) T_2 relaxation spectra showing the NMR incremental volume change as a function of pressure on dodecane saturated Wolfcamp sample. b) NMR cumulative volume change as a function of function of pressure for the Wolfcamp 8097. Note the decrease in pore volume at small T2 relaxation and the decrease of the cumulative NMR pore volume as function of increasing pressure.

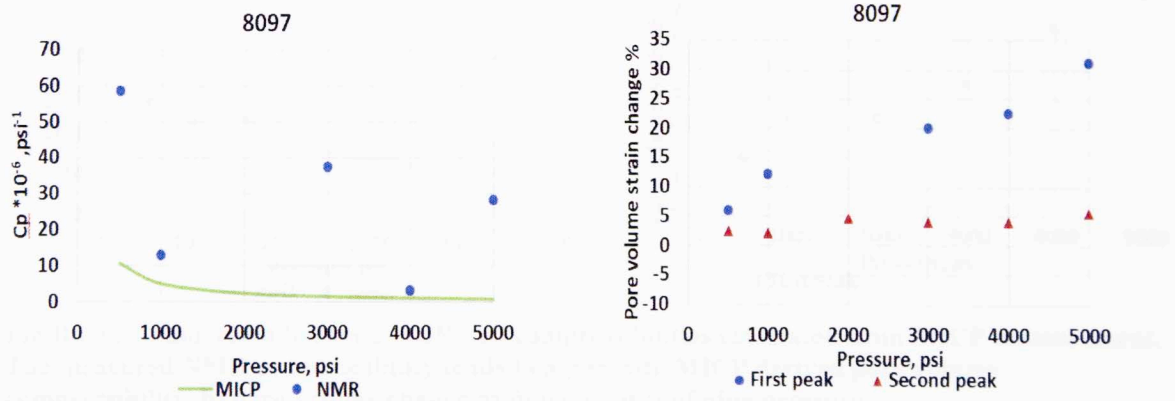

Fig B2:a) Comparison between NMR and compressibilities calculated from MICP measurement. The measured NMR compressibility tends to agree with MICP derived pore volume compressibility. b) pore volume change as function of confining pressure.

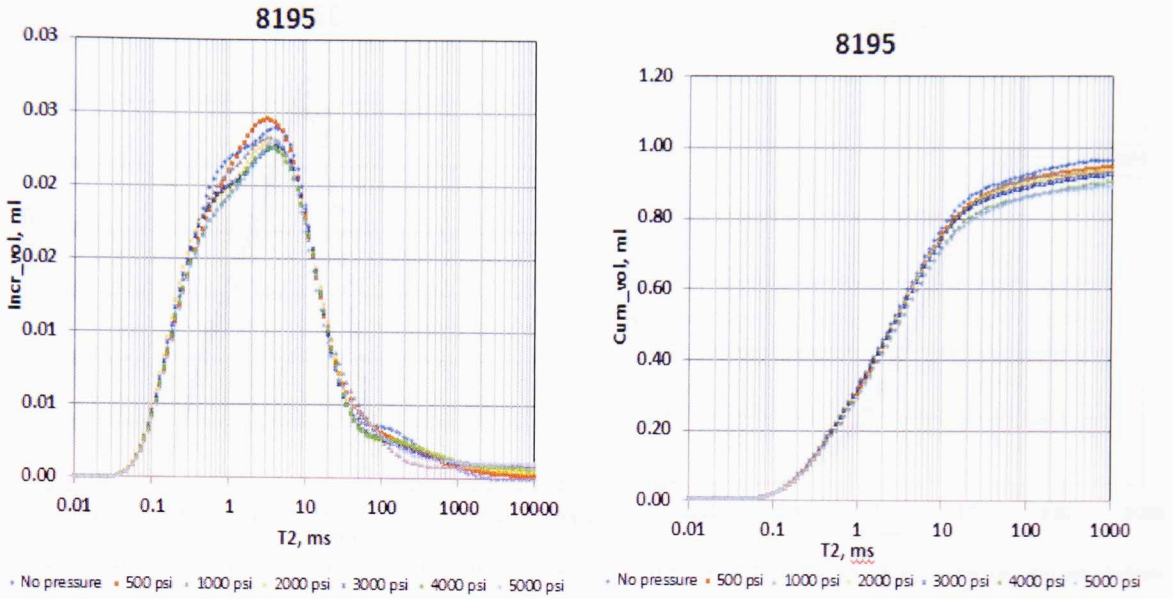

Fig B3:a) T_2 relaxation spectra showing the NMR incremental volume change as a function of pressure on dodecane saturated Wolfcamp sample. b) NMR cumulative volume change as a function of function of pressure for the Wolfcamp 8195 Note the decrease in pore volume at small T2 relaxation and the decrease of the cumulative NMR pore volume as function of increasing pressure

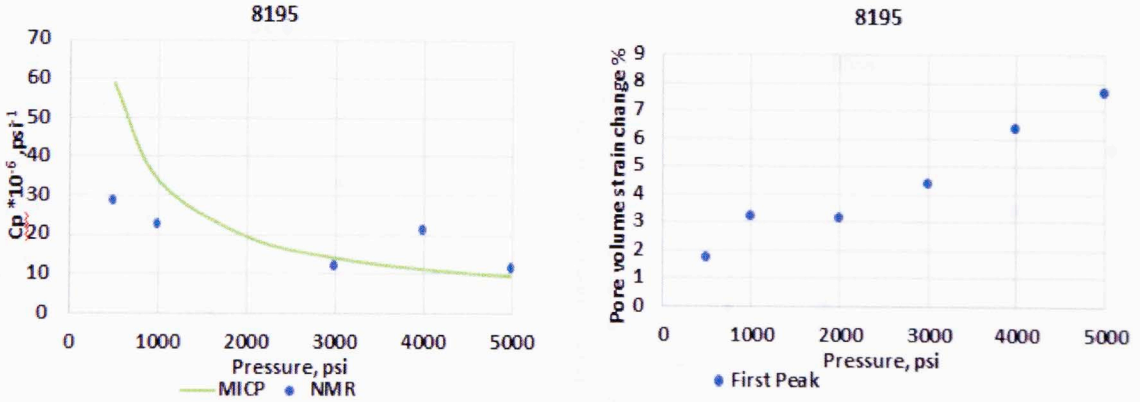

Fig B4:a) Comparison between NMR and compressibilities calculated from MICP measurement. The measured NMR compressibility tends to agree with MICP derived pore volume compressibility. b) pore volume change as function of confining pressure.

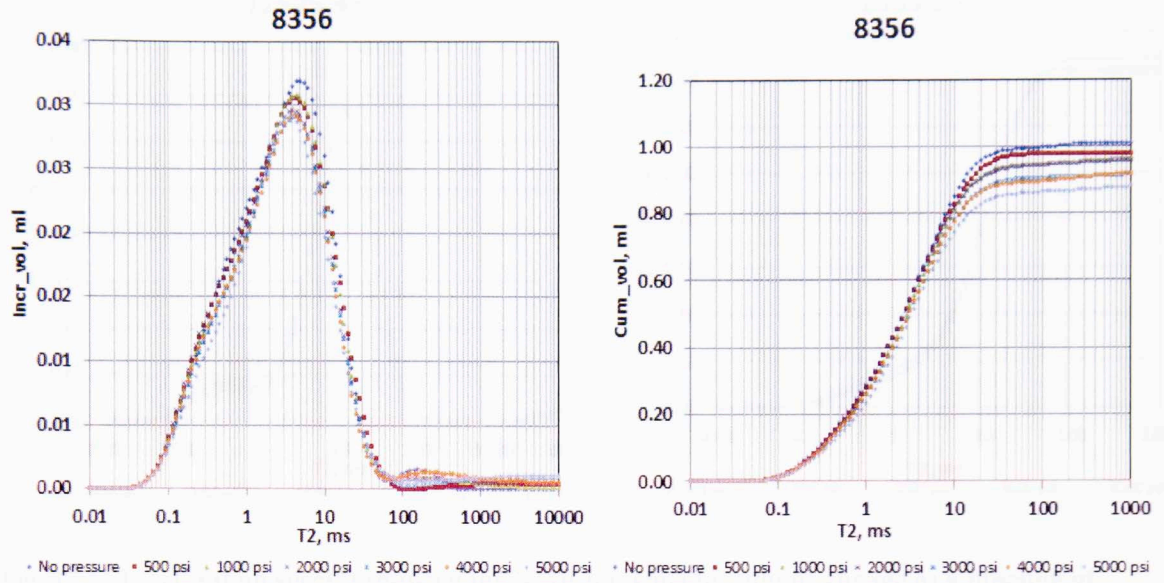

Fig B5:a) T_2 relaxation spectra showing the NMR incremental volume change as a function of pressure on dodecane saturated Wolfcamp sample. b) NMR cumulative volume change as a function of function of pressure for the Wolfcamp 8356. Note the decrease in pore volume at small T2 relaxation and the decrease of the cumulative NMR pore volume as function of increasing pressure

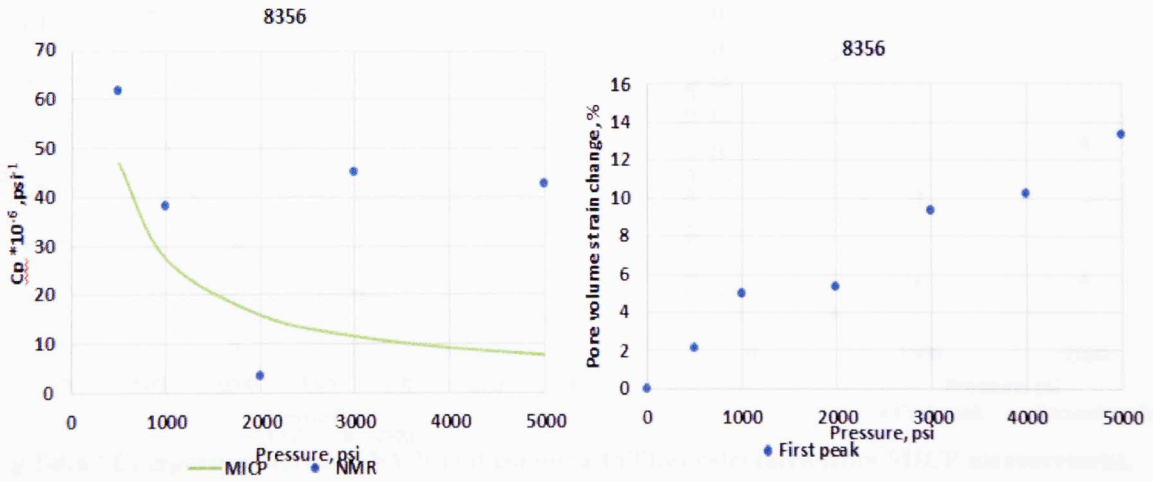

Fig A6:a) Comparison between NMR and compressibilities calculated from MICP measurement. The measured NMR compressibility tends to agree with MICP derived pore volume compressibility. b) pore volume change as function of confining pressure.

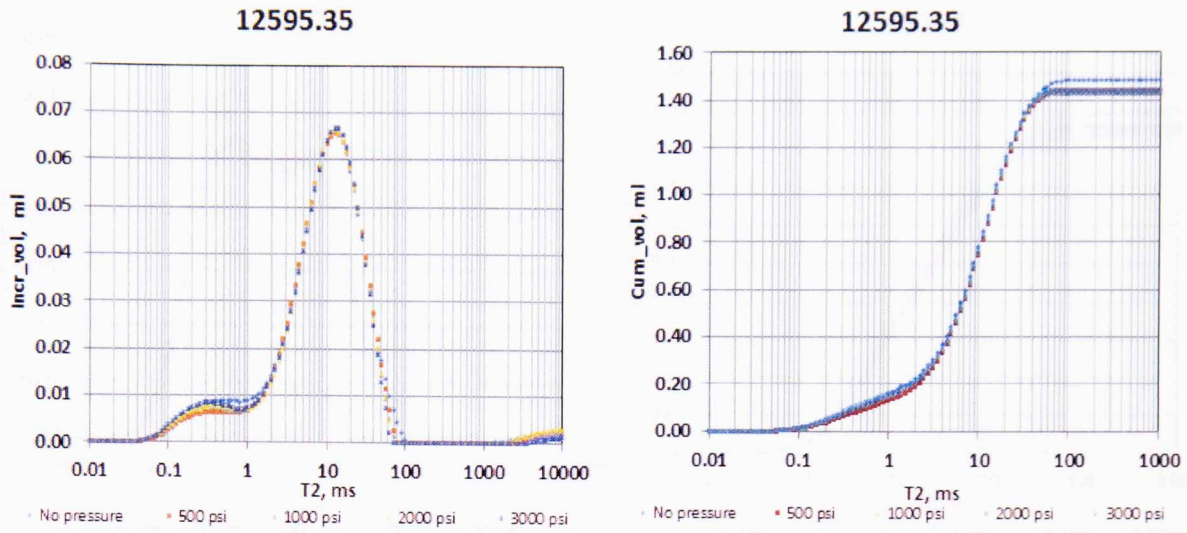

Fig B7:a) T_2 relaxation spectra showing the NMR incremental volume change as a function of pressure on dodecane saturated Eagle Ford sample. b) NMR cumulative volume change as a function of function of pressure for the Eagle Ford 12595.35. Note the decrease in pore volume at small T2 relaxation and the decrease of the cumulative NMR pore volume as function of increasing pressure

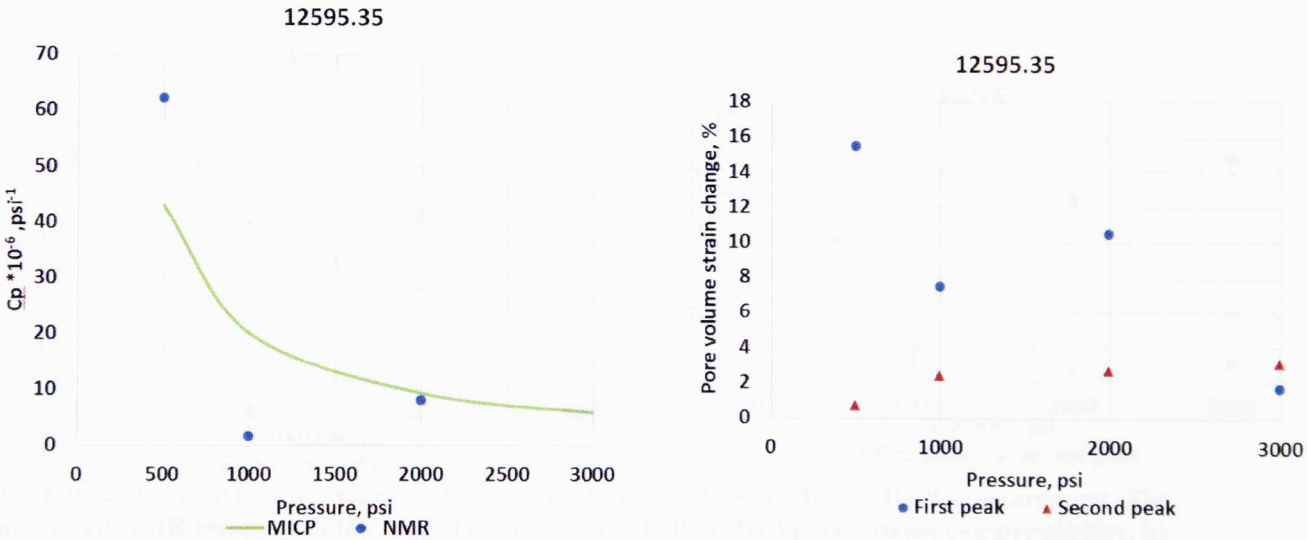

Fig B8:a) Comparison between NMR and compressibilities calculated from MICP measurement. The measured NMR compressibility tends to agree with MICP derived pore volume compressibility. b) pore volume change as function of confining pressure.

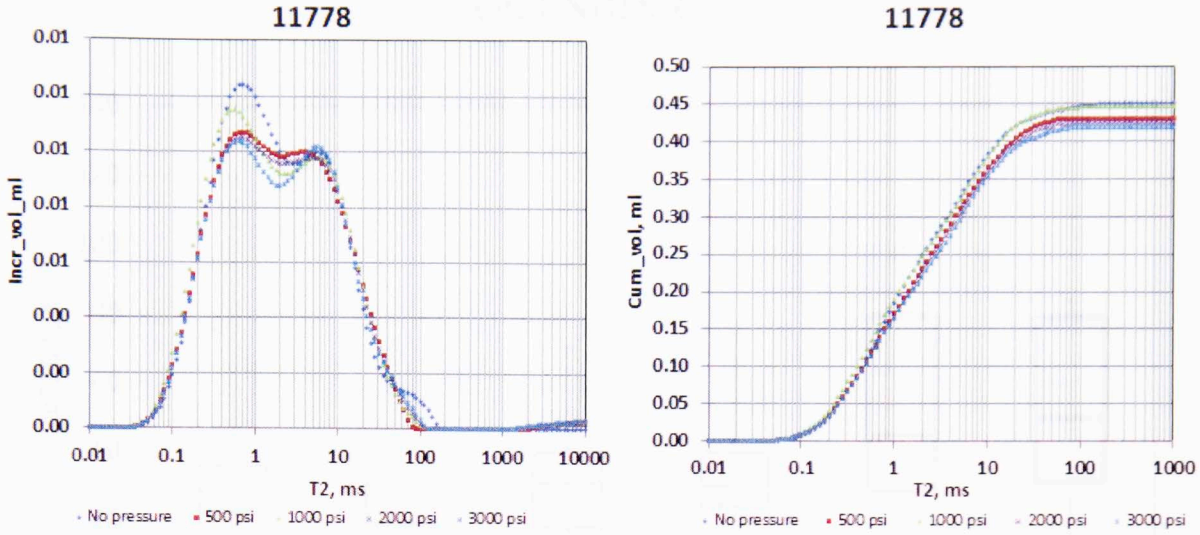

Fig BA9:a) T_2 relaxation spectra showing NMR incremental volume change as a function of pressure on dodecane saturated Eagle Ford sample . b) NMR cumulative volume change as a function of function of pressure for the Haynesville 11778. Note the decrease in pore volume at small T2 relaxation and the decrease of the cumulative NMR pore volume as function of increasing pressure

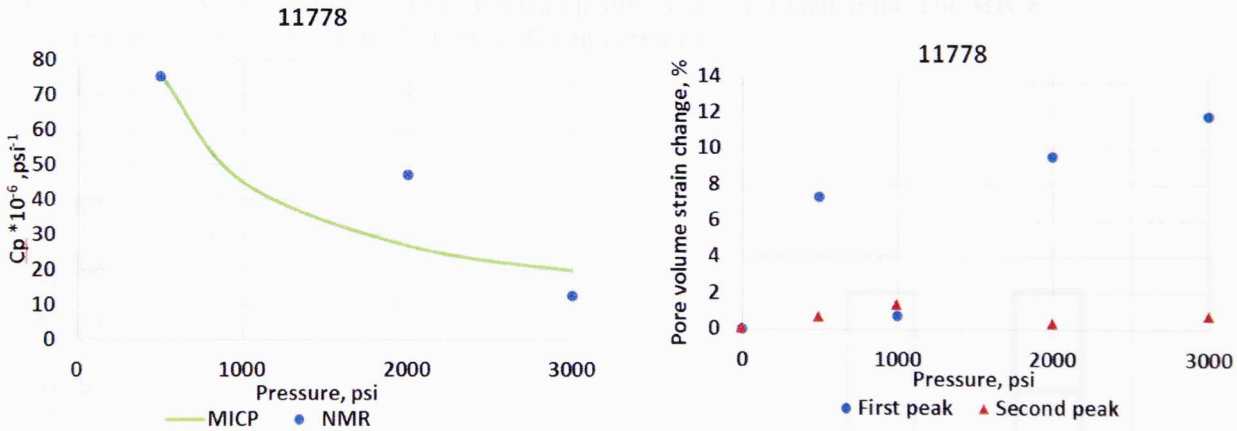

Fig B10:a) Comparison between NMR compressibilities calculated from MICP measurement. The measured NMR compressibility tends to agree with MICP derived pore volume compressibility. b) pore volume change as function of confining pressure.

APPENDIX-C

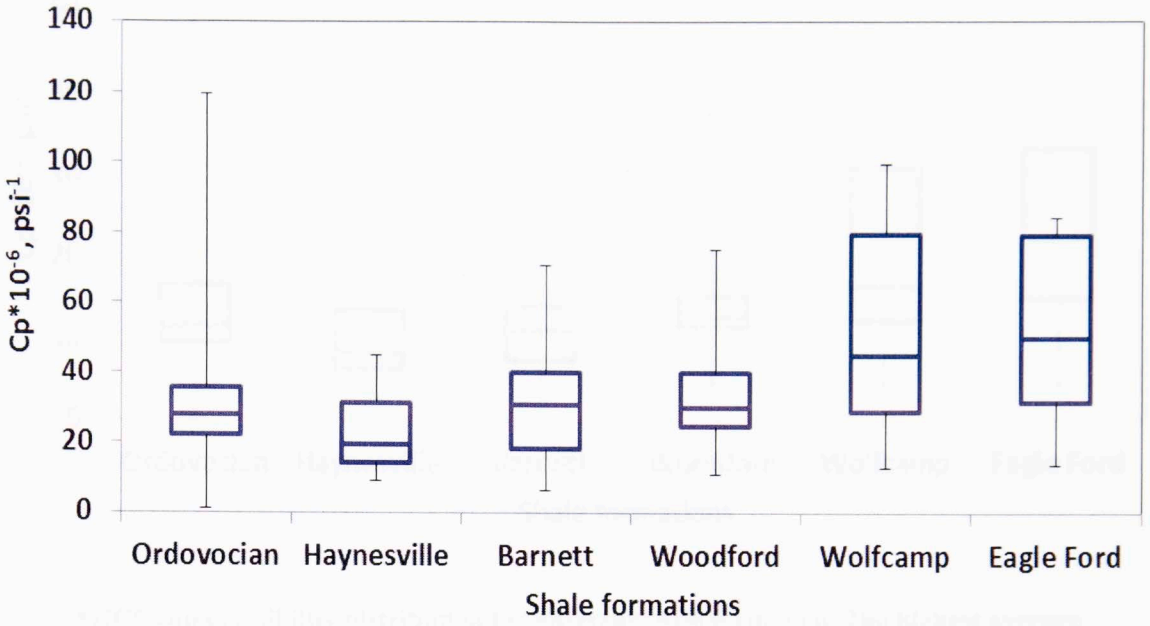

Fig C1: MICP compressibility distribution for different shale formation. The highest average compressibilities were measured for the Wolfcamp and Eagle Ford formation. The MICP compressibilities are reported at 1000 psi confining pressure.

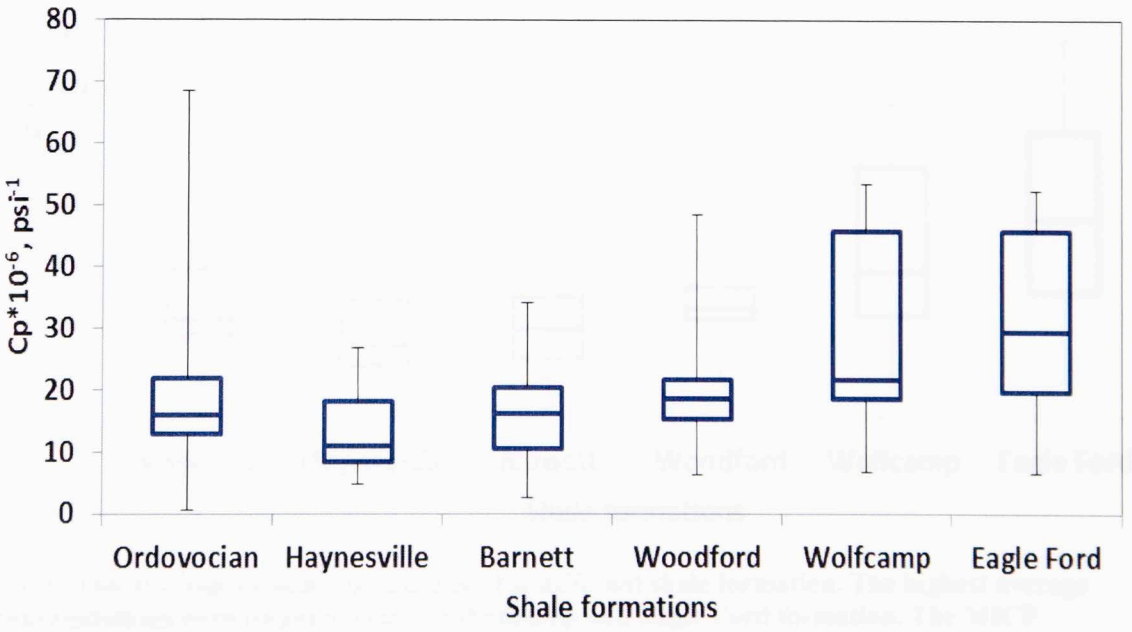

Fig C2: MICP compressibility distribution for different shale formation. The highest average compressibilities were measured for the Wolfcamp and Eagle Ford formation. The MICP compressibilities are reported at 2000 psi confining pressure.

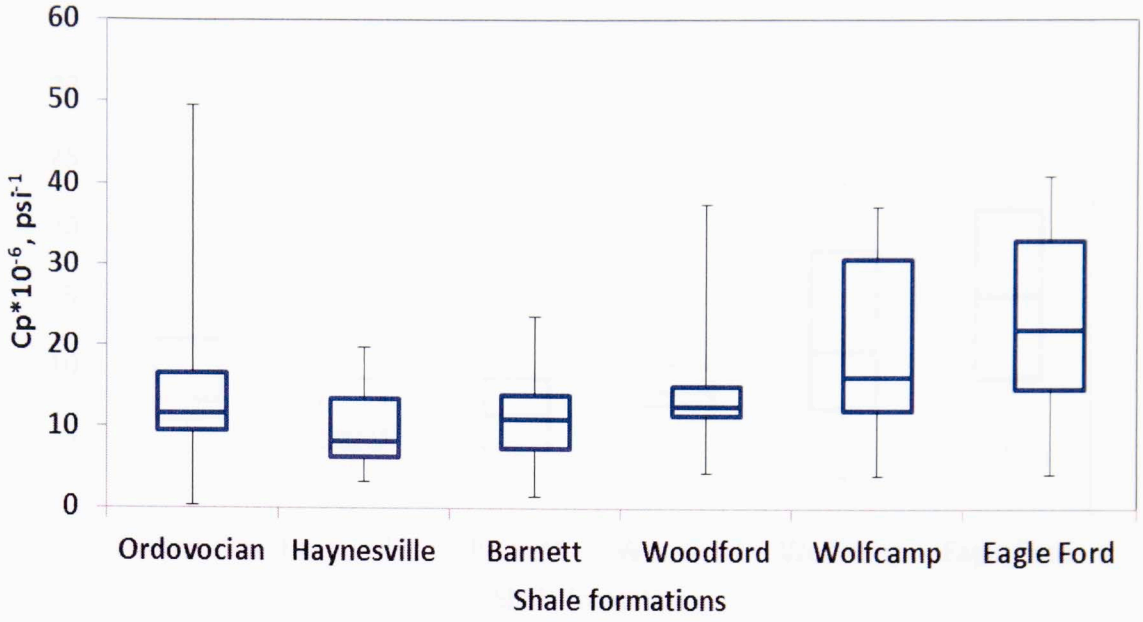

Fig C3: MICP compressibility distribution for different shale formation. The highest average compressibilities were measured for the Wolfcamp and Eagle Ford formation. The MICP compressibilities are reported at 3000 psi confining pressure.

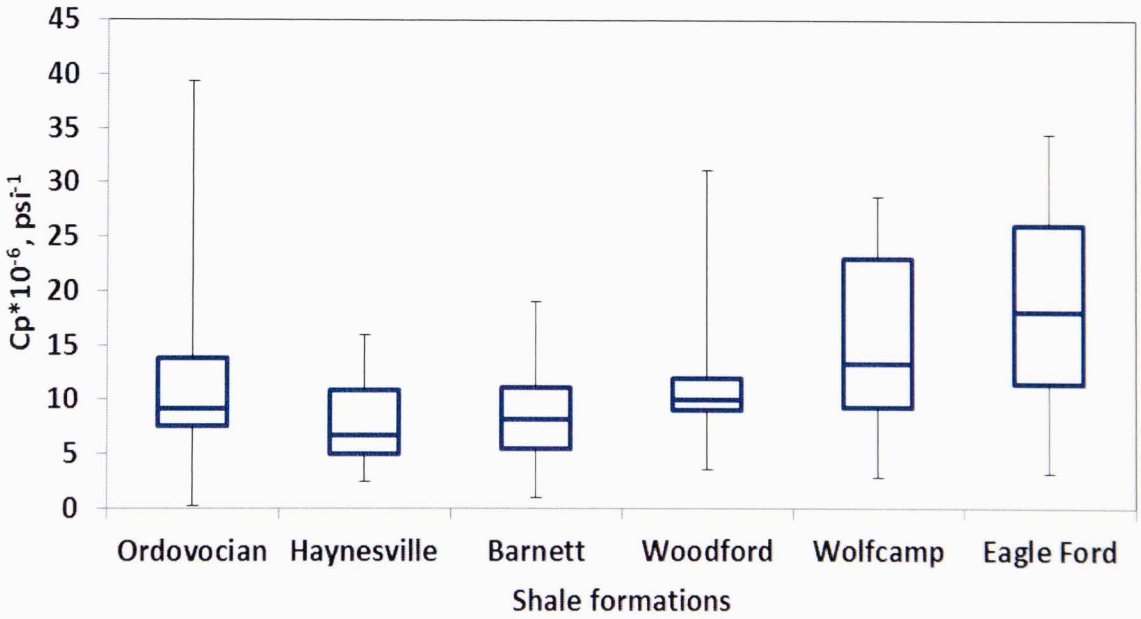

Fig C4: MICP compressibility distribution for different shale formation. The highest average compressibilities were measured for the Wolfcamp and Eagle Ford formation. The MICP compressibilities are reported at 4000 psi confining pressure.

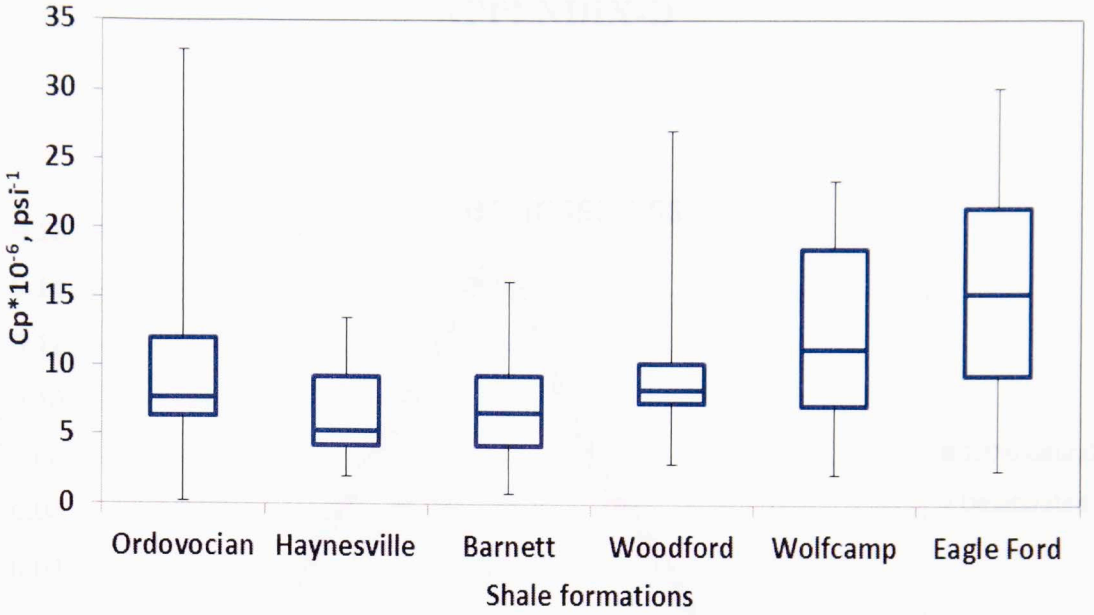

Fig C5: MICP compressibility distribution for different US shale formation. The highest average compressibilities were measured for the Wolfcamp and Eagle Ford formation. The MICP compressibilities are reported at 5000 psi confining pressure.

APPENDIX-D

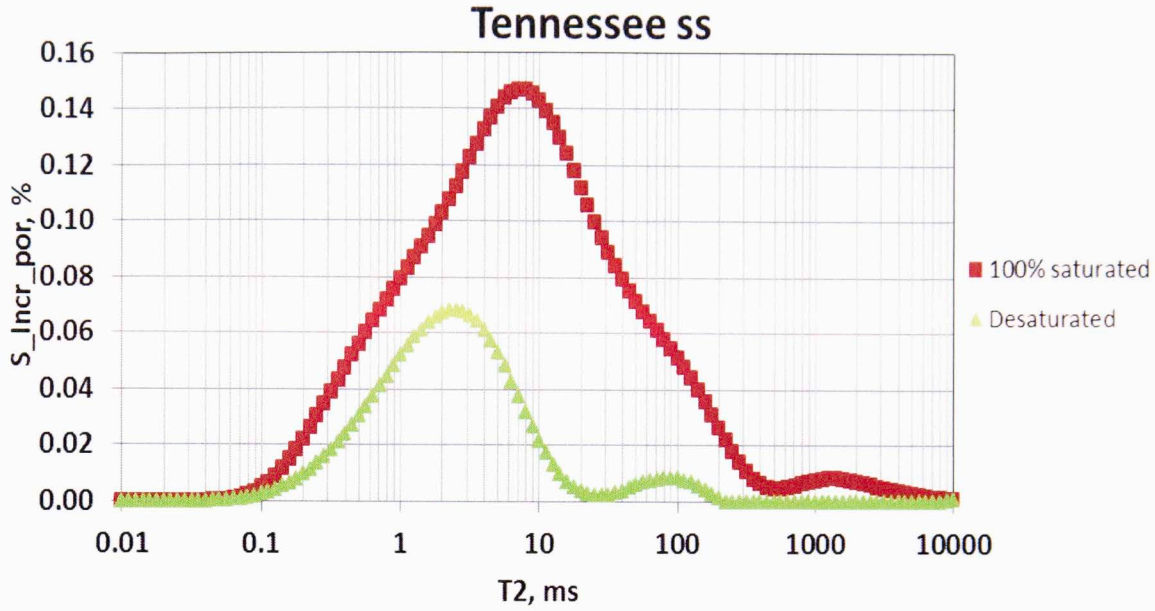

Fig D1: T2 relaxation versus incremental porosity for Tennessee sandstone 100% saturated with brine and after desaturating the sample in the centrifuge at 100 psi.

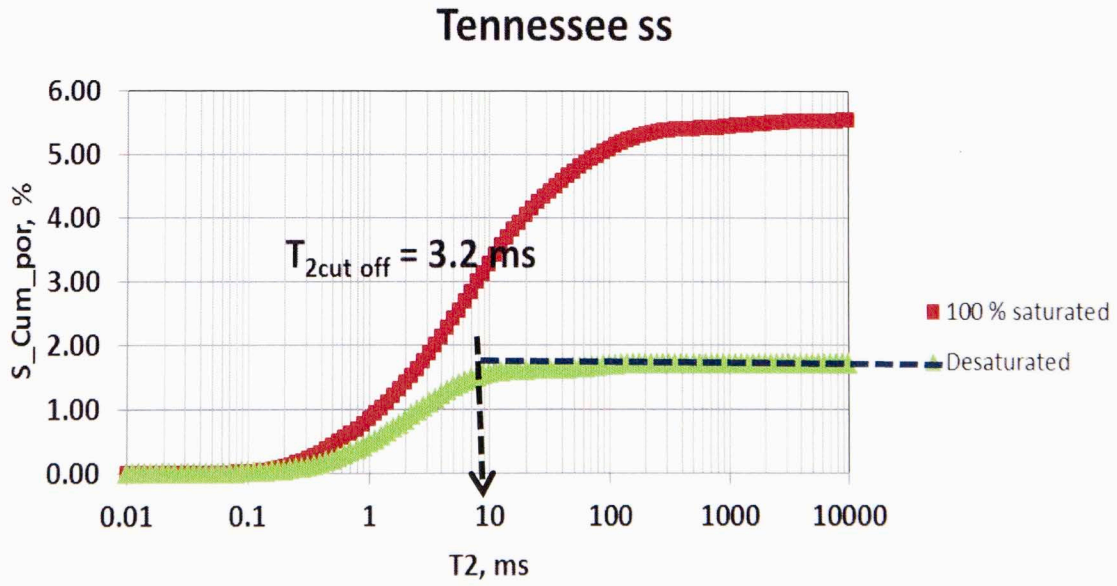

Fig D1: T2 relaxation versus cumulative porosity for Tennessee sandstone 100% saturated with brine and after desaturating the sample in the centrifuge. The T_2 cut off for the Tennessee sandstone was equal to 3.2 ms and the Swirr~ 28%